

ANA FLÁVIA SUZANA

***In situ* imaging of gold nanocrystals during the CO oxidation
reaction studied by Bragg Coherent Diffraction Imaging.**

Thesis presented to the Institute of
Chemistry, São Paulo State University, for
the requirements for the degree of Doctor
of Chemistry.

Supervisor: Prof. Dr. Sandra Helena Pulcinelli
Co-supervisor: Dr. Florian Meneau

Araraquara

2019

ANA FLÁVIA SUZANA

Imageamento *in situ* de nanocristais de ouro durante a reação de oxidação de CO estudada por Imageamento por Difração Coerente de Bragg.

Tese apresentada ao Instituto de Química,
Universidade Estadual Paulista, como
parte dos requisitos para obtenção do título
de Doutora em Química.

Orientadora: Prof. Dr. Sandra Helena Pulcinelli
Co-orientador: Dr. Florian Meneau

Araraquara

2019

FICHA CATALOGRÁFICA

S968i Suzana, Ana Flávia
In situ imaging of gold nanocrystals during the CO
oxidation reaction studied by Bragg Coherent Diffraction
Imaging / Ana Flávia Suzana. – Araraquara: [s.n.], 2019
149 p.: il.

Thesis (doctor) – Universidade Estadual Paulista,
Instituto de Química

Advisor: Sandra Helena Pulcinelli

Co-advisor: Florian Meneau

1. Diffraction. 2. Nanocrystals. 3. Gold. 4. Crystals-
Defects. 5. Deformation. I. Title.

CERTIFICADO DE APROVAÇÃO

TÍTULO DA TESE: "*In situ* imaging of gold nanocrystals during the CO oxidation reaction studied by Bragg Coherent Diffraction Imaging"

AUTORA: ANA FLAVIA SUZANA

ORIENTADORA: SANDRA HELENA PULCINELLI

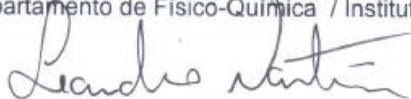
COORDENADOR: FLORIAN MENEAU

Aprovada como parte das exigências para obtenção do Título de Doutora em QUÍMICA, pela Comissão Examinadora:



Prof.^a. Dr.^a. SANDRA HELENA PULCINELLI

Departamento de Físico-Química / Instituto de Química - UNESP - Araraquara



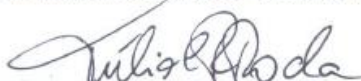
Prof. Dr. LEANDRO MARTINS

Departamento de Bioquímica e Tecnologia Química / Instituto de Química - UNESP - Araraquara



Prof. Dr. RODRIGO FERNANDO COSTA MARQUES

Departamento de Físico-Química / Instituto de Química - UNESP - Araraquara



Prof. Dr. TULIO COSTA RIZUTI DA ROCHA

Departamento - LNLS / Laboratório Nacional de Luz Síncrotron - Campinas



Prof. Dr. IAN KEITH ROBINSON

Faculty of Maths & Physical Sciences / London Centre for Nanotechnology - Londres - Reino Unido

Araraquara, 26 de março de 2019

CONTACT AND PERSONAL INFORMATION

Ana Flávia Suzana

Rua Vitorino Ferrari, 54, Campinas-SP (Brazil)

CEP 13084 050

Phone: +55 (19) 981839037

E-mail: ana.suzana@lnls.br

Birthdate: February 15th 1988

Citizenship: Brazilian

Languages (spoken and written): English, Portuguese (native)

EDUCATION

M. Sc. in Physicochemistry, March 2015

São Paulo State University Júlio de Mesquita Filho (Unesp) – Institute of Chemistry
(Araraquara, São Paulo, Brazil)

“Hybrid materials clay-poly(methyl methacrylate) obtained through grafting method”

B. S. Degree in Chemistry, January 2012

São Paulo State University Júlio de Mesquita Filho (Unesp) – Institute of Chemistry
(Araraquara, São Paulo, Brazil)

PUBLICATIONS

Submitted/in preparation:

- Suzana, Ana; Rochet, Amélie; Passos, Aline; Zerba, João; Pólo, Carla; Santilli, Celso; Pulcinelli, Sandra; Berenguer, Felisa; Harder, Ross; Maxey, Evan; Meneau, Florian. **Three-dimensional in situ imaging of catalytic reaction on gold nanocrystal**. In review at ACS Catalysis.

Published:

- Rochet, A., Suzana, A. F.; Passos, A. R.; Kalile, T.; Berenguer, F.; Santilli, Celso V.; Pulcinelli, Sandra H.; Meneau, F. ***In situ* reactor to image catalysts at work in three-dimensions by Bragg coherent X-ray diffraction**. Catalysis Today, online, 2018.
- Suzana, A. F.; Ferreira, E. A.; Benedetti, A. V.; Carvalho, H. W. P.; Santilli, Celso V.; Pulcinelli, Sandra H. P. **Corrosion protection of chromium-coated steel by hybrid sol-gel coatings**. Surface & Coatings Technology, v. 299, p. 71-80, 2016.
- De Carvalho, H. W. P.; Suzana, A. F.; Santilli, C. V.; Pulcinelli, S. H. **Structure and thermal behavior of PMMA-polysilsesquioxane organic-inorganic hybrids**. Polymer Degradation and Stability, v. 104, p. 112-119, 2014.
- Carvalho, H. W. P.; Suzana, A. F.; Pulcinelli, S. H.; Santilli, C. V. **Synthesis, Structure, and Thermal Stability of Poly(methyl methacrylate)-co-Poly(3-tri(methoxysilyl)propyl methacrylate)/Montmorillonite Nanocomposites**. Polymer Engineering and Science, v. 53, p. 1253-1261, 2013.

CONFERENCES

Oral presentations:

- 3rd International user workshop on coherent X-ray imaging and small angle X-ray scattering (Cateretê Workshop), Campinas, Brazil, 23rd-24th, 2019, *"Three-dimensional in situ imaging of catalytic reaction on gold nanocrystal by Bragg CDI"*;
- International Conference on Novel nanomaterial: Engineering and properties ICON², Saint-Aubin, France, October 18-20th, 2017. *"Strain Field Mapping of a 120 nm Single Gold Nanocrystal Supported on TiO₂ Provided by Bragg Coherent Diffraction Imaging During in situ CO Oxidation Reaction"*;
- Presentation of the general seminar *"Fundamentos e aplicações da radiação síncrotron na Química"*, as part of the Ph.D. program of the Institute of Chemistry - Unesp-Araraquara on April 1st, 2016;
- XV Brazilian Materials Research Society Meeting, Campinas, Brazil, September 25-29th, 2016, *"Simple one-step green synthesis of gold nanoparticles with controlled size using imidazolium ionic liquid as ligand"*;
- XIII Brazilian Materials Research Society Meeting, João Pessoa, Brazil, September 28th - October 02nd, 2014, *"Structure and thermal behavior of organic-inorganic PMMA-MMT-Na⁺ hybrids"*.

Awards:

- The student won the student oral communication award for the oral presentation category; *"Strain Field Mapping of a 120 nm Single Gold Nanocrystal Supported on TiO₂ Provided by Bragg Coherent Diffraction Imaging During in situ CO Oxidation Reaction"*. ICON², Saint-Aubin, France, October 18-20th, 2017.

Others:

- Completion of the Research Internship Abroad (BEPE-FAPESP) at Synchrotron Soleil, France, from 19/06/2017 to 18/06/2018 under the supervision of Dr Felisa Berenguer, beamline scientist at the Cristal beamline, dedicated, among other techniques, to Bragg Coherent Diffraction Imaging (Bragg CDI).

“Life’s most persistent and urgent question is: What are you doing for others?”

Martin Luther King Jr.

I would like to dedicate this work to my lovely family:

Mom, Dad, Fer, Maria Stella and Josi.

Acknowledgements

In this first line I would like to thank my supervisor Florian Meneau for the opportunity in this fascinating scientific area, all the knowledge, for the patience with my “beginner” questions, for the encouragement words (“Yes, yes, it is easy, just do it!”) and for being constantly present and helpful. I own to him a very special thanks for all these reasons. A special thanks to professor Sandra who welcomed me in her group since I was an undergraduate student, for teaching me in many scientific and personal aspects. I would like to thank Felisa Berenguer for the help in understanding the technique explored in this work and for the friendship. Thank to Celso Santilli for the fruitful scientific discussions.

I would like to thank the people who hardly worked in this project, with the data collection, treatment and interpretation: Aline Passos, Amélie Rochet and João Zerba, who are deeply involved in this work.

I would like to thank my family: my mom Marta, my dad Milton, my brother Fernando, my little sister Maria Stella, cousin Lucas, aunts Lúcia, Márcia, uncle Valter and my grandmother Helena, for the love and affection.

A special thanks to Josi, for the friendship, for all the love, the support and for being this amazing person.

I thank my special friends who I consider as part of my family: Cláudia, Flávia and Douglas. And a special thanks to Dilma, Tiago and Rafinha, for all the friendship and for being this amazing and lovely family!

A special thanks for special friends from work: Paloma, Phelipe and Thiago, who I consider amazing people, being always sweet, gentle and thinking about the others. It was a pleasure to be with them during this time.

My friends who I met in France: Lauriane, Eloisa, Bruno, Marininha, Rodrigo and Antoniel. I will always remember our conversations and our laughs! And also, the special people that I met at LNLS: the amazing Colombian/Peruvian guys, Carlitos, Ximenita and Vanessa and also Glauco. They were very important for me here. Thank you!

I thank my university, Unesp, the Institute of Chemistry, the group of Physicochemistry of materials, the Brazilian center for Research in Energy and Materials (CNPEM), the Brazilian Synchrotron Light Laboratory (LNLS), Nacional Laboratory of Nanotechnology (LNNano), Advanced Photon Source (APS) and Synchrotron Soleil for the disposal of infrastructure and all the people from Cristal and 34-ID-C beamlines, specially Ross Harder for the help with the technique and the data treatment/interpretation.

I thank the staff from LNLS: Natália Moreno, Simone Betim, Fábio Zambello and Tiago Kalile for the help with the instruments and measurements. I also would like to thank Stéphanie Blanchandin, Karine Chaouchi and Valérie Briois from Soleil for the fruitful discussions and help.

I would like to thank FAPESP and CAPES for the scholarship and financial support.

ABSTRACT

The fundamental aim of heterogeneous catalysis research is to understand mechanisms at the nanoparticle level, and then to design and synthesise catalysts with desired active sites. In this regard, the *in situ/operando* characterisation of defects is crucial as they are preferential catalytic sites for the reaction occurrence.

The main part of this thesis was the investigation of the morphology and structure evolution of gold nano-catalysts supported on titanium dioxide. We worked with different methods of preparation (seed-growth, ionic liquid stabilizer) to synthesise gold catalysts with controlled sizes. Those catalytic materials were evaluated for the model CO oxidation reaction, chosen for its environmental relevance and “simplicity” to be reproducible within our X-ray imaging study.

We used the Bragg Coherent Diffraction Imaging technique to follow *in situ* the 3D morphology changes under catalytic reaction conditions. A dedicated *in situ* heating reactor has been built. We correlated the 3D displacement field and strain distribution of the gold nanoparticles to the catalytic properties of the material. In particular, for a 120 nm gold nanoparticle, we quantified under working conditions the adsorbate-induced surface stress on the gold nanocrystal, which leads to restructuring and defects identified as a nanotwin network.

Finally, by using scanning X-ray nanodiffraction to characterise few tenths of nanometers single gold nanorods, we were able to obtain a strain map over the Bragg well oriented gold crystals. This characterisation revealed the presence of a strain pattern encoded in the nanorods structure consistent with the so-called Rayleigh Instability. This kind of study proved to be very important as the presence of instability does affect the properties of nanorods.

Keywords: *in situ* Bragg CDI, gold nanocrystals, CO oxidation reaction, strain, twin defects, nanodiffraction.

RESUMO

O principal objetivo da catálise heterogênea é entender os mecanismos de reação a nível nanométrico e planejar/sintetizar catalisadores com os sítios ativos desejados. A este respeito, a caracterização de defeitos *in situ/operando* é crucial, pois esses são sítios catalíticos preferenciais para a ocorrência da reação.

A parte principal desta tese foi a investigação da morfologia e evolução estrutural de nano-catalisadores de ouro suportados em dióxido de titânio. Trabalhamos com diferentes métodos de preparação (crescimento de “sementes”, uso de líquidos iônicos como agentes estabilizantes) para sintetizar catalisadores de ouro com tamanhos controlados. Esses catalisadores foram testados para a reação modelo de oxidação de CO, escolhida por sua relevância ambiental e "simplicidade" para ser reproduzível em nosso estudo de imageamento por raios-X.

Utilizamos a técnica Imageamento por Difração Coerente de Bragg para acompanhar *in situ* as alterações da morfologia em 3D nas condições da reação catalítica. Um reator que permite aquecimento, dedicado a experimentos *in situ*, foi construído. Correlacionamos o *strain* e *displacement field* em 3D das nanopartículas às propriedades catalíticas do material. Para uma nanopartícula de 120 nm em particular, nós quantificamos sob condições de funcionamento o *stress* superficial induzido pelo processo de adsorção no nanocristal, o que leva à reestruturação da nanopartícula e defeitos identificados como uma rede nanotwin.

Finalmente, usando nanodifração de raios-X para caracterizar *nanorods* de ouro individuais de algumas dezenas de nanômetros, pudemos obter um mapa de *strain* para os cristais de ouro bem orientados na condição de Bragg. Esta caracterização revelou a presença de um padrão de deformação codificado na estrutura dos *nanorods*, consistente com a chamada Instabilidade de Rayleigh. Esse tipo de estudo provou ser muito importante, pois a presença de instabilidade afeta as propriedades dos *nanorods*.

Palavras-chave: *in situ* Bragg CDI, nanocristais de ouro, reação de oxidação do CO, *strain*, defeitos twin, nanodifração.

List of Figures

Figure 2.1. (a) Plane-wave CDI: a plane-wave illuminates fully the sample and the diffraction pattern is measured in the far-field. (b) Ptychography CDI: can be applied to Plane-wave-CDI to study extended specimens. Figure reproduced from reference (5).	37
Figure 2.2. (a) Number of publications and (b) number of citations over the last 20 years in the Web of Science database using the input terms “Bragg Coherent Diffraction Imaging” or “Bragg Coherent Diffractive Imaging”.....	38
Figure 2.3. Illustration of the longitudinal coherence length (L_L), value representing the length which the waves (initially in phase) become shifted by π . Figure from reference (10).....	39
Figure 2.4. Illustration representing the transverse coherence length (L_T).	40
Figure 2.5. (a) Diffraction of X-rays for a perfect crystalline structure. (b) Diffraction of X-rays for a realistic case of a defected structure. (c) The Q vector is the vectorial difference between the incident and scattered vectors (k_i and k_f , respectively).....	41
Figure 2.6. Iterative phase retrieval based on the Gerchberg-Saxton algorithm (12); n is the iteration number.....	43
Figure 2.7. Schematic of a crystalline structure with displaced atoms by Δd (in red), showing the displacement vector u	45
Figure 2.8. Schematic of the sample alignment to the center of rotation. Figure from reference (17).....	47
Figure 2.9. Example of a 2D Bragg peak for the center of the rocking curve. The red square represents the cropped area and the red arrows point to scattering contributions from different objects.....	48
Figure 2.10. Representation of the different types of stacking faults present in a fcc structure: (a) intrinsic and (b) extrinsic.	49
Figure 2.11. Schematic of a twin domain formation.....	50
Figure 2.12. (a) Schematic representing a perfect crystal, in the absence of dislocation. (b) When shear stress is applied in the crystal, the structure is plastically deformed provoking a slide of the atomic planes over each other.....	51
Figure 2.13. Representative schematic of an edge dislocation. When shear stress (represented by the blue arrows) is applied to the crystalline structure, the metallic bond can break, and a new bond is created, as shown by the red lines. The symbol \perp represents the edge dislocation.....	51
Figure 2.14. Burgers circuit for (a) a perfect crystal and (b) a crystal with screw dislocation. Figure from reference (18).....	52

Figure 2.15. Burgers vector (in red) from the origin to the center of a body-centered cubic cell.....	52
Figure 2.16. Schematic representation of a Shockley partial dislocation. Figure from reference (18).....	53
Figure 2.17. Possible slip ways of {111} planes in fcc crystals: b_1 vector represents a perfect dislocation and b_2/b_3 vectors, partial dislocations. Figure adapted from reference (18).....	53
Figure 2.18. Reachable strain resolution for TEM, CDI and High resolution X-ray diffraction. The graphic brings the main advantages and drawbacks of each of them. Figure adapted from reference (19).....	54
Figure 3.1. STEM images of the seed Au NP at different magnifications (the scale bar is 100 nm).....	60
Figure 3.2. (a) UV-Vis spectra of the seed Au NP. (b) SAXS curve of this sample (black) and its respective fit using a sphere model and lognormal distribution.	60
Figure 3.3. (a) UV-Vis spectra and (b) SAXS curve (in black) of the sample <i>50_Au</i> . The fit (in red) was done using the sphere model, diameter = 50 nm.....	62
Figure 3.4. STEM images of <i>50_Au</i> (scale bar 25 nm).	62
Figure 3.5. (a) UV-Vis spectra and (b) SAXS curve of the sample <i>120_Au</i> , synthesised following the seed approach. The sample scattering is shown in black and the fitting using the sphere form factor, in red.	63
Figure 3.6. STEM images of the sample <i>120_Au</i> (scale bar 100 nm).	63
Figure 3.7. HRTEM images of the samples <i>NPILBrAuBr</i> , <i>NPILBrAuCl</i> , <i>NPILClAuBr</i> and <i>NPILClAuCl</i> (the scale bar is 20 nm). The diameter distribution below the images is shown as well.	65
Figure 3.8. (a) SAXS curves and (b) UV-Vis spectra of the samples <i>NPILBrAuBr</i> , <i>NPILBrAuCl</i> , <i>NPILClAuBr</i> and <i>NPILClAuCl</i>	66
Figure 3.9. (a) SEM images at different magnifications of the sample <i>TiO₂-a</i> . (b) Diffractogram of this sample.	67
Figure 3.10. (a) SEM images at different magnifications of the sample mixed <i>TiO₂</i> (anatase/rutile). (b) Diffractogram of this sample, where there is a mixture of both phases, anatase (denoted by A) and rutile (denoted by R).	68
Figure 3.11. STEM images at different magnifications of the sample <i>NPILClAuCl-TiO₂-a</i>	69
Figure 3.12. STEM images at different magnifications of the samples <i>50_Au/TiO₂-a</i> (a) and <i>50_Au/TiO₂-m</i> (b).	70
Figure 3.13. STEM images at different magnifications of the samples <i>120_Au/TiO₂-a</i> (a) and <i>120_Au/TiO₂-m</i> (b).	71

- Figure 3.14.** Mass spectrometry signal for CO (black), O₂ (red) and CO₂ (blue) obtained for the catalytic tests of *NPILClAuCl-TiO₂-a*, *50_Au/TiO₂-a*, *50_Au/TiO₂-m*, *120_Au/TiO₂-a* and *120_Au/TiO₂-m*. The dashed lines represent the heating and the solid lines, the cooling step.....73
- Figure 3.15.** UV-Vis spectra of the Au NR, showing two bands corresponding to the transverse (at 527 nm) and longitudinal (at 1060 nm) SPR modes. The inset shows a SEM image.....75
- Figure 3.16.** Au NR SAXS curve (black) and the cylinder/sphere model fit (red) used to fit the different q regions of the experimental data.....76
- Figure 4.1.** Schematic overview of the cell. (1) ceramic heating device, (2) clamp, (3) cell body, (4) gas inlet, (5) gas outlet, (6) Kapton window.80
- Figure 4.2.** Infrared thermography measurement of the sample holder heated at 400 °C: IR thermography image and temperature distribution on the whole image. Scale bar corresponds to 1 mm.....81
- Figure 4.3.** Mass spectrometry signal of CO (black), O₂ (red) and CO₂ (blue) obtained at the outlet of the cell during heating-cooling reaction cycle (1% CO, 0.5% O₂). Heating: dashed line and cooling: solid line.....82
- Figure 4.4.** Schematic of the Cristal beamline. Figure adapted from (4).....83
- Figure 4.5.** Experimental set-up of Cristal beamline showing the θ -2 θ configuration for the Bragg CDI experiment.83
- Figure 4.6.** Photography of the cell installed at the Cristal beamline at SOLEIL.....84
- Figure 4.7.** Part of the X-ray diffraction data measured during the rocking curve around the Au (111) reflection for one Au/TiO₂ nanoparticle at RT under He (A).86
- Figure 4.8.** Part of the X-ray diffraction data measured during the rocking curve around the Au (111) reflection for one Au/TiO₂ nanoparticle at RT under CO/O₂ (B).87
- Figure 4.9.** Part of the X-ray diffraction data measured during the rocking curve around the Au (111) reflection for one Au/TiO₂ nanoparticle at 400 °C under CO/O₂ (C).....88
- Figure 4.10.** 2D slices through the 3D coherent diffraction patterns around the center of the Bragg spot for the same individual Au/TiO₂ nanoparticle at RT under He flux (A) and under CO/O₂/He flux (B). (C) 2D slice for another Au/TiO₂ nanoparticle obtained at 400 °C under CO/O₂/He flux whilst the CO oxidation reaction is occurring.89
- Figure 4.11.** Morphology of the gold nanoparticle reconstructed from Bragg CDI patterns measured under He at RT (A), under CO/O₂/He at RT (B) and at 400 °C (C). The side (left), bottom (middle) and top (right) views are presented. The green and black marks are showing the faceted and rounder shapes of the nanoparticles. Scale bar corresponds to 100 nm.....90
- Figure 4.12.** Particle cross-sections displaying the phase and lattice displacement, projected along (111) of the interior of the nanoparticle at RT (A) under He, (B) under

CO/O₂/He and (C) at 400 °C under CO/O₂/He. As shown in the figure inset, cross-sections are made at the center of the nanoparticle perpendicular (top) and parallel (bottom) to the support. Scale bar corresponds to 100 nm.92

Figure 5.1. Schematic of the 34-ID-C beamline. Adapted from (2).97

Figure 5.2. (a) The *in situ* cell used for the Bragg CDI experiment, where the gas/temperature connections are shown; (b) SEM image showing the distribution of the sample 120_Au/TiO₂-m on the silicon nitride membrane.98

Figure 5.3. Picture of the experimental setup at the beamline 34-ID-C, showing the experimental cell, the gas and electrical connections, the detector position and the incoming/diffracted X-rays.98

Figure 5.4. Series of 2D coherent diffraction patterns of a gold nanocrystal recorded at RT under air (for sake of clarity, only one every two patterns is shown (0.04°)). Inset: 3D Bragg diffraction peak obtained by stacking the 2D diffraction patterns. The intensity of the diffraction patterns scales from 0 to 128612 counts; the rocking curve was measured by ten exposures of 5 s each of them.101

Figure 5.5. (a) Top and bottom views (the scale bar is 50 nm) of a gold nanocrystal recorded at RT under air. The direction of the Q vector is shown in the top view. (b) STEM image of the Au NP (the scale bar is 100 nm). The zoom in region highlights the hexagonal shape of the particle.102

Figure 5.6. Averaged line profiles. Lines (A, black) along the vertical and (B, red) horizontal directions of the particle cross-section presented as a green surface on the right. The derivatives of the line scans are showing that the reconstruction resolution is 12 nm.103

Figure 5.7. Series of 2D coherent diffraction patterns of a gold nanocrystal recorded at RT under CO/O₂ (for sake of clarity, only one over two patterns are shown (0.04°)). The intensity of the diffraction patterns scales from 0 to 115171 counts; the rocking curve was measured by ten exposures of 5 s each of them.104

Figure 5.8. Top: 3D Bragg diffraction peak of the gold NP at RT under air (a) and CO/O₂ (b). Bottom: Grey isosurface (30%) representing the particle shape of the same Au/TiO₂ nanoparticle in side view. The dotted lines are showing the faceted and rounder shapes of the nanoparticle.105

Figure 5.9. Three-dimensional views as function of phase of the gold nanocrystal under both atmospheres, air and CO/O₂ at RT.106

Figure 5.10. Cross-section views as function of phase of the gold nanocrystal under both atmospheres air and CO/O₂ at RT. The inset represents the four cross-section planes shown. The inset in the first column represents the q vector direction.106

Figure 5.11. Three-dimensional views as function of strain of the gold nanocrystal under both atmospheres air and CO/O₂ at RT.108

- Figure 5.12.** Cross-section views as function of strain of the gold nanocrystal under both atmospheres air and CO/O₂ at RT. The inset represents the four cross-section planes shown. 108
- Figure 5.13.** Three-dimensional views as function of phase of the gold nanocrystal under CO/O₂ at RT, 200 °C and 400 °C. The green gradient represents the increase of catalytic activity as function of the temperature. 109
- Figure 5.14.** Three-dimensional views as function of strain of the gold nanocrystal under CO/O₂ at RT, 200 °C and 400 °C. The green gradient represents the increase of catalytic activity as function of the temperature. 109
- Figure 5.15.** Cross-section views as function of phase of the gold nanocrystal under CO/O₂ at RT, 200 °C and 400 °C. The inset represents the four cross-section planes shown. The green gradient represents the increase of catalytic activity as function of the temperature. 111
- Figure 5.16.** Cross-section views as function of strain of the gold nanocrystal under CO/O₂ at RT, 200 °C and 400 °C. The inset represents the four cross-section planes shown. The green gradient represents the increase of catalytic activity as function of the temperature. 111
- Figure 5.17.** Line scans of the phase and strain along the dashed line of the cross-sections presented for illustration at 400 °C under CO/O₂. The black line corresponds to the gold catalyst at room temperature, with no catalytic activity, the blue line to the same cross section at 200 °C, and the red line to the same, but active gold catalyst at 400 °C. 112
- Figure 5.18.** 3D and cross sections of the distribution of the low (yellow) and high (green) phase shift of the same Au/TiO₂ nanoparticle under CO/O₂ at 200 °C (A) and 400 °C (B). The black arrows indicate the position of the nanotwin network. 113
- Figure 5.19.** Phase shift distribution for the Au nanocrystal at 200 and 400 °C under CO/O₂. Distribution of the maximum phase (0.4-1.1) of the same Au/TiO₂ nanoparticle under CO/O₂ at 200 °C in top view (A) and at 400 °C in top (B) and side view (C). The crystal at 200 °C shows highly distorted areas concentrated at the surface. At 400 °C, a complex network is present with highly distorted areas crossing the entire volume of the crystal. 114
- Figure 5.20.** Cross-section views of the nanoparticle measured at 400 °C under air in function of both, phase and strain. 115
- Figure 6.1.** Series of 2D coherent diffraction patterns of a gold nanocrystal (*Particle 2*) presenting twin defects recorded at RT under air (for sake of clarity, only one every two patterns is shown (0.04°)). The intensity of the diffraction patterns scales from 0 to 84120 counts; the rocking curve was measured by ten exposures of 5 s each of them. 121
- Figure 6.2.** (a) Reconstruction of the 120 nm Au/TiO₂ catalyst measured at RT under air in function of phase. 1, 2 and 3 correspond to the three pieces of the parent crystal;

the designation of the top/bottom parts is shown. (b) STEM image of another nanoparticle from the same batch; the red arrows point to regions of darker contrast, characteristic of twin domains. The scale bar is 50 nm for both, the reconstruction and the STEM image..... 122

Figure 6.3. Twinning domains formation for the (111) planes. The black dotted lines link the parent crystal, here called matrix, with the twinned crystal, which is formed as the mirrored images of the original structure. Figure from reference (2). 122

Figure 6.4. Reconstructions in function of phase for the nanoparticle measured under air at the three different temperatures (RT, 200 °C and 400 °C) showed in top, bottom and side views. The last column shows 2D slices taken as shown in the inset below the slices. 123

Figure 6.5. Reconstructions of the nanoparticle measured at RT under air (left) and under CO/O₂ (right). The yellow marks are showing the faceted and rounder shapes of the nanoparticle, depending on the gas environment. 125

Figure 6.6. Different views of the 3D reconstruction of *Particle 3*, shown as function of phase for the measurement done at 200 °C under CO/O₂. The scale bar is 50 nm. 126

Figure 6.7. Different views of the 3D reconstructions for *Particle 3* at the three different temperatures measured. The data are shown as function of phase..... 127

Figure 7.1. (a) Picture of the 26-ID-C beamline setup and (b) schematic representing the as showed picture of the experimental setup for diffraction/fluorescence mapping; a sketch of the NR composed by the {111} and {200} planes is also displayed. 132

Figure 7.2. Scanning transmission electron microscopy of the gold nanorods dispersed on the silicon nitride membrane used for the nanodiffraction and fluorescence measurements. 133

Figure 7.3. (a) STEM image of the explored area during the nanodiffraction experiment (scale bar 1µm); (b) fluorescence pattern recorded on the area detector of the region highlighted by the white dashed square in (a); (c) diffraction pattern of the same region recorded simultaneously as the fluorescence. The green arrows point to bright diffraction spots derived from well oriented objects. The 2θ angle was configured to the (200) reflection. 134

Figure 7.4. (a) STEM image (scale bar 500 nm) of the region mapped in fluorescence mode shown in (b); (c) diffraction pattern of the same region. The area highlighted by the blue square in (a) is shown zoomed in (d) (scale bar 100 nm); (e) and (f) fluorescence mapping and diffraction pattern, respectively, of the same area using finer steps. In (f), the white arrows represent the direction of the scan (from the left to the right, from the bottom to the top) and the rows 1, 2 and 3 inside the dashed rectangle are the ones taken for the strain calculation. 135

Figure 7.5. (a) SEM image (scale bar 500 nm) of the region mapped in fluorescence mode shown in (b); (c) diffraction pattern of the same region. The area highlighted by

the blue square is shown zoomed in (d); (e) and (f) fluorescence mapping and diffraction pattern, respectively, of the same area using finer steps. In (f), the rows 1, 2 and 3 inside the dashed rectangle are the ones taken for the strain calculation.136

Figure 7.6. (a) SEM image (scale bar 500 nm) of the region mapped in fluorescence mode shown in (b); (c) diffraction pattern of the same region. The area highlighted by the blue square is shown zoomed in (d); (e) and (f) fluorescence mapping and diffraction pattern, respectively, of the same area using finer steps. In (f), the rows 1, 2 and 3 inside the dashed rectangle are the ones taken for the strain calculation.136

Figure 7.7. Diffraction patterns measured along the NR1, NR2 and NR3. The red squares indicate the patterns used for the strain analysis.137

Figure 7.8. Strain as function of the distance from the center of the nanorod, for NR1, NR2 and NR3. Black dots are the strain data and the red curves the sin fitting.138

Figure 7.9. Schematic representation of the Rayleigh instability for a solid rod.....139

List of Tables

Table 1. Diameter (in nm) taken from SAXS and HRTEM imaging of the ultra-small Au NP.	64
Table 2. Evolution of the strain energy and strain energy density as function of temperature.	116
Table 3. Phase offset and distance between the parent and twin portions.	124

Table of Contents

RESUMO EXPANDIDO	25
CHAPTER I: INTRODUCTION	30
1.1. Introduction.....	31
References	33
CHAPTER II: COHERENT DIFFRACTION IMAGING	36
2.1. Coherent Diffraction Imaging (CDI)	37
2.2. Coherence	39
2.2.1. Longitudinal coherence length	39
2.2.2. Transverse coherence length	40
2.3. Diffraction by a crystal	40
2.3.1. Phase problem	41
2.4. Phase retrieval algorithms	42
2.5. Oversampling.....	43
2.6. Lattice displacement	44
2.7. Strain	45
2.8. Bragg CDI experiments	46
2.8.1. Bragg CDI measurement	46
2.8.2. Nanocrystal alignment.....	47
2.8.3. Data preparation for the reconstruction.....	48
2.9. Defects.....	49
2.9.1. Stacking fault	49
2.9.2. Twin domains	49
2.9.3. Dislocations and Burgers vector	50
2.9.4. Shockley partial dislocations	52
Conclusion	53
Goals and motivations	54
References	56
CHAPTER III: EXPERIMENTAL METHODS AND CHARACTERISATIONS.....	58
3.1. Introduction.....	59
3.2. Gold nanoparticles	59

3.2.1. Seed gold nanoparticles.....	59
3.2.2. Large gold nanoparticles	61
3.2.3. Ultra-small gold nanoparticles.....	64
3.3. Titania supports (TiO ₂)	66
3.3.1. TiO ₂ in anatase phase.....	66
3.3.2. TiO ₂ in mixed anatase and rutile phases.....	67
3.4. Supported catalysts.....	69
3.4.1. Catalysts preparation	69
3.4.2. Catalytic tests.....	72
3.5. Gold nanorods (Au NR)	74
Conclusions	76
References	77

CHAPTER IV: DEVELOPMENT OF AN *IN SITU* REACTOR TO IMAGE

CATALYSTS AT WORK IN THREE-DIMENSIONS BY BRAGG CDI.....	78
4.1 Introduction.....	79
4.2. Design and operation of the <i>in situ</i> reactor	79
4.2.1. Description of the reactor.....	79
4.2.2. Validation of the reactor	81
4.3. First Bragg CDI measurements of Au NP with the <i>in situ</i> reactor	83
4.3.1. Cristal beamline at SOLEIL	83
4.3.2. Data reconstructions	85
4.3.3. <i>In situ</i> conditions	85
4.4. Bragg CDI results and discussion.....	89
Conclusions	92
References	93

CHAPTER V: WATCHING A GOLD NANOCRYSTAL AT WORK: FROM THE CORE TO THE SURFACE OF THE NANOPARTICLE

5. Introduction.....	96
5.1. Bragg CDI experiments of Au NP	96
5.1.1. Beamline 34-ID-C at APS	96
5.1.2. Experimental conditions	97
5.1.2.1. Sample preparation.....	97
5.1.2.2. Sample environment	97

5.1.2.3. Bragg CDI measurements	99
5.1.2.4. <i>In situ</i> measurements	99
5.1.3. Data reconstructions	99
5.2. Pristine gold nanoparticle	100
5.3. Adsorbate-induced surface transformations	103
5.3.1. Morphology and lattice displacement	103
5.3.2. Strain analysis.....	106
5.4. <i>In situ</i> dynamics and catalytic activity	108
5.4.1. <i>In situ</i> surface dynamics	108
5.4.2. Nanotwin network formation	110
5.4.3. Strain energy density.....	115
Conclusions	116
References	116

CHAPTER VI: LOOKING *IN SITU* AT TWINNED NANOPARTICLES..... 119

6.1. Introduction.....	120
6.2. Twinned gold nanocrystal under air	120
6.2.1. Pristine twinned nanoparticle	120
6.2.2. Calcination treatment	123
6.3. Twin gold nanocrystal under CO/O ₂	124
Conclusions	127
References	128

CHAPTER VII: GOLD NANORODS STABILITY STUDIED BY NANODIFFRACTION 129

7.1. Introduction.....	130
7.2. X-ray nanodiffraction experiments of Au NR	131
7.2.1. 26-ID-C beamline at APS	131
7.2.2. Sample preparation	132
7.2.3. Gold nanorod alignment.....	133
7.3. Gold nanorods	134
7.3.1. Strain determination	137
Conclusions	139
References	139
Conclusions and future work.....	141

APPENDIX	144
ANNEX.....	147
Characterisation techniques.....	147
<i>A. Electron microscopy</i>	<i>147</i>
<i>B. UV-Vis.....</i>	<i>147</i>
<i>C. SAXS</i>	<i>148</i>
<i>D. XRD</i>	<i>149</i>

RESUMO EXPANDIDO

Em escala nanométrica, os materiais apresentam propriedades físico-químicas diferentes se comparadas com o estado bulk, devido à alta razão superfície/volume, característica de nanomateriais. Isso garante o emprego desses materiais em numerosas aplicações em áreas como sensores, na biomedicina, fabricação de dispositivos eletrônicos, etc. Por exemplo, nanopartículas de metais nobres suportadas em óxidos são bastante utilizadas em catálise heterogênea e são um tema amplamente estudado em nanociência.

A catálise é dita heterogênea quando a fase do catalisador é diferente da fase dos reagentes. Uma vez que esse tipo de catálise é extensivamente empregada em várias áreas da química e em muitos processos industriais, melhoras no desempenho de catalisadores heterogêneos são de suma importância no aprimoramento de processos industriais, no desenvolvimento de novas formas de energia e no controle da poluição ambiental. Um exemplo é o uso de catalisadores em veículos automotivos para a transformação química de gases poluentes que representam uma ameaça ao meio ambiente como hidrocarbonetos, monóxido de carbono (CO) e óxidos de nitrogênio (NO_x) em substâncias menos agressivas em termos de poluição ambiental, como CO₂, H₂O e N₂. Nesse cenário, o estudo da estrutura do catalisador e os mecanismos envolvidos na reação de catálise são passos importantes no processo de melhoramento no desempenho de catalisadores.

Dispersões coloidais de nanopartículas de ouro (Au NP) são muito estudadas devido as suas fascinantes propriedades físico-químicas: trata-se de dispersões estáveis que apresentam propriedades ópticas e magnéticas muito interessantes. O ouro quando no estado bulk é um metal inerte, mas quando nanoparticulado, apresenta excelentes propriedades catalíticas para uma ampla série de reações químicas. Esse fato é atribuído principalmente a abundância de átomos com menor número de coordenação em partículas pequenas, onde a adsorção dos reagentes, difusão e a dessorção dos produtos acontece.

Esses sítios ativos estão localizados nas bordas, esquinas e defeitos superficiais das nanopartículas. A reatividade dos catalisadores é ajustada pela deformação ("*strain*") presente na estrutura superficial, a qual é altamente dinâmica e consequentemente varia durante a ocorrência da reação. Nesse contexto, o *strain*

denota o deslocamento dos átomos na estrutura cristalina em relação às suas posições ideais. O desempenho catalítico pode ser melhorado através do entendimento da evolução do *strain* e a formação de defeitos tanto na superfície quanto na estrutura interna dos nanomateriais. Sob o ponto de vista da catálise, a fonte de *strain* durante o processo catalítico pode ser advinda da tensão (“*stress*”) induzida pela adsorção dos reagentes e da formação de defeitos internos/superficiais, os quais deslocam os átomos, resultando em compressão ou expansão da rede em relação à estrutura cristalina perfeita.

Além disso, as condições da reação afetam o comportamento dos catalisadores e seu desempenho. Assim, estudos sob condições controladas do ambiente reacional (“*in situ/operando*”) devem ser feitos. No entanto, técnicas de imageamento *in situ* em três dimensões (3D) que alcancem resolução nanométrica e determinação de *strain* simultaneamente são difíceis de serem aplicadas. Informações referentes a *strain* e defeitos em escala nanométrica podem ser obtidos com resolução atômica através de microscopia eletrônica, mas com severas restrições que incluem pressões reduzidas devido a profundidade de penetração curta dos elétrons, impedindo caracterizações *in operando*. Por outro lado, difração de raios-X de pó no regime de raios X duros permite a determinação de *strain* sob condições *in operando*; no entanto, as informações obtidas se referem a amostra como um todo, levando a informações que representam uma média de todas as estruturas presentes no pó.

A disponibilidade de raios X coerentes em fontes de luz síncrotron abre novos caminhos no campo de imageamento de nanomateriais, onde a técnica de Imageamento por Difração Coerente de Bragg (Bragg CDI) pode revelar a distribuição de *strain* de objetos nano e micrométricos em 3D em condições *in operando*. É importante destacar que a caracterização por Bragg CDI é possível em diversos ambientes realísticos (soluções aquosas, atmosferas reativas, altas temperaturas, etc.). Bragg CDI é uma técnica que se desenvolveu muito ao longo dos últimos 20 anos. Ela permite a reconstrução 3D de nano/micro objetos cristalinos e não cristalinos, como por exemplo, zeólitas, nanopartículas, tecidos biológicos, etc. Na técnica de difração, como a intensidade da radiação espalhada é o quadrado de sua amplitude, nós temos acesso a amplitude; no entanto, informações relativas a fase das ondas difratadas são perdidas nesse processo. Esse é o famoso “problema da fase”, bem conhecido na área de cristalografia. A radiação difratada pode ser

convertida na distribuição da densidade eletrônica do objeto espalhador através da aplicação de uma transformada de Fourier inversa. A amplitude da imagem obtida por Bragg CDI representa a densidade eletrônica da amostra e a fase corresponde a projeção do deslocamento dos átomos na estrutura cristalina. Assim, é possível reconstruir a partícula e obter informações referentes a morfologia e também sobre o deslocamento na posição dos átomos em relação as suas posições ideais na estrutura cristalina.

Neste trabalho, a técnica Bragg CDI é utilizada para revelar a dinâmica dos defeitos cristalinos e também o processo de facetamento que ocorre no sistema modelo sintetizado, isto é, nanopartículas de ouro suportadas em dióxido de titânio. Esse sistema foi estudado *in situ* durante a reação de oxidação de CO a pressão atmosférica. Essa reação catalítica é de suma importância ambiental uma vez que ela é utilizada no controle da poluição ambiental através da remoção de CO do sistema de exaustão de veículos motores, sendo considerada uma reação modelo.

Um reator dedicado para experimentos de Bragg CDI *in situ* e que pode funcionar a altas temperaturas também foi construído. Fazendo uso de um algoritmo para recuperar a fase através de um processo iterativo, a densidade eletrônica 3D de Bragg é reconstruída, sendo possível obter informações relativas a morfologia do objeto, e também ao campo de deslocamento dos átomos presentes na rede cristalina das nanopartículas de ouro. Para um dos experimentos, chegou-se a uma resolução espacial de 12 nm. As transformações superficiais que são induzidas pelo processo de adsorção e a quantificação do *stress* superficial também foram descritos, mostrando que a formação de redes geminadas de *nanotwins* desempenham um papel crucial nos mecanismos de deformação dos nanocristais e se correlacionam com o comportamento catalítico das nanopartículas de ouro suportadas em dióxido de titânio.

Outra parte desse trabalho consistiu na síntese de nanopartículas de ouro ultra-pequenas, extremamente relevantes do ponto de vista catalítico. Au NP muito pequenas apresentam excelente performance catalítica para a reação de oxidação do CO: a taxa de conversão de CO para Au NP no intervalo de tamanho de 2-4 nm é aumentada em duas ordens de magnitude se comparadas com Au NP maiores, demonstrando que o tamanho da nanopartícula é extremamente relevante para a ocorrência do processo catalítico. Para o preparo dessas nanopartículas foram

utilizados líquidos iônicos como agentes estabilizantes. Essa classe emergente de materiais tem crescido e atraído bastante atenção devido as suas propriedades físicas únicas como baixa volatilidade, alta estabilidade, baixa toxicidade e biodegradabilidade. De fato, diversos líquidos iônicos têm sido vastamente utilizados nas áreas de síntese orgânica, catálise, eletroquímica, eletrólitos poliméricos, na síntese “verde” de nanomateriais estáveis em água, em diversas reações químicas empregadas na indústria, etc.

Por fim, uma outra parte do trabalho desenvolvido durante esse doutorado foi o estudo de nanobastões (“*nanorods*”) de ouro utilizando como técnica principal nanodifração. O estudo aprofundado da estrutura e morfologia de *nanorods* de ouro é extremamente relevante para o emprego dos mesmos em uma ampla gama de aplicações que inclui dispositivos nanoeletrônicos e na área de biologia. Nessa tese, através do uso de microscopia eletrônica de varredura e nanodifração de raios X para caracterizar pequenos *nanorods* de ouro individuais, foi possível obter uma projeção da distribuição de *strain* dos cristais bem orientados na condição de Bragg. Essa última caracterização revelou a presença de um padrão de *strain* codificado na estrutura cristalina dos *nanorods* consistente com a chamada instabilidade Rayleigh, que leva a uma posterior segmentação de sua estrutura em esferas. Nossa metodologia mostra que a instabilidade está intrinsicamente presente nos *nanorods* em escala atômica e traz informações sobre a estabilidade estrutural dos mesmos, fazendo emergir uma compreensão nova para a engenharia de dispositivos que utilizam esse tipo de nanomaterial.

A principal inspiração do trabalho desenvolvido durante esse doutorado é a necessidade de conhecimento científico sobre técnicas advindas de radiação coerente uma vez que a nova fonte de luz síncrotron brasileira, o SIRIUS, terá diversas linhas de luz que oferecerão técnicas que utilizam luz coerente. O SIRIUS será uma máquina de quarta geração e está em estágio final de construção em Campinas-SP, sendo capaz de funcionar como um grande microscópio que oferecerá para a comunidade científica uma ampla série de métodos de caracterização pioneiros. Isso com certeza irá permitir o desenvolvimento de pesquisas no estado da arte, com potencialidades para resolver problemas científicos em diversas áreas como saúde, agricultura, energia, etc. Nesse aspecto, o presente trabalho abriu novos caminhos em relação a experiência/conhecimento adquiridos pelas pessoas envolvidas nesse projeto em

relação a técnica utilizada, aquisição/tratamento dos dados, conhecimento teórico/prática experimental, etc.

A linha de luz Cateretê, no SIRIUS, será dedicada a performance de CDI e está planejada para começar a funcionar em 2019. Quando a linha de luz de Cateretê estiver em operação, as técnicas de imagem de difração de raios X coerentes alcançarão a resolução espacial e temporal necessária para o estudo de dispositivos reais e as técnicas poderão ser aplicadas durante medições *in situ/operando*: tratamento térmico; uso de células dedicadas em diferentes atmosferas; estudo de carga/descarga em sistemas de baterias; dentre muitas outras possibilidades. Sem dúvida, isso expandirá os horizontes para a comunidade científica uma vez que no SIRIUS o fluxo coerente de fótons será 2 a 3 ordens de grandeza maior do que os disponíveis hoje em dia, o que significa uma grande melhora nas resoluções espacial e temporal.

CHAPTER I: Introduction

1.1. INTRODUCTION

At the nanometric scale, materials present different properties from the bulk state, mostly due to the remarkable property of high surface/volume ratio. Colloidal dispersions of gold nanoparticles (Au NP) have been vastly studied due to their fascinating physicochemical properties: they are the most stable (1), and present very interesting optical and magnetic properties. Although gold is inert in the bulk state, when in nanosized regime, gold presents excellent catalytic properties in a wide range of reactions. This fact is attributed to the abundance of a high number of low coordinated atoms in small nanoparticles, where the reactants' adsorption, diffusion and the products' desorption take place.

These active sites are localised at corners, edges and surface defects (2,3). The reactivity of the catalysts is tuned by the inherently strained surface structure (4,5) that is highly dynamic under reaction conditions (6–8). The improvement of catalytic processes can be achieved through the fine understanding of the evolution of strain and the formation of defects in both the surface and the inner core structure of the nanomaterials. In this context, strain denotes to the displacement of atoms in the crystal structure in relation to their ideal positions. For a catalyst, the source of strain during the catalytic process can be caused by the stress induced by the reactants adsorption and from internal defects, which displaces the atoms, resulting in compression or expansion from the ideal crystalline lattice.

Moreover, reaction conditions affect the catalysts behaviour and their performances. *In situ/operando* studies under relevant and controlled environmental conditions must be performed (9,10). However, *in situ* three-dimensional (3D) imaging techniques enabling nanometer-resolution and strain determination simultaneously are lacking. To date, strain and defect information at the nanoscale is accurately obtained by electron microscopy (11,12) with restrictions to reduced pressures due to the short penetration depth of electrons, preventing *in operando* characterisations. On the other hand, powder X-ray diffraction in the hard X-ray regime, enables to get strain structure data *in operando* conditions but on a large assembly of particles, yielding solely averaged information. The availability of coherent hard X-rays from synchrotron light sources opens new opportunities for imaging studies of nanomaterials (13,14), where Bragg coherent X-ray diffraction imaging (Bragg CDI) can reveal the strain distribution of single micro- and nano-sized objects (15–20) in 3D and *in operando* conditions. It is

worth mentioning that Bragg CDI is feasible in several realistic environments (aqueous solutions, reactive atmospheres, high temperatures...). The amplitude of the image obtained by Bragg CDI represents the electron density of the sample and the phase corresponds to the projection of the displacement of the crystal lattice. Thus, it is possible to reconstruct the particle and obtain information about the morphology and also information regarding the displacement of the atom's positions in relation to their ideal positions in the crystal lattice.

In this PhD work, Bragg CDI is used to unveil the defects dynamics and facetting process occurring on model gold nanocrystals supported on titanium dioxide during the CO oxidation reaction at atmospheric pressure. Because of its use in pollution control, by removing toxic CO from the exhaust of motor vehicles, this catalytic reaction is of high environmental and societal importance but also considered as a prototypical reaction for heterogeneous catalysis (22). We built a dedicated *in situ* heating reactor for *in situ* Bragg CDI. Applying iterative phase retrieval for coherent diffraction imaging (21), we reconstructed the 3D Bragg electron density and lattice displacement field of the gold nanocrystals with a spatial resolution down to 12 nm. We describe the adsorbate-induced surface transformation, quantify the surface stress and further show that nanotwins formation play a crucial role in the nanocrystal deformation mechanisms and correlates with the catalytic behaviour of the gold catalyst.

In this work we also synthesised ultra-small gold nanoparticles, which are interesting from the catalysis point of view (23). Very small Au NP present excellent catalytic performance for the CO oxidation reaction: the conversion rate of CO for Au NP in the 2-4 nm size range is increased by two orders of magnitude if compared with larger Au NP, demonstrating that the size of the nanoparticle is extremely relevant to the reaction rate (23). The approach we followed to prepare the ultra-small Au NP was based on the use of ionic liquids (IL) as stabilizers. This emergent class of material has grown and has attracted much attention due to their unique physical properties such as nonvolatility, high stability, low toxicity and biodegradability (24–26). Therefore, IL have been widely used in the area of organic synthesis, catalysis, electrochemistry, polymer electrolyte, surface active agents, nanoparticles green synthesis in water stable, chemical reactions mostly used in industry (27) and so forth.

Another part of this work regards the study of pristine gold nanorods. Comprehensive knowledge of the structure and morphology of thin gold nanorods is

crucial for its reliable employment in a wide range of applications such as in the nanoelectronics devices area and in biology field. In this thesis, by using scanning electron microscopy (SEM) and then scanning X-ray nanodiffraction to characterise few tenths of nanometers single gold nanorods, we were able to obtain a projection of the strain distribution over the Bragg well oriented gold crystals. This characterisation revealed the presence of a strain pattern encoded in the nanorods structure consistent with the so-called Rayleigh Instability compatible with a mechanism that leads to further rod segmentation into spheres. Our approach shows that the instability is intrinsically present in the rods on the atomic-scale and provides insights on the structural stability in very thin gold nanorods which brings up novel opportunities for nano-devices engineering.

REFERENCES

1. DANIEL, M.-C.; ASTRUC, D. Gold Nanoparticles: Assembly, Supramolecular Chemistry, Quantum-Size-Related Properties, and Applications toward Biology, Catalysis, and Nanotechnology. **Chemical Reviews**, v. 104, n. 1, p. 293–346, 2004.
2. RASHKEEV, S. N. et al. Role of the nanoscale in catalytic CO oxidation by supported Au and Pt nanostructures. **Physical Review B - Condensed Matter and Materials Physics**, v. 76, n. 3, p. 1–8, 2007.
3. WU, C. Y. et al. High-spatial-resolution mapping of catalytic reactions on single particles. **Nature**, v. 541, n. 7638, p. 511–515, 2017.
4. MAVRIKAKIS, M.; HAMMER, B.; NØRSKOV, J. K. Effect of Strain on the Reactivity of Metal Surfaces. **Physical Review Letters**, v. 81, n. 13, p. 2819–2822, 1998.
5. WALSH, M. J. et al. On the structural origin of the catalytic properties of inherently strained ultrasmall decahedral gold nanoparticles. **Nano Letters**, v. 12, n. 4, p. 2027–2031, 2012.
6. VENDELBO, S. B. et al. Visualization of oscillatory behaviour of Pt nanoparticles catalysing CO oxidation. **Nature Materials**, v. 13, n. 9, p. 884–890, 2014.
7. KALZ, K. F. et al. Future Challenges in Heterogeneous Catalysis: Understanding Catalysts under Dynamic Reaction Conditions. **ChemCatChem**, v. 9, n. 1, p. 17–29, 2017.
8. HE, Y. et al. Size-dependent dynamic structures of supported gold nanoparticles in CO oxidation reaction condition. **Proceedings of the National Academy of Sciences**, v. 115, n. 30, p. 7700–7705, 2018.

9. ROCHET, A. et al. Quick-XAS and Raman operando characterisation of a cobalt alumina-supported catalyst under realistic Fischer-Tropsch reaction conditions. **Catalysis Today**, v. 205, p. 94–100, 2013.
10. WECKHUYSEN, B. M. Snapshots of a working catalyst: possibilities and limitations of heterogeneous catalysts. **Inorganic Chemistry**, p. 97–110, 2002.
11. JOHNSON, C. L. et al. Effects of elastic anisotropy on strain distributions in decahedral gold nanoparticles. **Nature materials**, v. 7, n. 2, p. 120–4, 2008.
12. GORIS, B. et al. Measuring Lattice Strain in Three Dimensions through Electron Microscopy. **Nano Letters**, v. 15, n. 10, p. 6996–7001, 2015.
13. BAIER, S. et al. In Situ Ptychography of Heterogeneous Catalysts using Hard X-Rays: High Resolution Imaging at Ambient Pressure and Elevated Temperature. **Microscopy and Microanalysis**, v. 22, n. 1, p. 178–188, 2016.
14. WISE, A. M. et al. Nanoscale Chemical Imaging of an Individual Catalyst Particle with Soft X-ray Ptychography. **ACS Catalysis**, v. 6, n. 4, p. 2178–2181, 2016.
15. PFEIFER, M. A. et al. Three-dimensional mapping of a deformation field inside a nanocrystal. **Nature**, v. 442, n. 6, p. 63–66, 2006.
16. ROBINSON, I.; HARDER, R. Coherent X-ray diffraction imaging of strain at the nanoscale. **Nature Materials**, v. 8, n. 4, p. 291–298, 2009.
17. WATARI, M. et al. Differential stress induced by thiol adsorption on faceted nanocrystals. **Nature Materials**, v. 10, n. 11, p. 862–866, 2011.
18. KIM, D. et al. Active site localization of methane oxidation on Pt nanocrystals. **Nature Communications**, v. 9, n. 1, p. 3422, 2018.
19. YAU, A. et al. Materials science: Bragg coherent diffractive imaging of single-grain defect dynamics in polycrystalline films. **Science**, v. 356, n. 6339, p. 739–742, 2017.
20. ULVESTAD, U. et al. Topological defect dynamics in operando battery nanoparticles. **Science**, v. 348, n. 6241, p. 1344–1347, 2015.
21. MIAO, J. et al. Extending the methodology of X-ray crystallography to allow imaging of micrometre-sized non-crystalline specimens. **Nature**, v. 400, n. July, p. 342–344, 1999.
22. FREUND, H. J. et al. CO oxidation as a prototypical reaction for heterogeneous processes. **Angewandte Chemie - International Edition**, v. 50, n. 43, p. 10064–10094, 2011.
23. LOPEZ, N. On the origin of the catalytic activity of gold nanoparticles for low-temperature CO oxidation. **Journal of Catalysis**, v. 223, n. 1, p. 232–235, 2004.
24. DAVIS Jr, J. H., et al. **Ionic Liquids in Synthesis**. New York: Wiley-VCH Verlag GmbH & Co, 2003.

25. FEI, Z. et al. From dysfunction to bis-function: On the design and applications of functionalised ionic liquids. **Chemistry - A European Journal**, v. 12, n. 8, p. 2122–2130, 2006.
26. CASAL-DUJAT, L. et al. Gemini imidazolium amphiphiles for the synthesis, stabilization, and drug delivery from gold nanoparticles. **Langmuir**, v. 28, n. 5, p. 2368–2381, 2012.
27. PLECHKOVA, N. V; SEDDON, K. R. Applications of ionic liquids in the chemical industry. **Chemical Society reviews**, v. 37, p. 123–150, 2008.

CHAPTER II: Coherent Diffraction Imaging

2.1. COHERENT DIFFRACTION IMAGING (CDI)

Coherent Diffraction Imaging (CDI) is a technique that has been developed over the past 20 years. It is an imaging technique that allows the 3D reconstruction of crystalline or noncrystalline nano/microscale objects such as nanowires (1), zeolites (2), nanocrystals (3), biological tissues (4) and so on. The light source used in CDI must be coherent.

One mode of CDI is the so-called plane-wave CDI where the illumination is a coherent plane-wave radiation, which reaches the sample and the scattering pattern is collected in the far-field with a 2-dimensional detector, as shown in Figure 2.1 (a) (5). To obtain a 3D reconstruction, the sample is rotated and for each projection, a scattering pattern is acquired. The best resolution achieved in 3D to date using plane-wave CDI is 4 nm on gold patterned test sample (6).

As the irradiated object volume has to be smaller than the coherent volume of the X-ray source (7), there is a limitation for the size of the object to be possibly measured. This limitation can be circumvented by using the CDI mode called Ptychography, whose schematic representation is displayed in Figure 2.1 (b) (5). In this case, the methodology is the same as in plane-wave CDI, but extended objects (several tens of microns) can be measured by performing a 2D scanning (with a partial overlap between the points). Best resolution so far of 5 nm was reported by Shapiro *et al.* (8).

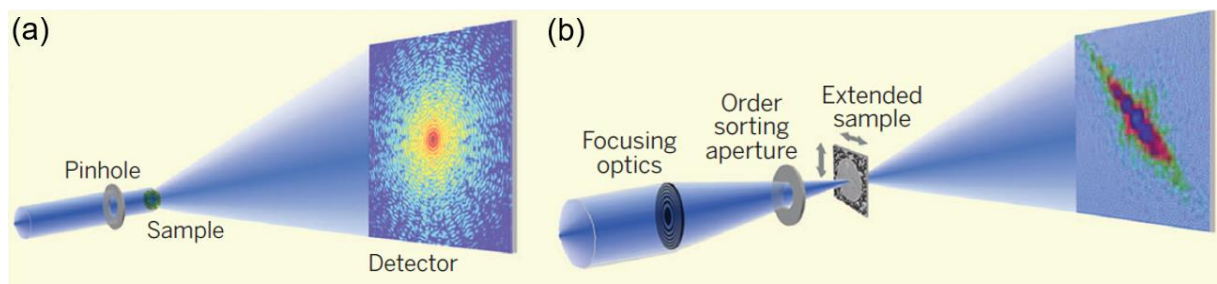
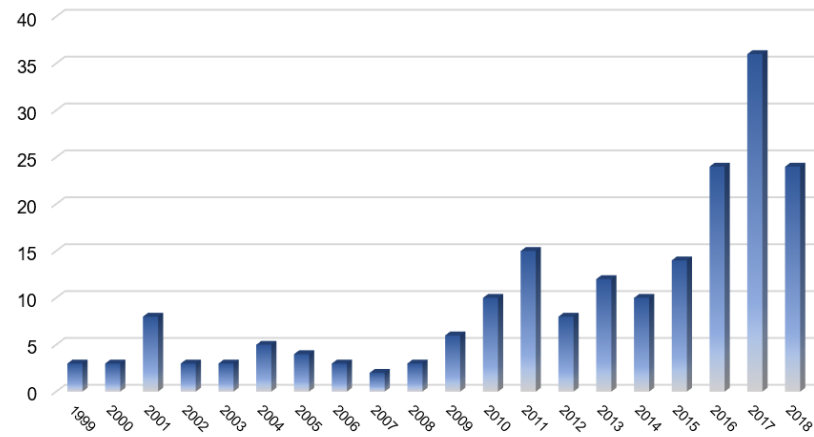


Figure 2.1. (a) Plane-wave CDI: a plane-wave illuminates fully the sample and the diffraction pattern is measured in the far-field. (b) Ptychography CDI: can be applied to Plane-wave-CDI to study extended specimens. Figure reproduced from reference (5).

The CDI mode used in this thesis is called Bragg CDI. In the Bragg geometry, one is also sensitive to lattice distortions with sub-angstrom sensitivity (9). The technique is ideal for studying surface and internal defects in nanocrystalline structure.

The use of this technique has been growing significantly over the last 20 years. Figure 2.2 shows the result of a search in the Web of Science database using the input terms “Bragg Coherent Diffraction Imaging” or “Bragg Coherent Diffractive Imaging”. The number of publications (a) and citations (b) over the last 20 years have significantly increased. A total of 196 works were published during these years and the sum of times cited was 3319. These numbers will keep on rising with the advent of new synchrotron sources such as SIRIUS, in Brazil, and the upgrades that have been done or are planned at several synchrotrons around the world.

(a) Number of publications per year



(b) Number of citations per year

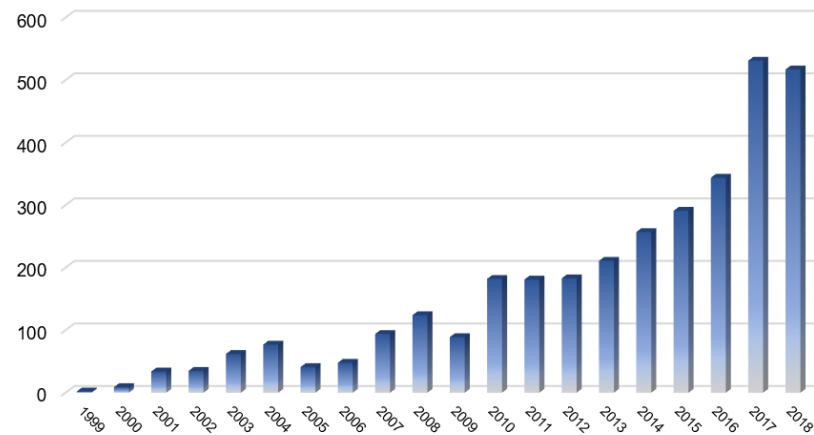


Figure 2.2. (a) Number of publications and (b) number of citations over the last 20 years in the Web of Science database using the input terms “Bragg Coherent Diffraction Imaging” or “Bragg Coherent Diffractive Imaging”.

2.2. COHERENCE

As highlighted before, Bragg CDI needs coherent X-ray radiation. 4th generation synchrotron facilities are emerging as the coherence properties of this source are tremendously improved. At SIRIUS, that is a 4th generation synchrotron in construction in Campinas, Brazil, the Cateretê and Carnaúba beamlines will be the first to propose coherent based experiments with such high coherent X-ray properties. The coherence of the X-ray beam can be defined by two physical quantities: the longitudinal coherence length, L_L , and the transverse (X and Y) coherence lengths, L_T .

2.2.1. Longitudinal coherence length

The longitudinal coherence length (L_L) is defined as the distance between two wavefronts, initially in phase, until they are totally out of phase, as shown in the schematic in Figure 2.3 (10). The longitudinal coherence length is:

$$L_L = \frac{1}{2} \frac{\lambda^2}{\Delta\lambda} \quad (1)$$

Therefore, the longitudinal coherence length is directly related to the monochromatisation device used on the beamline.

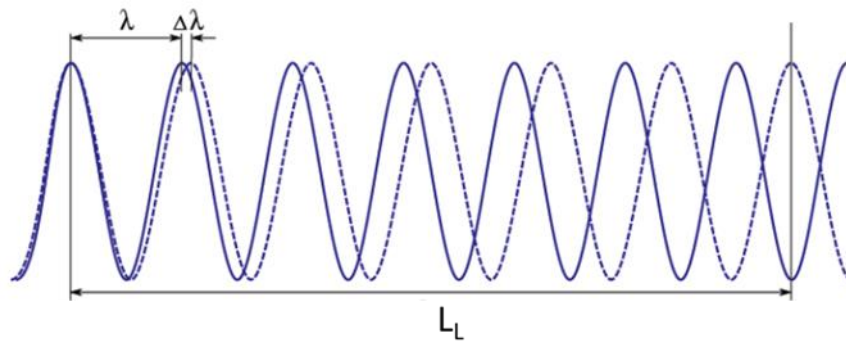


Figure 2.3. Illustration of the longitudinal coherence length (L_L), value representing the length which the waves (initially in phase) become shifted by π . Figure from reference (10).

2.2.2. Transverse coherence length

The transverse coherence lengths (L_T) are defining the dimensions of the coherent illumination of the beam. Let's consider the monochromatic waves 1 and 2 in Figure 2.4, propagating in different directions, that are displaced by the difference $\Delta\theta$. The distance from point P to where the difference between the waves is 2π (point K in this case) is the so-called spatial coherence length. From Figure 2.4, L_T is defined by:

$$L_T = \frac{\lambda}{\Delta\theta} = \frac{\lambda R}{w} \quad (2)$$

The specimen under study needs thus to be smaller than the transverse coherent lengths, L_{Tx} and L_{Ty} . From equation (2), large transverse coherence lengths values will be reached by using small size sources and by increasing the source-sample distance.

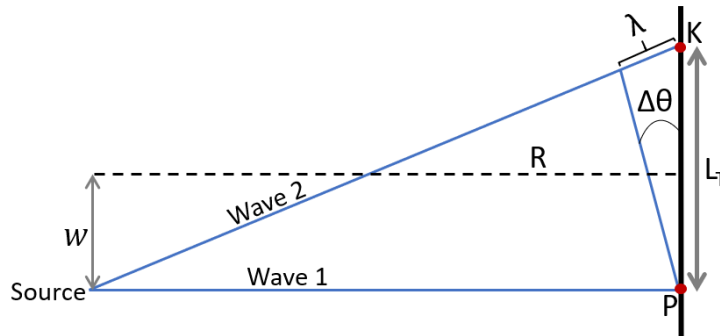


Figure 2.4. Illustration representing the transverse coherence length (L_T).

2.3. DIFFRACTION BY A CRYSTAL

For the occurrence of diffraction phenomenon, the wavelength of the incoming radiation is comparable with the distance between the scattering species. As the X-rays are electromagnetic radiation whose wavelength is in the order of 10^{-10} m, this radiation is diffracted by crystals once the distance between the planes of the crystalline lattice is comparable to the X-ray wavelength. When X-rays illuminate a crystal, they are scattered by the electrons of the atoms forming the crystal. Given the periodicity of the crystal lattice, it acts as a diffraction grating, and, at determined

directions, the diffracted radiation will interfere constructively, which gives rise to the diffraction peaks. The conditions for constructive interference of the scattered waves by the crystal planes are given by the well-known Bragg law:

$$n\lambda = 2d\sin\theta \quad (3)$$

where, $n = 1, 2, 3$, etc. is the order, λ is the wavelength of the radiation, d is the lattice spacing and θ is the angle between the incident X-rays and the crystal plane. Figure 2.5 (a) shows the schematic of the diffraction phenomenon, supposing that the incident radiation is coherent. For constructive interference of the elastically scattered X-ray from the lattice planes to occur, the optical path length difference between the successive scattered waves must be an integer multiple n of the wavelength of the X-ray that is used.

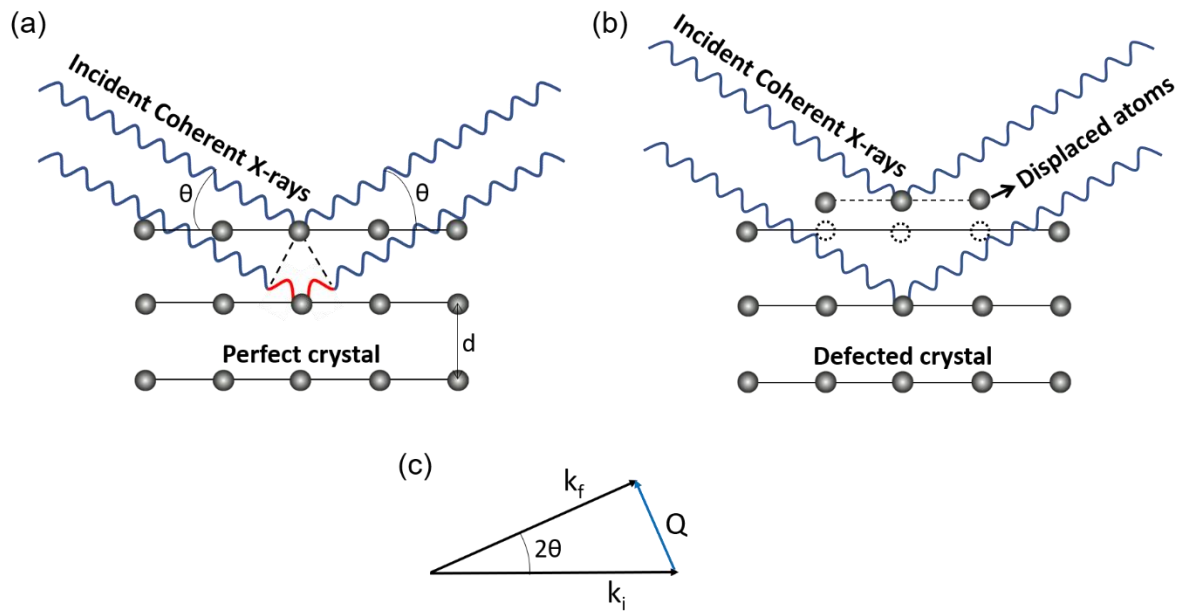


Figure 2.5. (a) Diffraction of X-rays for a perfect crystalline structure. (b) Diffraction of X-rays for a realistic case of a defected structure. (c) The Q vector is the vectorial difference between the incident and scattered vectors (k_i and k_f , respectively).

2.3.1. Phase problem

In diffraction, as the intensity of the scattered radiation is the square of the amplitude, we have access to the amplitude, but information regarding the phase of

the waves is lost in this process. This is the “phase problem”, well-known in crystallography. The recorded diffracted radiation can be converted back into the electron density distribution of the diffracting object by applying an inverse Fourier transform. The phase change in a defected crystal can be visualised by the simplified schematic shown in Figure 2.5 (b). In the as explained case (a), the X-rays reach a non-defective crystal and, it carries a constant phase relationship after the diffraction phenomenon. In this ideal case, assuming that the radiation is coherent, according to the inversion symmetry of the magnitude of the Fourier transform of a real object (11), the crystal would give rise to a symmetric coherent diffraction pattern. Now, let's consider the realistic case where the crystal is not perfect and there are several displaced atoms on its structure as exemplified in (b). In this case, the phase relationship is changed due to the displaced atoms and the coherent diffraction pattern would be asymmetric. In (c), the scattering vector Q is represented. It is the difference between the incoming wavevector k_i and the outgoing one, k_f .

2.4. PHASE RETRIEVAL ALGORITHMS

The recovery of both amplitude and phase of the diffracted radiation allows one to image the object that diffracts the radiation through an inverse Fourier transform. Making sure that the diffraction data is oversampled and that the object is isolated, the algorithm can be used for the phase retrieval via an iterative way. The phase retrieval algorithms most used for CDI data are primarily based on the iterative method of Gerchberg-Saxton, which was originally developed for the electron microscopy (EM) imaging case where the measurement is done in both real and reciprocal spaces (12). With the availability of fast Fourier Transform (FFT), switching back and forth between both spaces, the amplitude and phase of the diffracted radiation can be recovered from the recorded intensity (13). Figure 2.6 displays the basic principle of operation of this algorithm. At first, a real space estimate - $g_n(x)$ - of the object is done considering a random phase set. A FFT is then calculated, which gives rise to the diffraction pattern - $G_n(u)$ - that will be compared with the experimental one. By imposing a Fourier constraint, this gives rise to $G'_n(u)$. An inverse FFT of the reciprocal space of the object is then calculated, which generates $g'_n(x)$. A real space constraint is executed, which results in a new estimate in real space for the object. This iterative process is repeated

until convergence is attained, which means the constraints in both real and Fourier domains are satisfied. For a convergent solution, the difference between the measured and retrieved intensity, usually reaches values smaller than 10^{-3} . The number of times that this process happens is called “number of iterations”. The algorithm works trying to minimise the difference between the measured diffraction pattern and the one generated by the hypothetical reconstructed object, by changing progressively this object (both its amplitude and phase).

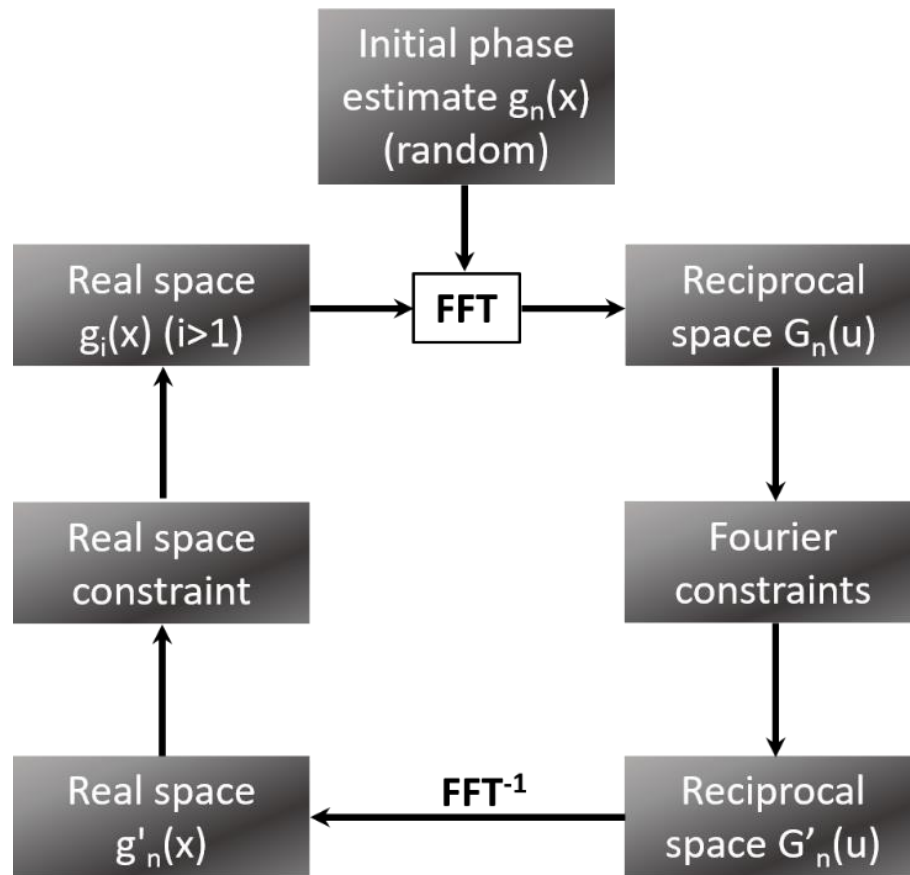


Figure 2.6. Iterative phase retrieval based on the Gerchberg-Saxton algorithm (12); n is the iteration number.

2.5. OVERSAMPLING

The oversampling criteria is related to the region known as the support, which defines the boundary which encloses the scattering object. In the case of a two-fold oversampling, the quantity of unknowns in the real space is equal to the quantity of

measured diffraction intensities on the detector. This is a requirement for the reconstruction work. The oversampling ratio can be defined as:

$$\sigma = \frac{\text{total region}}{\text{electron density region}} \quad (4)$$

where the total region is the electron density region + no-density region (the support area) (14). For retrieving the phase from a diffraction pattern, the oversampling ratio must be greater than two. In CDI, the oversampling condition is achieved by making sure that the number of pixels per fringe in the detector is greater than two. Given that the fringe spacing is $\frac{\lambda D}{S}$, where λ is the wavelength of the X-rays, D is the sample-detector distance and S is the size of the sample, the oversampling ratio is defined as:

$$\sigma = \frac{\lambda D}{S \cdot \text{detector pixel size}} \quad (5)$$

Therefore, by increasing λ and the sample-detector distance, the oversampling ratio is increased.

2.6. LATTICE DISPLACEMENT

The imaginary part, the phase shift Φ , provides an image of the displacement u of the crystal lattice projected along the scattering vector of the measured Bragg spot via the following equation:

$$\Phi = G u \quad (6)$$

where G is the scattering vector and u the displacement field (15). G is also defined by $G = \frac{2\pi}{d}$ where d is the lattice spacing for the studied Bragg peak. Replacing G in equation (6) it is clear that the phase changes by 2π for every increase of u by one lattice spacing. As the displacement field represents the distortions in the crystalline structure, it is possible to get insights about the defects present in the structure.

2.7. STRAIN

The concept of strain in crystal lattices is related with the shifts of the atoms in relation to their equilibrium positions. Figure 2.7 shows an example of a strained structure in a simplified crystal lattice (for better visualisation, the atoms are not shown), where the red structure represents the displaced atoms by the quantity Δd in relation to the perfect lattice spacing d . There are several reasons for the appearance of strain in the crystalline structure, and for the particular case of this work, the strain induced from internal defects (for example, dislocations inside the crystals) and from forces applied to the surface of the crystal (stress, for example) are of particular relevance.

Let's define strain in terms of vectorial notation: consider the original position of an atom in the crystal lattice as the ideal position and, if the atom is displaced, the points will be displaced by Δd , as shown in Figure 2.7 and, the difference between the strained and original positions is called displacement vector, represented by the notation \vec{u} . From this, the strain can be defined as the symmetric part of the gradient of the displacement. If x_i and x_j are both components of the position in the ideal lattice, the strain tensor is:

$$\epsilon_{ij} = \frac{1}{2} \left(\frac{\partial u_i}{\partial x_j} + \frac{\partial u_j}{\partial x_i} \right) \quad (7)$$

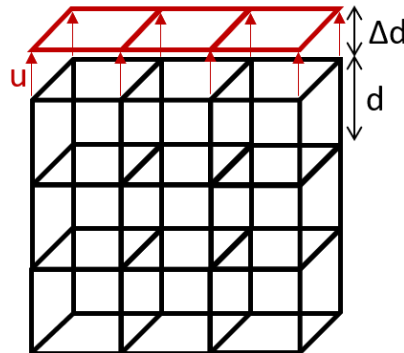


Figure 2.7. Schematic of a crystalline structure with displaced atoms by Δd (in red), showing the displacement vector \vec{u} .

The lattice spacing is determined applying the Bragg equation and the strain is defined as:

$$\frac{\Delta d}{d} = \frac{d_{exp} - d_{theo}}{d_{theo}} \quad (8)$$

where $\frac{\Delta d}{d}$ is the strain, d_{exp} is the experimentally measured lattice spacing and d_{theo} is the theoretical lattice spacing. As the 2θ position changes as function of the presence of strain in the crystal, having measured the relative Bragg positions we can determine the relative variations of the strain distribution across the sample.

From the phase shift, one can obtain information on the strain field of the crystal lattice (16). The 3D strain distribution along the measurement direction (here (111)) is obtained by taking the derivative of the displacement field resulting from algorithmic phase reconstruction. It is defined by the formula:

$$\varepsilon = \frac{\partial u_{111}(r)}{\partial x_{111}} \quad (9)$$

where $u_{111}(r)$ is the displacement field.

Given that the phase shift is a scalar product of the scattering vector and displacement field (equation (6)), only one component of the displacement field is measured for a given Q, which is the projection of the displacement field onto the Q vector. Hence, the full strain tensor is obtained if the diffraction of at least three non-coplanar Bragg peaks are measured.

2.8. BRAGG CDI EXPERIMENTS

2.8.1. Bragg CDI measurement

In Bragg CDI, the sample is illuminated by a coherent plane wave beam, where the intensity of the diffracted radiation for a given Bragg peak is recorded in the detector. The rocking curve is then measured, where the crystal is rotated around the 2θ angle in a short interval by using small step angles and measuring a sequence of successive 2D diffraction patterns for each angle. The stacking of these 2D diffraction

patterns yields the 3D Bragg peak. The structure information of the object is encoded in the diffraction speckles. The 3D Bragg peak is the main input file used in the algorithm for the nanoparticle reconstruction.

2.8.2. Nanocrystal alignment

Figure 2.8 presents a schematic of the crystal geometry for aligning the nanocrystal to the center of rotation. The alignment procedure is the following: if the crystal is not at the center of rotation along the x-ray propagation direction (y axis in this case), when rotating the crystal by a portion of a degree, the diffracting crystal will be out of the beam. In the second frame in this Figure, one should adjust the sample in the direction of x and z in order to move the crystal back into the X-ray beam. This shows where is the relative position of the object in relation to the center of rotation (along the y-axis). Then, one needs to move the crystal along the beam closer to the center of rotation. This procedure must be repeated until the crystal rocking curve presents a smooth Gaussian shape without abrupt intensity decrease (17).

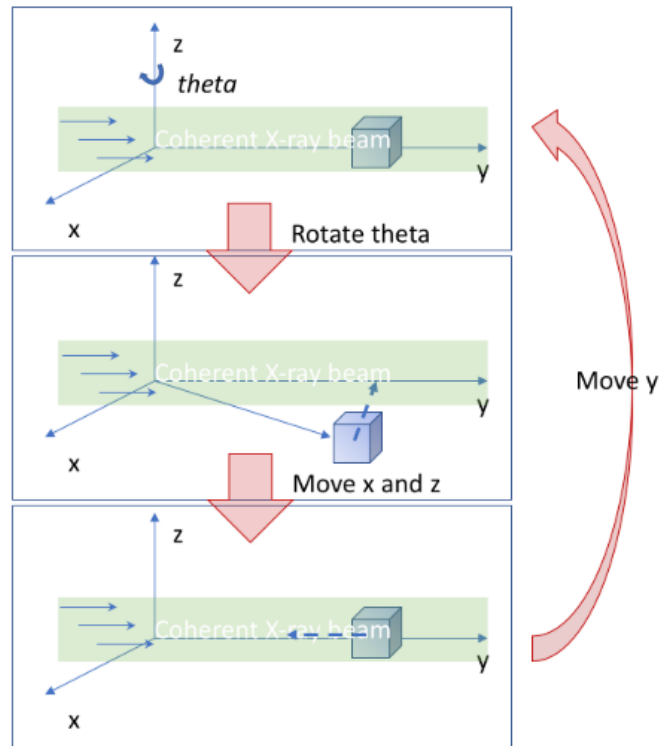


Figure 2.8. Schematic of the sample alignment to the center of rotation. Figure from reference (17).

This procedure is used to align the sample in the beginning of the experiment but also during the heating treatment in order to track the nanoparticle during heating ramps. Indeed, whilst increasing the temperature, the *in situ* setup can face a thermal expansion leading to a drift of the sample including loss from the beam. That is why, during the heating/cooling ramps, this alignment procedure is used to recover the orientation and position of the nanoparticle to get the maximum intensity of the signal before performing the rocking curves.

2.8.3. Data preparation for the reconstruction

One criterion used to select a good diffraction pattern is that this pattern is isolated on the area detector. If there are one or more diffraction patterns derived from different objects superposing, the algorithm is not capable of differentiating them during the reconstruction process and this approach doesn't work anymore. Figure 2.9 shows a 2D diffraction pattern with a main signal in its center and areas indicated by red arrows where “alien” diffraction signals are observed. Those signals coming from different crystals should be removed before using the data for reconstruction. This is done by cropping the 2D diffraction image and using in the phase-retrieval algorithm only the signal inside the red square.

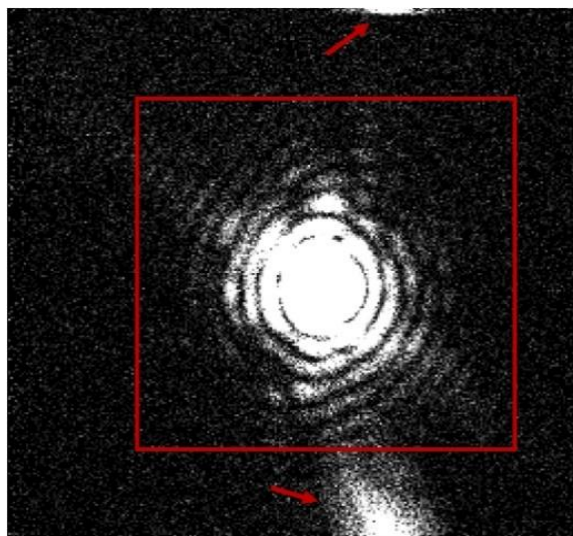


Figure 2.9. Example of a 2D Bragg peak for the center of the rocking curve. The red square represents the cropped area and the red arrows point to scattering contributions from different objects.

2.9. DEFECTS

2.9.1. Stacking fault

Some of the most common defects present in crystalline materials are stacking faults. They are defined as imperfections where the stacking sequence of the atomic layers in the crystal is interrupted. For face centered cubic (fcc) crystalline structures, which is the case for gold, the crystallographic planes packing of $\{111\}$, for instance, follows the sequence ABCABCABC..., which can change in the case of the defected structure. For fcc structures, there are two main types of stacking faults: intrinsic and extrinsic as shown in Figure 2.10 (a) and (b), respectively. In the intrinsic type, one atomic layer, C in this case, is removed from the structure and, in the extrinsic type, an additional atomic layer, A in this case, is added to the structure (18). Both removed and added atomic layers are indicated by a black arrow in the Figure.

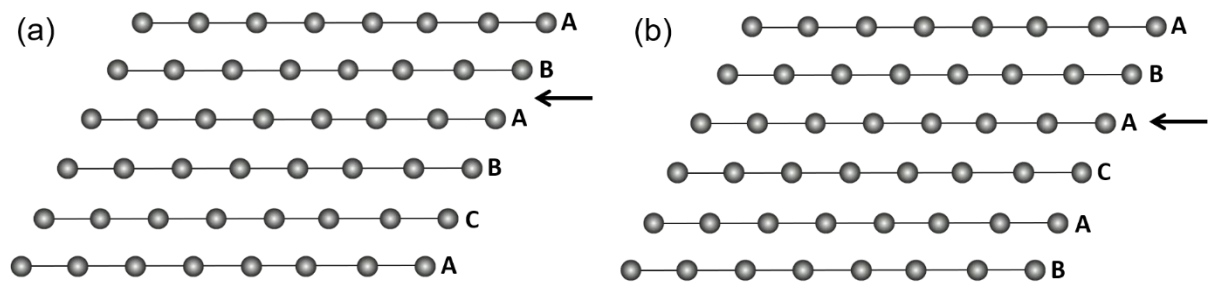


Figure 2.10. Representation of the different types of stacking faults present in a fcc structure: (a) intrinsic and (b) extrinsic.

2.9.2. Twin domains

The other common defect present in crystalline structures is the formation of the so-called twin domains, which occurs when the crystal shows two packing sequences, one the mirror of the other. For example, in the fcc structure of the $\{111\}$ planes, the formation of twin domains can happen through the sequence **ABCABC****BAC**, where the layers in grey bold represent the original crystal planes and the black bold sequence represent the twin layers, following a mirrored order in relation to the original crystal (18). A schematic representing a twin domain formation is shown in Figure 2.11, and the dashed red line represent the plane where the twin will be formed: the atoms below are the original crystal, called “parent crystal” and the atoms above are the

twinned structure, called “twin crystal”. It is noteworthy that the twin formation implies the creation of stacking faults in the crystal. In the schematic representation of Figure 2.11, for example, in the twin portion, an A layer is missing (between C and B) and right after, a C layer is missing as well (between B and A). Twin domains in crystalline structures are very important as they can influence several physicochemical properties, as will be discussed in Chapter VI.

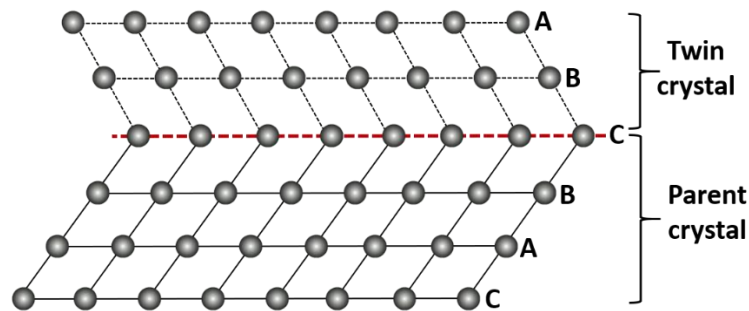


Figure 2.11. Schematic of a twin domain formation.

2.9.3. Dislocations and Burgers vector

Dislocations are another type of common defect in crystal structures. These defects are generated by atomic planes sliding over each other, caused when a stress is applied to the crystal, as displayed in Figure 2.12. There are two main types of dislocations: edge and screw. The edge dislocation is a 1D line defect where an extra half-plane of atoms is introduced in the crystalline structure, distorting the atomic layers in the surrounding region, as shown in Figure 2.13. This defect is represented by the symbol \perp . A screw dislocation is much harder to imagine. Consider the 3D perfect crystalline structure represented in a simplified way in Figure 2.14 (a). A screw dislocation is formed when the crystal structure slips along a plane and goes part way through the crystal, as shown in (b). The dislocation is usually represented by the so-called Burgers circuit, which is an atom-to-atom path in the crystalline structure that ends up in a closed loop (18). The Burgers vector is the vector placed from the last to the initial point of the circuit in the crystal. Figure 2.14 shows the Burgers circuit for both, the perfect and the defected structure as the MNOPQ way. For the crystal with the dislocation, the looping way is closed, but if we try the same with the defect-free

crystal, it is not possible to close the circuit. This means that the first case should have one or more dislocations (18).

The Burgers vector just defined in Figure 2.14 (b) is a lattice translation vector and the dislocation derived from this type of vector is a perfect dislocation. The Burgers vector is defined using the same indices from crystallography. Consider for example a lattice vector from the origin to the center of a body-centered cubic cell as shown in Figure 2.15, in red. The vector is defined as $a/2$ for all the axis and the correct notation is $b = \frac{1}{2} [111]$. The magnitude of the Burgers vector b is mathematically defined as:

$$b = \sqrt{\left(\frac{a^2}{4} + \frac{a^2}{4} + \frac{a^2}{4}\right)} = \frac{a\sqrt{3}}{2} \quad (10)$$

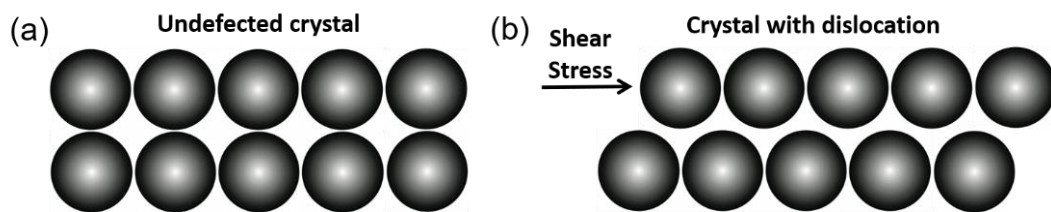


Figure 2.12. (a) Schematic representing a perfect crystal, in the absence of dislocation. (b) When shear stress is applied in the crystal, the structure is plastically deformed provoking a slide of the atomic planes over each other.

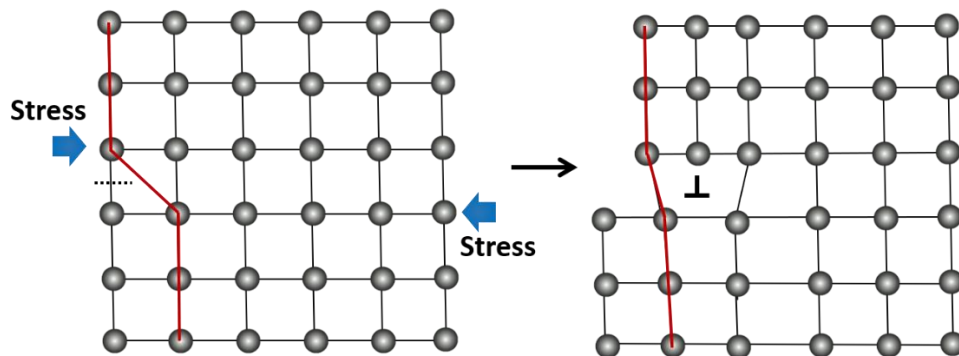


Figure 2.13. Representative schematic of an edge dislocation. When shear stress (represented by the blue arrows) is applied to the crystalline structure, the metallic bond can break, and a new bond is created, as shown by the red lines. The symbol \perp represents the edge dislocation.

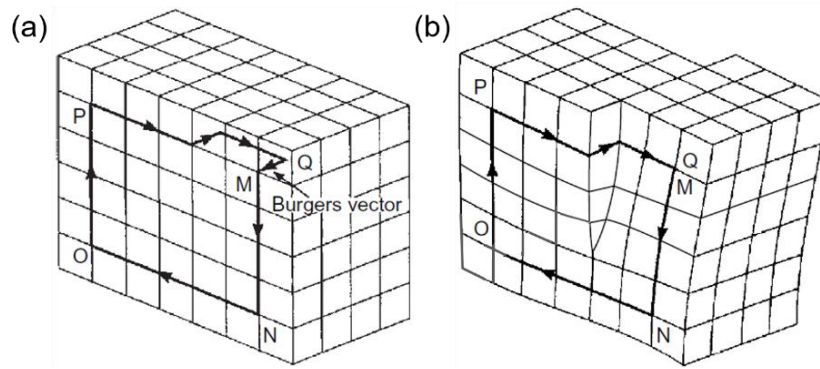


Figure 2.14. Burgers circuit for (a) a perfect crystal and (b) a crystal with screw dislocation. Figure from reference (18).

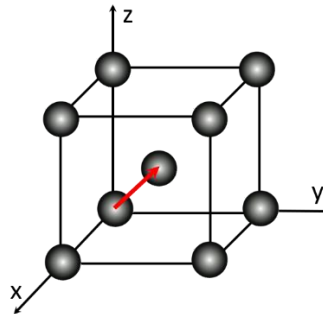


Figure 2.15. Burgers vector (in red) from the origin to the center of a body-centered cubic cell.

2.9.4. Shockley partial dislocations

The energy contained in a dislocation is proportional to the Burgers vector to the square (b^2) (18). Given this, the smallest energy of a dislocation and therefore the most likely to occur in face-centered cubic structures is the one of the $\frac{1}{2} \langle 110 \rangle$. As this is a lattice translation vector, this is a perfect dislocation. Perfect dislocations can split into two partial dislocations; a very common and important partial is the so-called Shockley partial dislocation. The creation of this partial dislocation is displayed in Figure 2.16 (18), where the right part of the schematic represents a perfect crystalline structure and in the left part, the atoms were slipped in relation to the original positions: the original A atom slips to the B layer position, the B atom goes to C and so on. This slipping process results in two main changes: i. a stacking fault is formed as there is an A layer of atoms missing and ii. the generation of a Shockley type partial dislocation. Consider the schematic representation of $\{111\}$ planes in fcc structures in Figure 2.17. If the layers are moved through a slipping process, the energy required for going from

B straight to the other B position (b_1 vector) is higher than the one required for the way B – C – B (b_2 and b_3 vectors). In this schematic, the b_1 vector represents the movement of a perfect dislocation and the b_2 and b_3 vectors are two Shockley partial dislocations. This implies that the slipping movement is more favourable as the two partial dislocations instead of the perfect one.

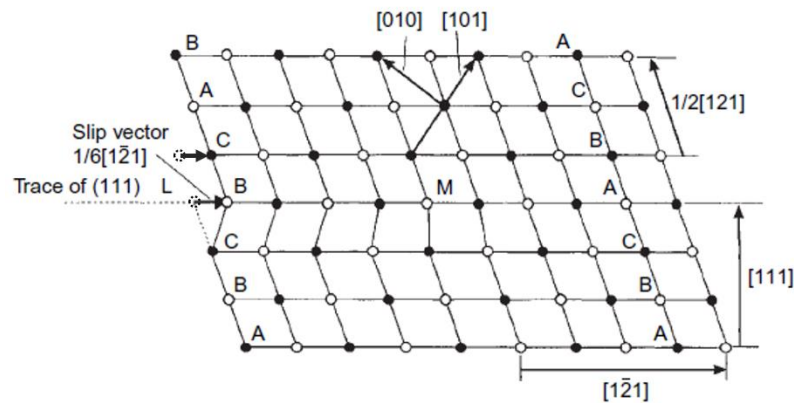


Figure 2.16. Schematic representation of a Shockley partial dislocation. Figure from reference (18).

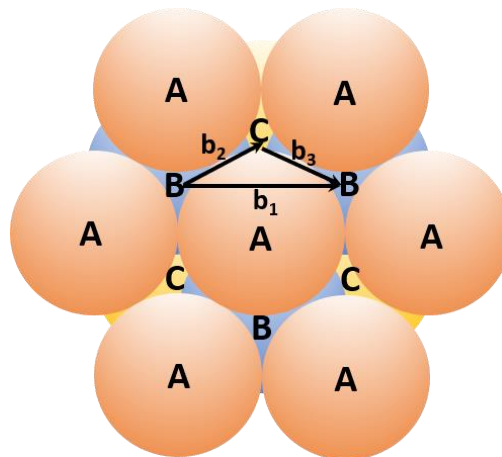


Figure 2.17. Possible slip ways of $\{111\}$ planes in fcc crystals: b_1 vector represents a perfect dislocation and b_2/b_3 vectors, partial dislocations. Figure adapted from reference (18).

CONCLUSION

In this chapter I showed the main basics of CDI. When in the Bragg geometry, the technique can be used to measure the strain in 3D, which gives us information about the lattice distortions and its impact on the materials performance can be

investigated. In the particular case of catalysis, as the presence of strain does affect the catalytic properties, increasing or decreasing the number of catalytic sites, the technique presents unprecedented capabilities for catalysts characterisation. One remarkable feature is that the technique permits the use of reactive environments, also crucial from the catalysis point of view. The methodology relies on iterative phase retrieval algorithms to solve the phase problem and create real space images.

As strain is present in crystalline structures, measure the strain in nanomaterials is particularly important for correlating it with the material's properties. X-ray techniques are the most widely used to investigate strain because of its accuracy. Figure 2.18 (19) brings up few techniques used for the characterisation of strain. In the inset text in this Figure, there are few advantages and drawbacks of each of them. In the case of this thesis, CDI was the technique used to extract strain information and we made use of all the advantages cited in the Figure.

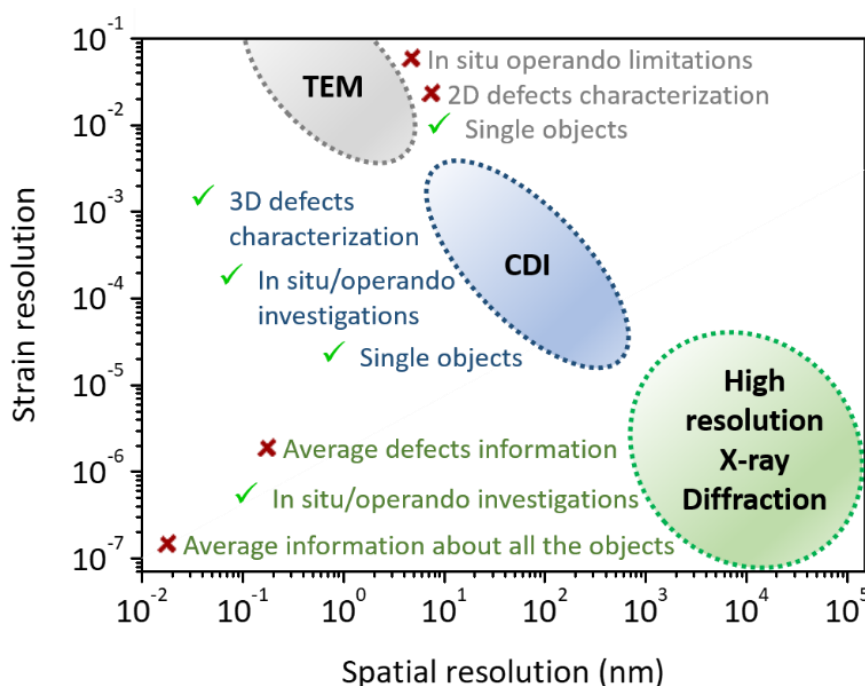


Figure 2.18. Reachable strain resolution for TEM, CDI and High resolution X-ray diffraction. The graphic brings the main advantages and drawbacks of each of them. Figure adapted from reference (19).

GOALS AND MOTIVATIONS

Given the importance of obtaining information about the 3D strain distribution in catalysts under working conditions, the main aim of this work is to investigate isolated

gold nanoparticles supported on titanium dioxide through Bragg coherent diffraction imaging (Bragg CDI) to follow the changes on the morphology and the 3D strain distribution over the nanoparticle during the CO oxidation, used in this work as a model catalytic reaction. We aim to link the strain distribution with the catalytic activity during the reaction occurrence.

The specific objectives of this work were:

- Given the current resolution limit for the technique, where is not possible to measure small objects (which would be better from the catalysis point of view), the first step of this part of the work was to synthesise gold nanoparticles of 50 and 120 nm average diameter and support them on two different phases of titanium dioxide. After the synthesis procedure, we pre-characterise the catalysts before the Bragg CDI experiment;
- Measure the catalytic activity of the catalysts for the CO oxidation reaction in order to check if the samples are catalytically active;
- Given the importance of size for Au NP in their catalysis performance, we aim to produce ultra-small gold nanoparticles by following a “green” chemical route using as stabilizing agent two types of ionic liquids and test their performance for the CO oxidation reaction;
- Regarding the second part of this work (the characterisation of gold nanorods by X-ray nanodiffraction), our main aim is to map the strain distribution over single gold nanorods, given its interesting optical properties, mostly due to the presence of two surface plasmon resonance (SPR) bands (the transverse and longitudinal modes) and also the particular trend that rod-shaped objects have to spheroidize due to the so-called Rayleigh instability.

A remarkable inspiration of this work is the need of scientific insights about techniques arising from coherent radiation since the upcoming new Brazilian synchrotron, SIRIUS, will have coherent related techniques. SIRIUS will be a 4th generation machine and is in final stage of construction in Campinas-SP, capable of working as a great microscope and will offer to the scientific community a wide range of pioneering characterisation methods. This will allow the development of state-of-art research, with potentialities to solve several scientific problems in areas such as

health, agriculture, energy, etc. In this respect, the current work paved the way in the scientific background about coherent derived techniques for many people involved on it, regarding several objects: the techniques itself, sample preparation, data treatment and the theoretical/experimental background behind the technique.

REFERENCES

1. DIAZ, A. et al. Coherent diffraction imaging of a single epitaxial InAs nanowire using a focused x-ray beam. **Physical Review B**, v. 79, n. 12, 2009.
2. CHA, W. et al. Core-shell strain structure of zeolite microcrystals. **Nature Materials**, v. 12, n. 8, p. 729–734, 2013.
3. ULVESTAD, A. et al. In Situ 3D Imaging of Catalysis Induced Strain in Gold Nanoparticles. **The Journal of Physical Chemistry Letters**, v. 7, n. 15, p. 3008–3013, 2016.
4. SHAHMORADIAN, S. H. et al. Three-dimensional imaging of biological tissue by cryo x-ray ptychography. **Scientific Reports**, v. 7, n. 1, p. 1–12, 2017.
5. MIAO, J. et al. Beyond crystallography: diffractive imaging using coherent x-ray light sources. **Science**, v. 348, n. 6234, p. 530–5, 2015.
6. CHERUKARA, M. J.; CHA, W.; HARDER, R. J. Anisotropic nano-scale resolution in 3D Bragg coherent diffraction imaging. **Applied Physics Letters**, v. 113, n. 20, p. 203101, 2018.
7. ALS-NIELSEN, J.; MCMORROW, D. **Elements of Modern X-ray Physics**. Chichester: John Wiley & Sons Ltd, 2011.
8. SHAPIRO, D. A. et al. Chemical composition mapping with nanometre resolution by soft X-ray microscopy. **Nature Photonics**, v. 8, n. 10, p. 765–769, 2014.
9. LEAKE, S. J. et al. Longitudinal coherence function in X-ray imaging of crystals. **Optics Express**, v. 17, n. 18, p. 15853, 2009.
10. VEEN, F. VAN DER; PFEIFFER, F. Coherent x-ray scattering. **Journal of Physics: Condensed Matter**, v. 16, p. 5003–5030, 2004.
11. ROBINSON, I. Nanoparticle Structure by Coherent X-ray Diffraction. **Journal of the Physical Society of Japan**, v. 82, p. 1–7, 2013.
12. GERCHBERG, R. W.; SAXTON, W. O. A practical algorithm for the determination of phase from image and diffraction plane pictures. **Optik**, v. 35, n. 2, p. 237–246, 1972.
13. CLARK, J. N. et al. Three-dimensional imaging of dislocation propagation during crystal growth and dissolution. **Nature Materials**, v. 14, n. 8, p. 780–784, 2015.

14. MIAO, J.; KIRZ, J.; SAYRE, D. The oversampling phasing method. **Acta Crystallographica Section D Biological Crystallography**, v. 56, n. 10, p. 1312–1315, 2000.
15. ROBINSON, I.; HARDER, R. Coherent X-ray diffraction imaging of strain at the nanoscale. **Nature Materials**, v. 8, p. 291–298, 2009.
16. PFEIFER, M. A. et al. Three-dimensional mapping of a deformation field inside a nanocrystal. **Nature**, v. 442, n. 7098, p. 63–66, 2006.
17. LI, L. et al. Methods for operando coherent X-ray diffraction of battery materials at the Advanced Photon Source. **Journal of Synchrotron Radiation**, v. 26, n. 1, p. 220–229, 2019.
18. HULL, D.; BACON, D. J. **Introduction to dislocations**. Amsterdam: Elsevier/Butterworth-Heinemann, 2011.
19. DIMPER, R. et al. Technical Design Study ESRF Upgrade programme Phase II (2015-2022), **Orange book**, 2014.

CHAPTER III: Experimental Methods and Characterisations

3.1. INTRODUCTION

In this chapter, I present the synthesis methods used to prepare the samples studied by Bragg CDI (results and discussion shown in Chapters IV, V and VI) and nanodiffraction (results and discussion shown in Chapter VII). Synthesis preparations and conventional characterisations (UV-Vis, Small Angle X-ray Scattering, Electron Microscopy, X-ray Diffraction) are presented. Details about the performance of these techniques and equipment are shown in Annex.

We work with three sets of different gold nanoparticles referred as seed NP, larger NP synthesised following a seeding-growth method and ultra-small NP stabilised by ionic liquids. We also present the synthesis of two types of titanium dioxides (TiO_2) used as support for the catalysts investigated by X-ray imaging.

The catalytic properties of these materials are evaluated for the CO oxidation reaction, as described hereafter. Finally, gold nanorods (Au NR) studied by nanodiffraction are also presented.

3.2. GOLD NANOPARTICLES

3.2.1. Seed gold nanoparticles

The seed nanoparticles were produced by the citrate reduction protocol (1). 0.5 mL of a 1% (w/v) gold chloride ($\text{HAuCl}_4 \cdot 3\text{H}_2\text{O}$) solution in 50 mL of Milli-Q water was boiled up to 100 °C and then a sodium citrate solution 1% (w/v) was added and the solution was maintained at this temperature for five minutes under vigorous stirring.

Scanning transmission electron microscopy (STEM) images of the gold seed are displayed in Figure 3.1, showing ~ 10 nm sized spherical particles.

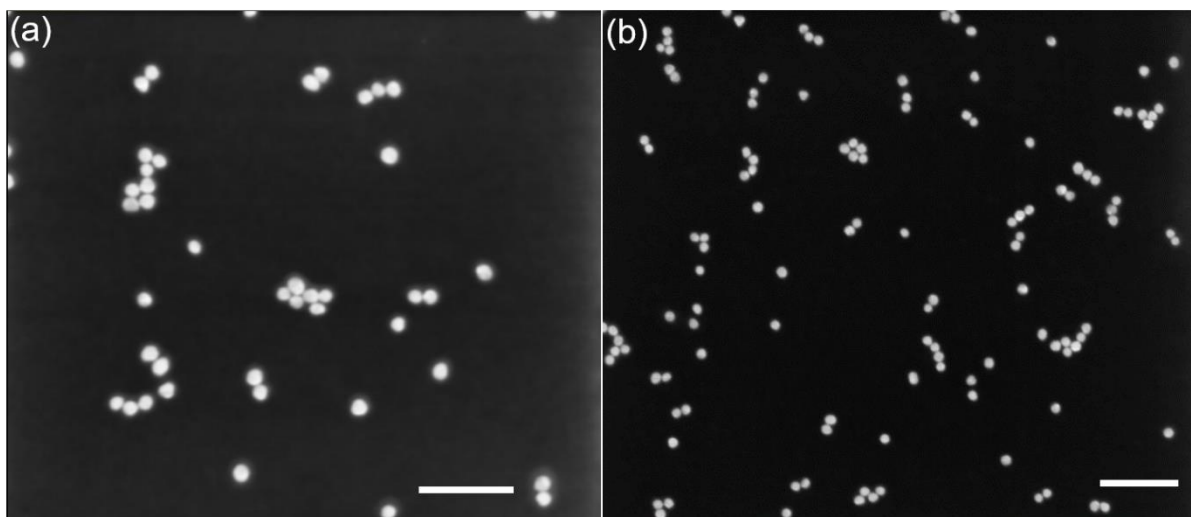


Figure 3.1. STEM images of the seed Au NP at different magnifications (the scale bar is 100 nm).

The size and monodispersity of the gold seeds was checked using small angle X-ray scattering (SAXS) and UV-Vis spectroscopy. Figure 3.2 shows the UV-Vis and SAXS curves of the seed Au NP (black dots) and the fits (red lines). The result of the fit using the sphere model leads to seed nanoparticles with 14 nm diameter and a polydispersity ratio of 0.08. Following the approach proposed by Haiss and co-workers (2) for the calculation of the diameter of Au NP based on the position of the surface plasmon resonance (SPR) band, UV-Vis data lead to the same conclusion. More details about this model and the SPR band are found in the Annex of this manuscript.

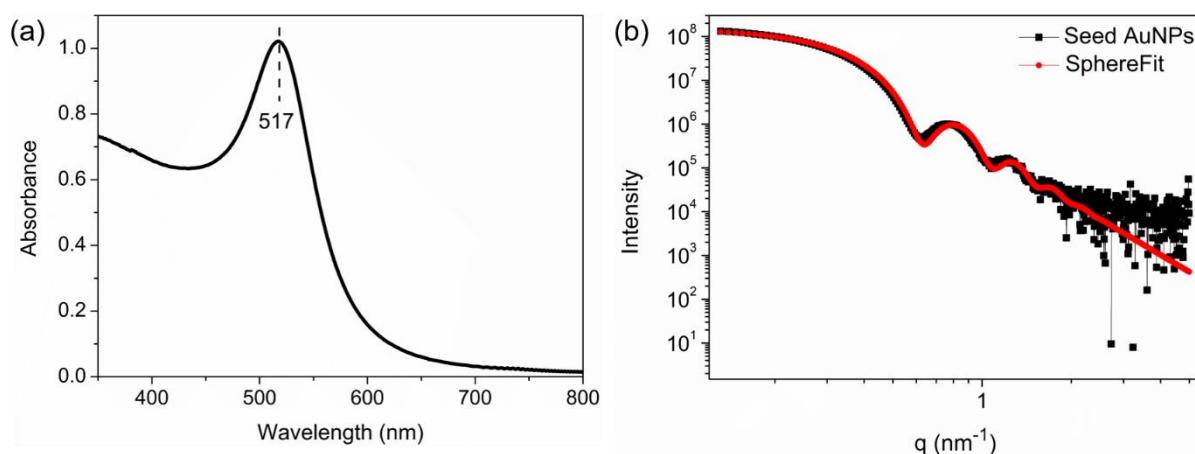


Figure 3.2. (a) UV-Vis spectra of the seed Au NP. (b) SAXS curve of this sample (black) and its respective fit using a sphere model and lognormal distribution.

3.2.2. Large gold nanoparticles

Gold nanocrystals were synthesised following the seeding-growth method (3). The seed Au NP were used for the preparation of two different Au NP sizes: 50 and 120 nm, following a reported work (3). Briefly, 2.25 mL of the seed precursor was mixed with 2.44 mL of a 10 mM gold chloride solution and then 150 mL of Milli-Q water was added to the medium. Finally, 100 mL of an 0.4 mM ascorbic acid solution was added to this system using a peristaltic pump at a controlled rate of 10 mL/min under vigorous stirring. This procedure gives rise to Au NP with an average diameter of 50 nm, referred hereafter as *50_Au*. For the synthesis of 120 nm Au NP, the same procedure was followed, using different volumes of the seed particles and gold chloride (10 mM) solution: 0.24 mL and 2.49 mL, respectively. This sample will be referred hereafter as *120_Au*.

In this method, gold chloride containing Au^{3+} is added to the as synthesised seed nanoparticles and it is reduced on the seed surface by the ascorbic acid at room temperature. The diameter of the larger particles is determined by the size/amount of the seed nanoparticles and by the amount of Au^{3+} added. Figure 3.3 (a) displays the UV-Vis spectra of the *50_Au* sample, showing the SPR band position at 531 nm. Using the equation proposed by Haiss (3) to calculate the particle diameter, the result is 49 nm, in excellent agreement with the expected size for the synthesis protocol used. STEM images recorded for this sample are shown in Figure 3.4 (the scale bar is 25 nm). For both nanoparticles, the size is about 45 nm, in good agreement with the previous results. It is important to notice that the images show isolated particles, but they are representative of the other particles present on the grid used for the microscopy imaging. Figure 3.3 (b) shows the SAXS curve of this sample (in black) and its respective fit (in red). As the form factor of the scattered radiation intensity of this sample is characteristic of spherical particles, a 50 nm diameter sphere model was used in the fitting process. The good agreement between the curve and its fit indicates that the Au NP have these features.

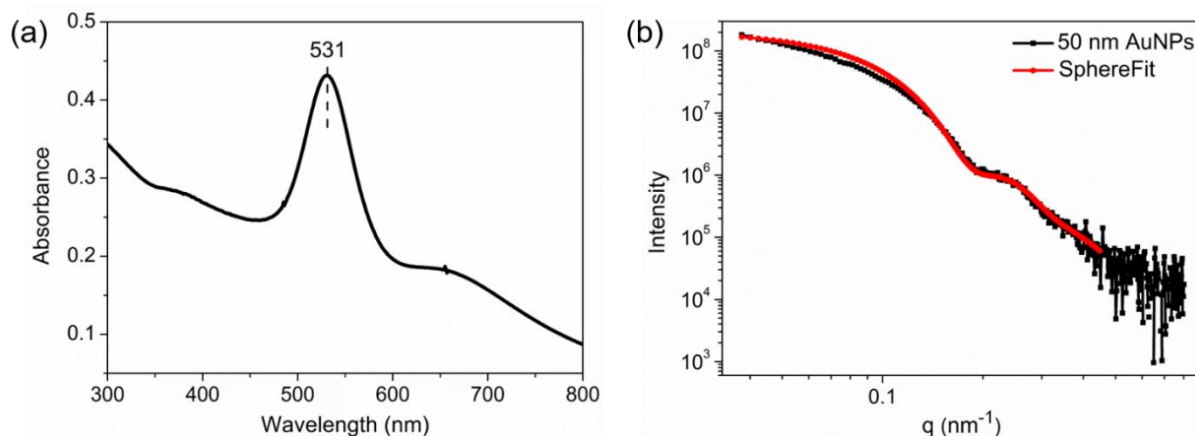


Figure 3.3. (a) UV-Vis spectra and (b) SAXS curve (in black) of the sample *50_Au*. The fit (in red) was done using the sphere model, diameter = 50 nm.

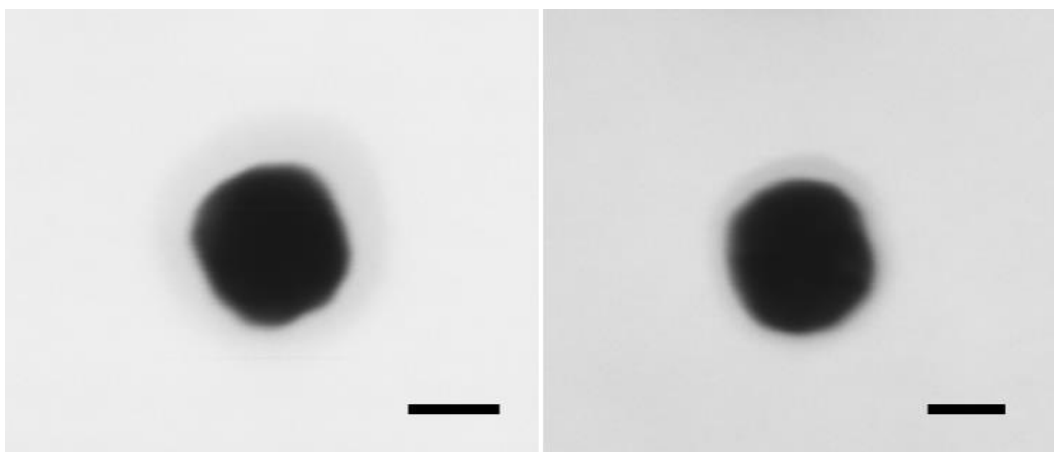


Figure 3.4. STEM images of *50_Au* (scale bar 25 nm).

Figure 3.5 (a) displays the UV-Vis spectra of the sample *120_Au*. The surface plasmon resonance band position is around 600 nm. Using the Haiss (3) approach to calculate the average diameter of the Au NP, the result is 118 nm. This approach is not valid anymore for nanoparticles larger than 110 nm, however, it can be used as an estimation. Figure 3.5 (b) shows the SAXS curve of this sample (in black) and the fit using a 120 nm diameter sphere model (in red). The form factor of the SAXS curve is a characteristic signature of spheres and indicates that the particles are relatively monodispersed. Again, the good agreement between the model and the experimental curve indicates that the nanoparticles have these features.

Figure 3.6 shows STEM images of this sample (the scale bar is 100 nm). The average nanoparticle diameter calculated from SEM images is 118 nm.

The narrow size distribution seen for both Au NP sizes can be explained by the experimental methodology employed in the synthesis: the present seed particles represent the nucleus, so no further nucleation or secondary nucleation processes are expected. Consequently, a narrow size distribution is supposed to be obtained.

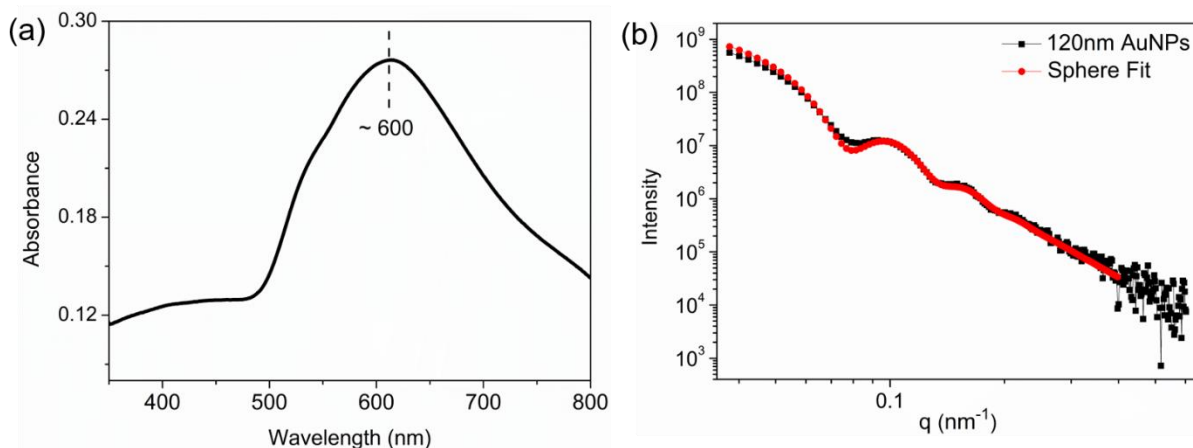


Figure 3.5. (a) UV-Vis spectra and (b) SAXS curve of the sample *120_Au*, synthesised following the seed approach. The sample scattering is shown in black and the fitting using the sphere form factor, in red.

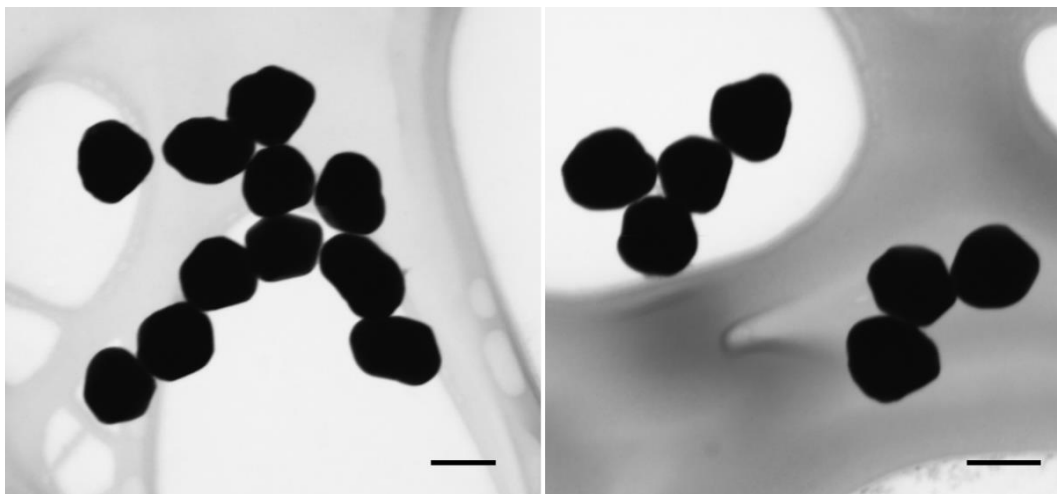


Figure 3.6. STEM images of the sample *120_Au* (scale bar 100 nm).

3.2.3. Ultra-small gold nanoparticles

This paragraph describes nanoparticles in the size range of conventional catalysts, *i.e.*, ultra-small Au NP (a few nm). The synthesis of these gold nanospheres stabilised by ionic liquids was done as follows: 3 mL of ionic liquid (from here denoted by IL) solution (300 mM) was added to 1.5 mL of the gold precursor (from here denoted by Au) solution (6 mM) and stirred for 10 min. Then, 4.5 mL of a freshly prepared NaBH₄ (sodium borohydride) solution (10 mM) was very quickly added to the mixture described above under vigorous stirring to obtain immediately stable gold nanoparticles. The colour of all solutions immediately changed to purple/red (4). Four solutions were prepared varying the IL (1-Dodecyl-3-methylimidazolium chloride/bromide) and the Au salt precursor (gold (III) chloride trihydrate and hydrogen bromoaurate (III) hydrate). The concentration of the IL is 100 mM and the Au salt is 1 mM in the final Au NP solution. The solutions under study were named: NPILX-AuY with X and Y = Cl or Br, which gives rise to the samples: *NPILBrAuBr*, *NPILBrAuCl*, *NPILClAuBr* and *NPILClAuCl*.

Figure 3.7 shows the HRTEM images of these samples (scale bar 20 nm for the four samples), with the respective size distributions (in nm) for each sample.

Figure 3.8 (a) displays the SAXS data for the four gold samples (in black) and their respective fits (in red). For all the samples a sphere model was used. The resulting diameters of the particles are in the range 2.1-2.4 nm and are summarised in Table 1, where the diameter provided by microscopy imaging is summarized as well. In the SAXS curves it is possible to see a scattering pattern in low q regions due to the presence of larger objects. As larger particles of this size were not seen in the electron microscopy imaging (Figure 3.7), we attributed this to aggregation of the NP on the capillary walls during the SAXS measurement.

Table 1. Diameter (in nm) taken from SAXS and HRTEM imaging of the ultra-small Au NP.

Sample	Diameter (nm) from SAXS	Diameter (nm) from HRTEM
NPILBr-AuBr	2.4	2.4
NPILBr-AuCl	2.4	3.0
NPILCl-AuBr	2.3	2.1
NPILCl-AuCl	2.1	3.5

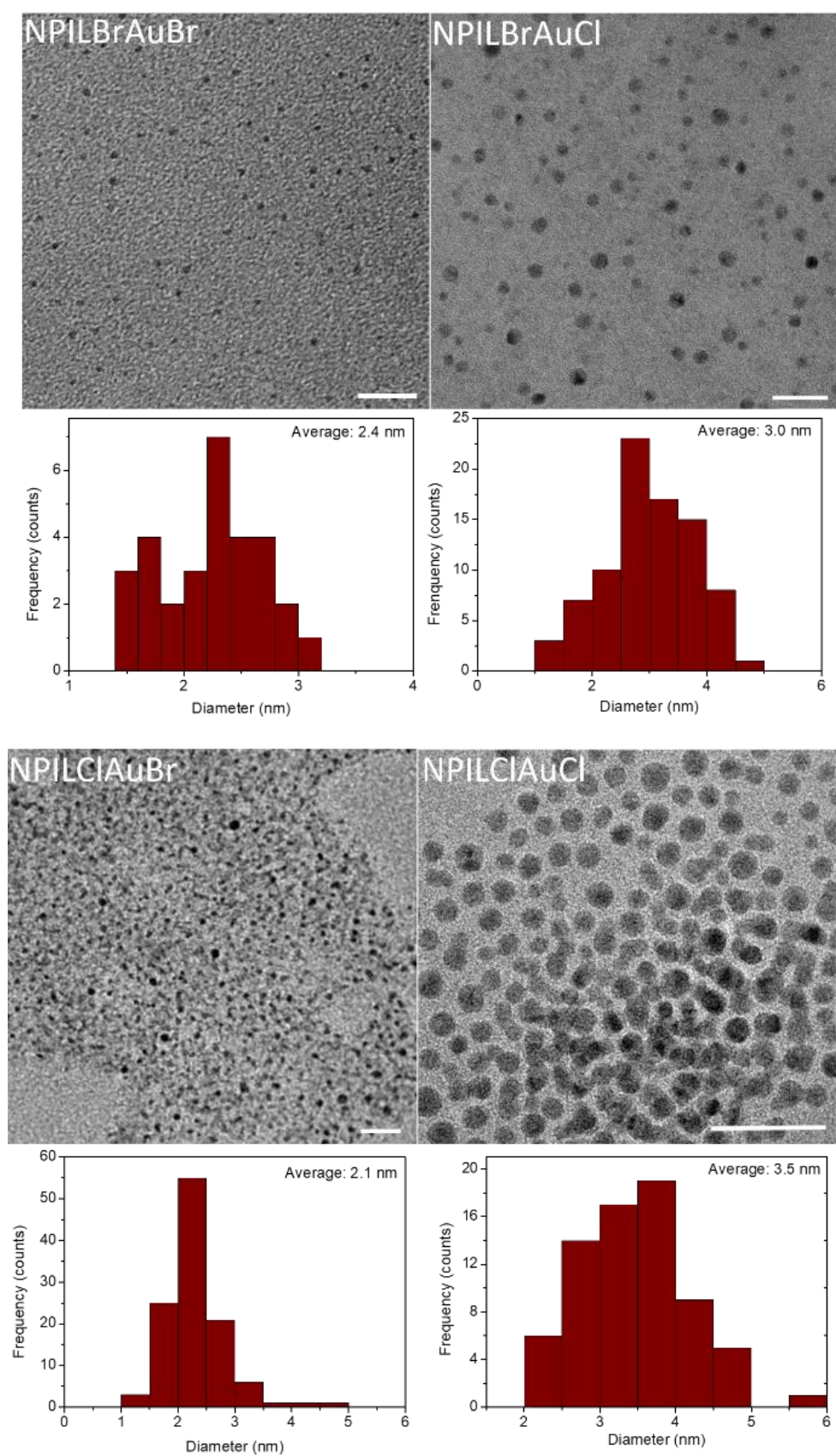


Figure 3.7. HRTEM images of the samples *NPILBrAuBr*, *NPILBrAuCl*, *NPILClAuBr* and *NPILClAuCl* (the scale bar is 20 nm). The diameter distribution below the images is shown as well.

The UV-Vis spectra of these samples are shown in Figure 3.8 (b). The SPR band is in the region 500-515 nm and are largely damped due to the reduced mean free path of the electrons for ultra-small gold nanoparticles (3). The position in lower wavelengths in this range is characteristic of ultra-small Au NP in accordance with the previous SAXS results.

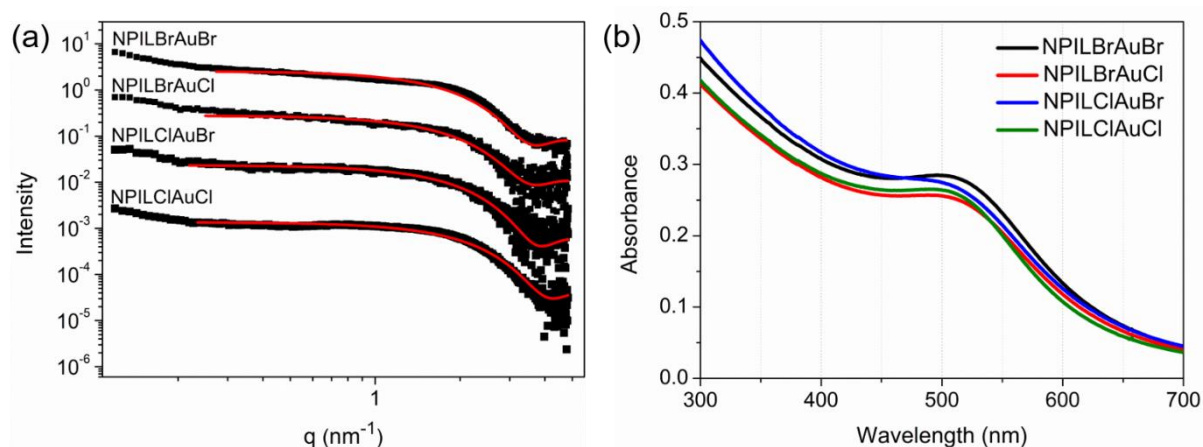


Figure 3.8. (a) SAXS curves and (b) UV-Vis spectra of the samples *NPILBrAuBr*, *NPILBrAuCl*, *NPILClAuBr* and *NPILClAuCl*.

3.3. TITANIA SUPPORTS (TiO_2)

3.3.1. TiO_2 in anatase phase

Anatase titanium dioxide was prepared by a sol-gel method, using titanium isopropoxide as precursor in isopropanol in a reflux system at 70 °C for 4 h. The molar ratio between the titanium precursor and water was 1:100. Right after the synthesis, the sample was centrifugated and washed several times with Milli-Q water and calcined at 450 °C for 16 h. Figure 3.9 (a) shows two microscopy images of this sample at different magnifications. The corresponding XRD pattern is shown in Figure 3.9 (b), where all the peaks were attributed to anatase, indicating a pure TiO_2 anatase phase. This sample is called hereafter *TiO₂-a*.

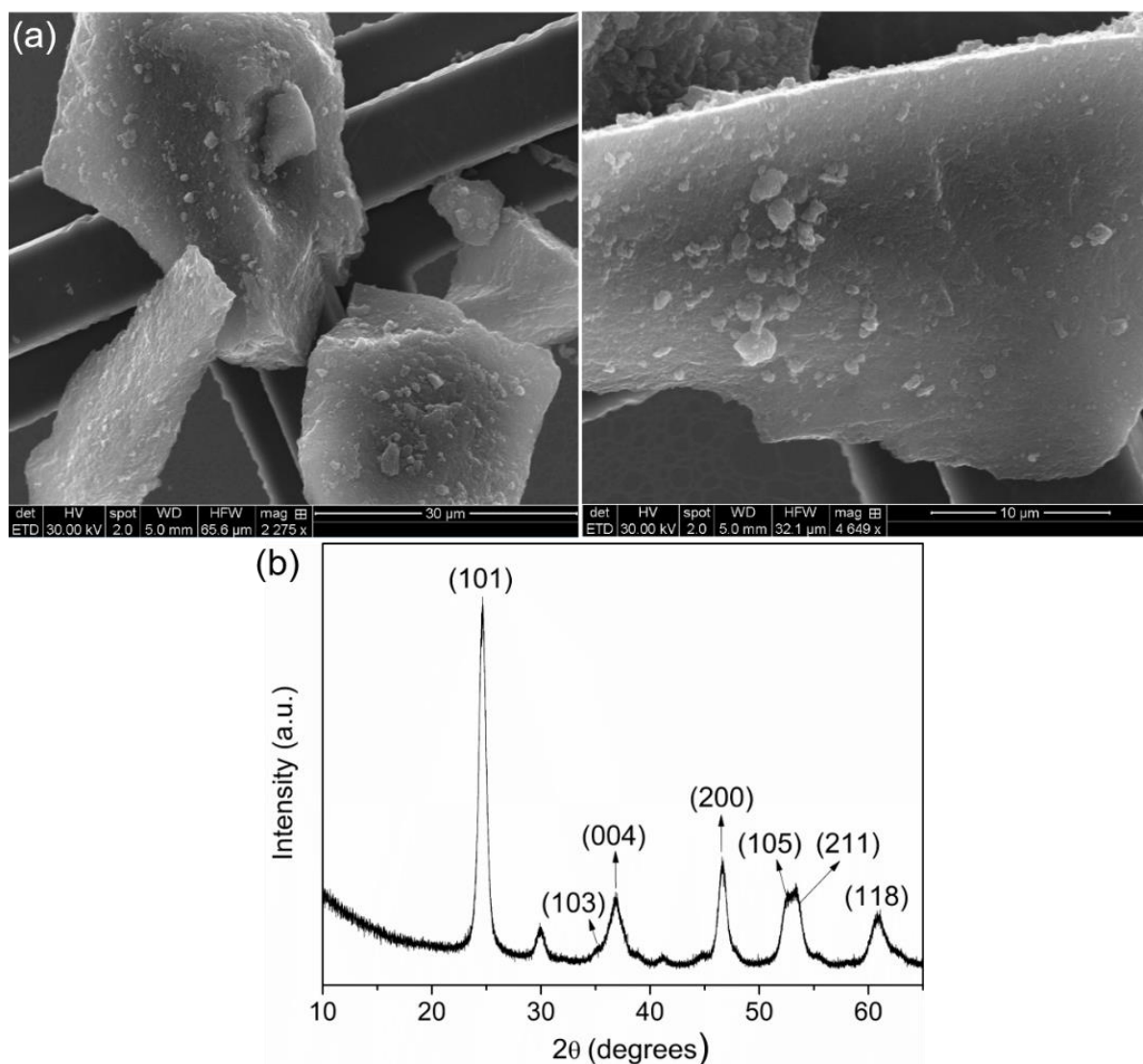


Figure 3.9. (a) SEM images at different magnifications of the sample $\text{TiO}_2\text{-a}$. (b) Diffractogram of this sample.

3.3.2. TiO_2 in mixed anatase and rutile phases

A second type of titania support was prepared via hydrothermal reaction, using the following procedure: 11 mL of TiCl_4 was slowly added to 90 mL of Milli-Q water in a round bottom flask inserted in a container with ice (as the TiCl_4 is extremely toxic and corrosive, this chemical was manipulated very carefully). The flask was then inserted in a reflux system at 160 °C and it was maintained for 16 h. The titania was centrifuged and washed multiple times and it was left in an oven at 110 °C for 15 h and calcined at 450 °C for 16 h. Figure 3.10 (a) shows STEM images of this TiO_2 sample. We observe a partial rod-shaped structure, as highlighted by the red arrows. In Figure 3.10

(b), the XRD pattern of this sample is displayed. Although the synthesis protocol used was directed for obtaining the pure rutile phase, there is a mixture of both phases, anatase (indicated by A) and rutile (indicated by R), as one can see in the attribution of the peaks in the diffractogram. Hereafter, this titania support will be referred as TiO_2 -*m*.

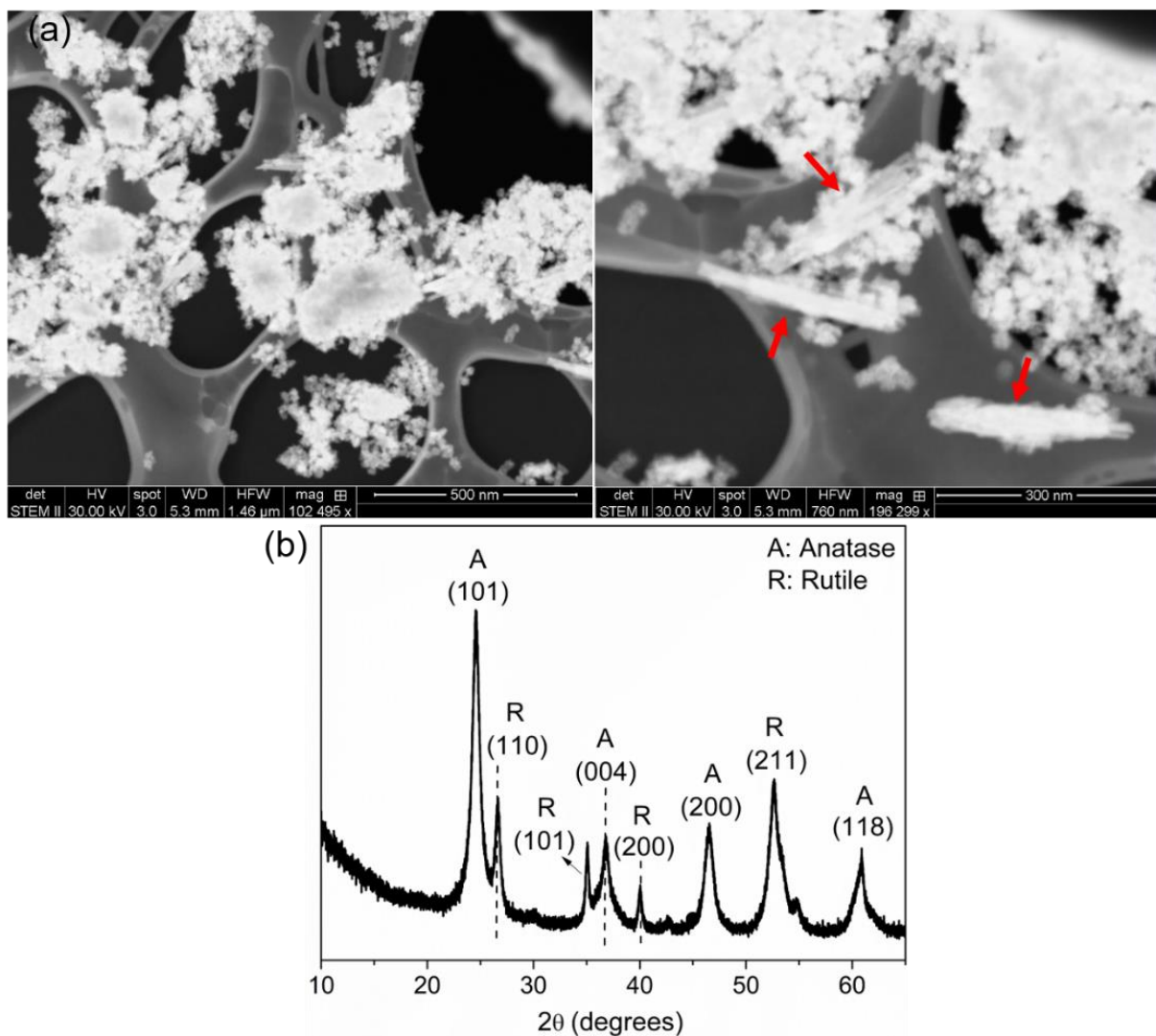


Figure 3.10. (a) SEM images at different magnifications of the sample mixed TiO_2 (anatase/rutile). (b) Diffractogram of this sample, where there is a mixture of both phases, anatase (denoted by A) and rutile (denoted by R).

3.4. SUPPORTED CATALYSTS

3.4.1. Catalysts preparation

The next step is the impregnation of the as synthesised gold nanoparticles *50_NP*, *120_NP* and *NPILClAuCl* on titania supports. For doing so, 50 mL of the Au NP is mixed with 100 mg of the titania powder and acidified by sulphuric acid until a pH = 1 is reached. The theoretical loading of gold is 1 wt%. The mixture is stirred for 2 h at room temperature (RT), centrifugated and washed until the supernatant becomes neutral. Then, the powder is dried at 120 °C for 6 h, calcined at 300 °C for 3 h and treated under a flux of pure H₂ at 400 °C for 1 h.

The STEM images of the five samples: *NPILClAuCl-TiO₂-a*, *50_Au/TiO₂-a*, *50_Au/TiO₂-m*, *120_Au/TiO₂-a*, *120_Au/TiO₂-m* (-a for TiO₂ anatase and -m for the mixed TiO₂) are shown in Figure 3.11, Figure 3.12 and Figure 3.13. It is noticeable that the ultra-small Au NP are rather well dispersed on the titania, as shown by the red arrows in the first image of Figure 3.11. Only a few aggregates were observed as highlighted by the red arrow in the second image, indicating that the nanoparticles coalesced during the impregnation or the calcination procedures. For the larger Au NP, Figure 3.12 and Figure 3.13 clearly show isolated gold nanocrystals deposited on the support, necessary condition for the Bragg CDI measurements.

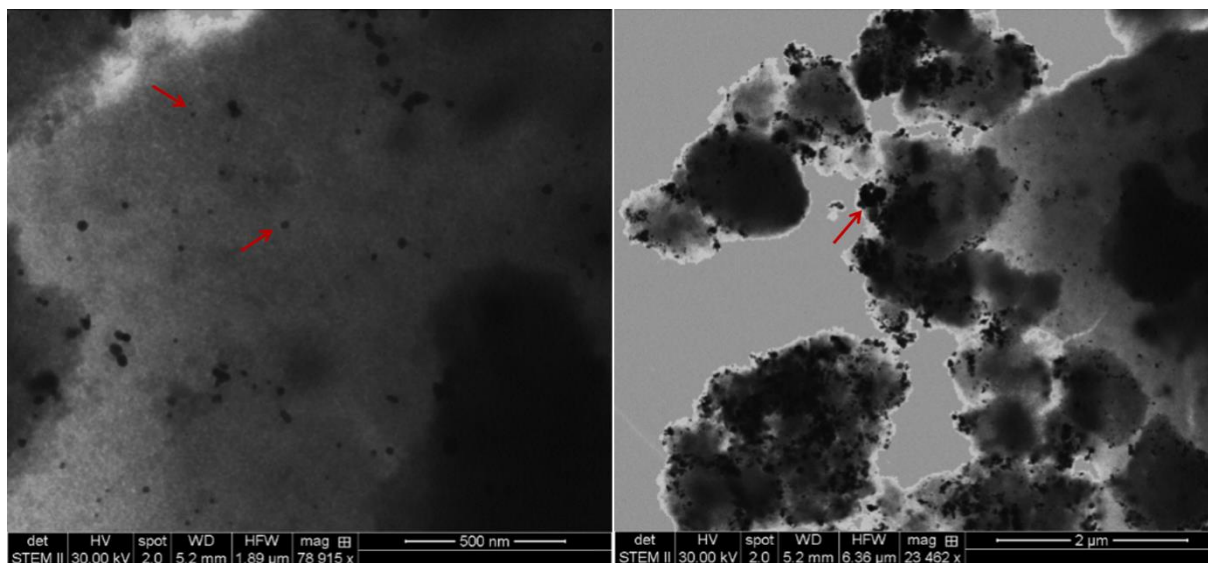


Figure 3.11. STEM images at different magnifications of the sample *NPILClAuCl-TiO₂-a*.

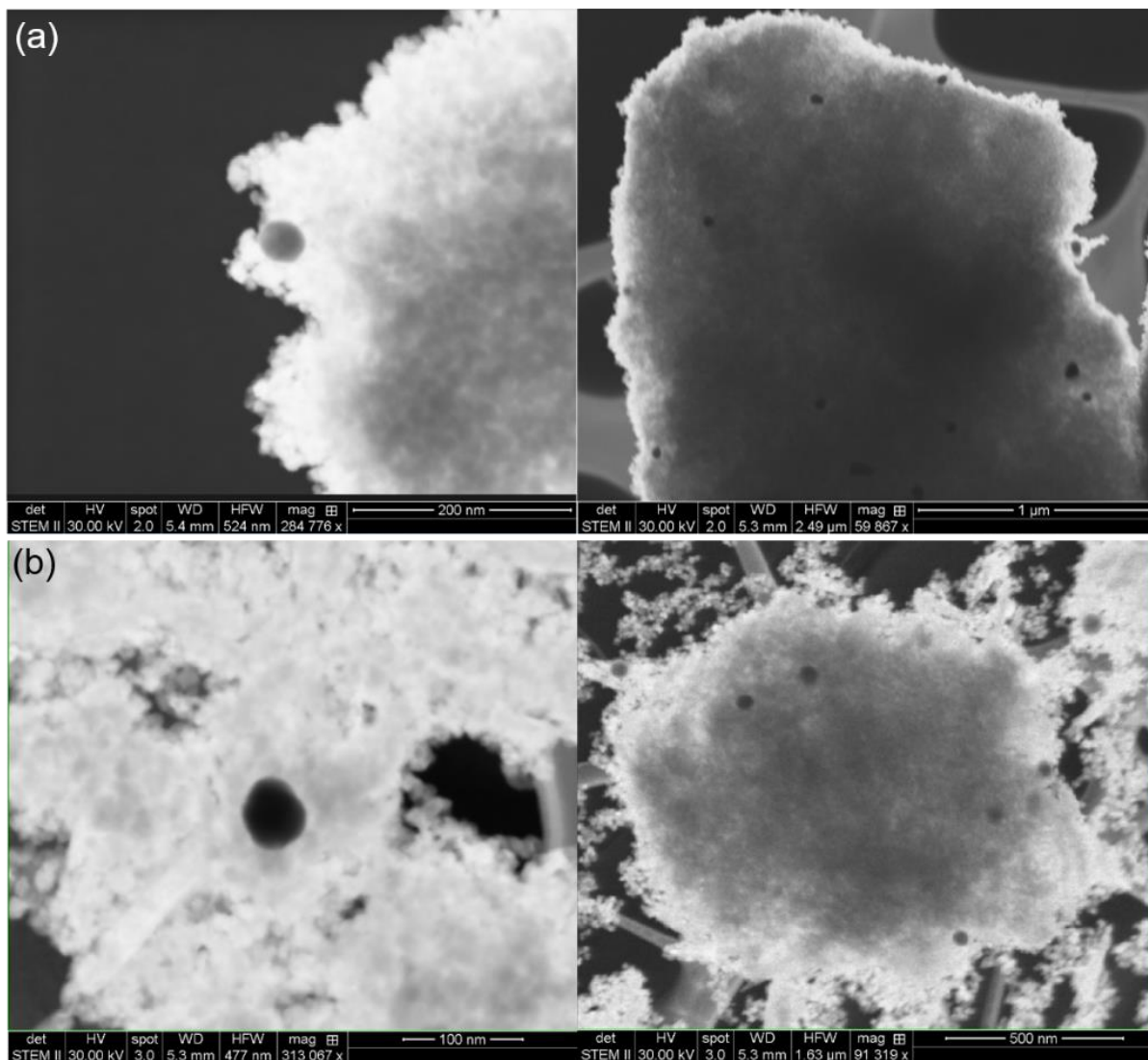


Figure 3.12. STEM images at different magnifications of the samples 50_Au/TiO₂-a (a) and 50_Au/TiO₂-m (b).

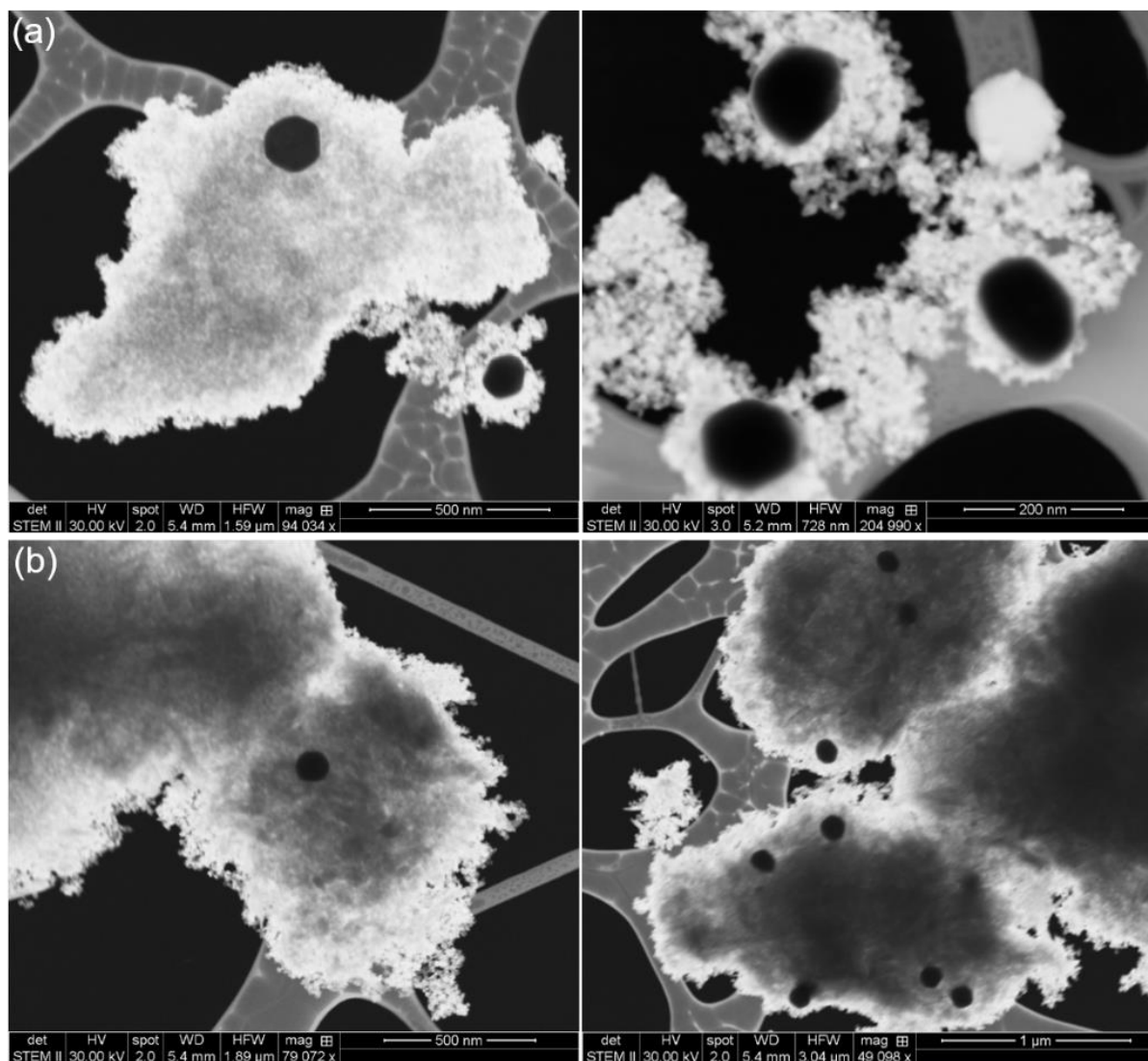


Figure 3.13. STEM images at different magnifications of the samples 120_Au/TiO₂-a (a) and 120_Au/TiO₂-m (b).

3.4.2. Catalytic tests

The catalytic activity of the Au/TiO₂ samples was measured for the CO oxidation reaction. The catalytic tests were done by mixing 50 mg of the catalyst with 250 mg of powdered quartz and this mixture was placed into a 6 mm diameter quartz bed reactor. The reactor was sited in a tubular furnace and a thermocouple was used to accurately measure the temperature inside it. The total gas flow rate was 50 mL/min in a ratio of 2:1:97 CO:O₂:He. 10 °C/min was used as heating and cooling rates. A mass spectrometry equipment was directly connected to the end of the reactor to follow the catalytic performance. The results of one single cycle per sample is shown in Figure 3.14. The dashed lines represent the heating cycle and the solid lines, the cooling step. The consumption of CO (black) and O₂ (red) are shown as well as the production of CO₂ (blue).

It is noteworthy that the MS signal vs. temperature plots from Figure 3.14 show hysteresis in that temperature-increasing and decreasing curves do not coincide. It means that the degree of conversion does not match with increasing and decreasing temperatures. It corresponds to a temperature hysteresis. The hysteresis is more or less pronounced, depending on the catalyst. However, the tendency is the same for all samples: the conversion of CO into CO₂ is higher in the cooling down step (solid lines).

Above the light-off temperature, corresponding to the temperature of ignition of the reaction, the concentration of CO₂ keeps increasing with the temperature up to reach a maximum value. During the cooling down process, the CO conversion is continuously decreased up to RT.

For the ultra-small nanoparticles, the concentration of CO₂ starts to increase around 100 °C and reaches a maximum around 350 °C. Between 350 and 400 °C, the signal of the mass spectrometer is rather stable which signifies we reached the maximum conversion before the highest temperature. For the other larger gold nanoparticles, the reaction starts at much higher temperature (around 300 °C). No maximum conversion is reached before 400 °C for the 50 and 120 nm nanoparticles.

Although these samples are not highly efficient from the catalysis point of view, they show catalytic activity, and will be studied in the next chapters with Bragg CDI.

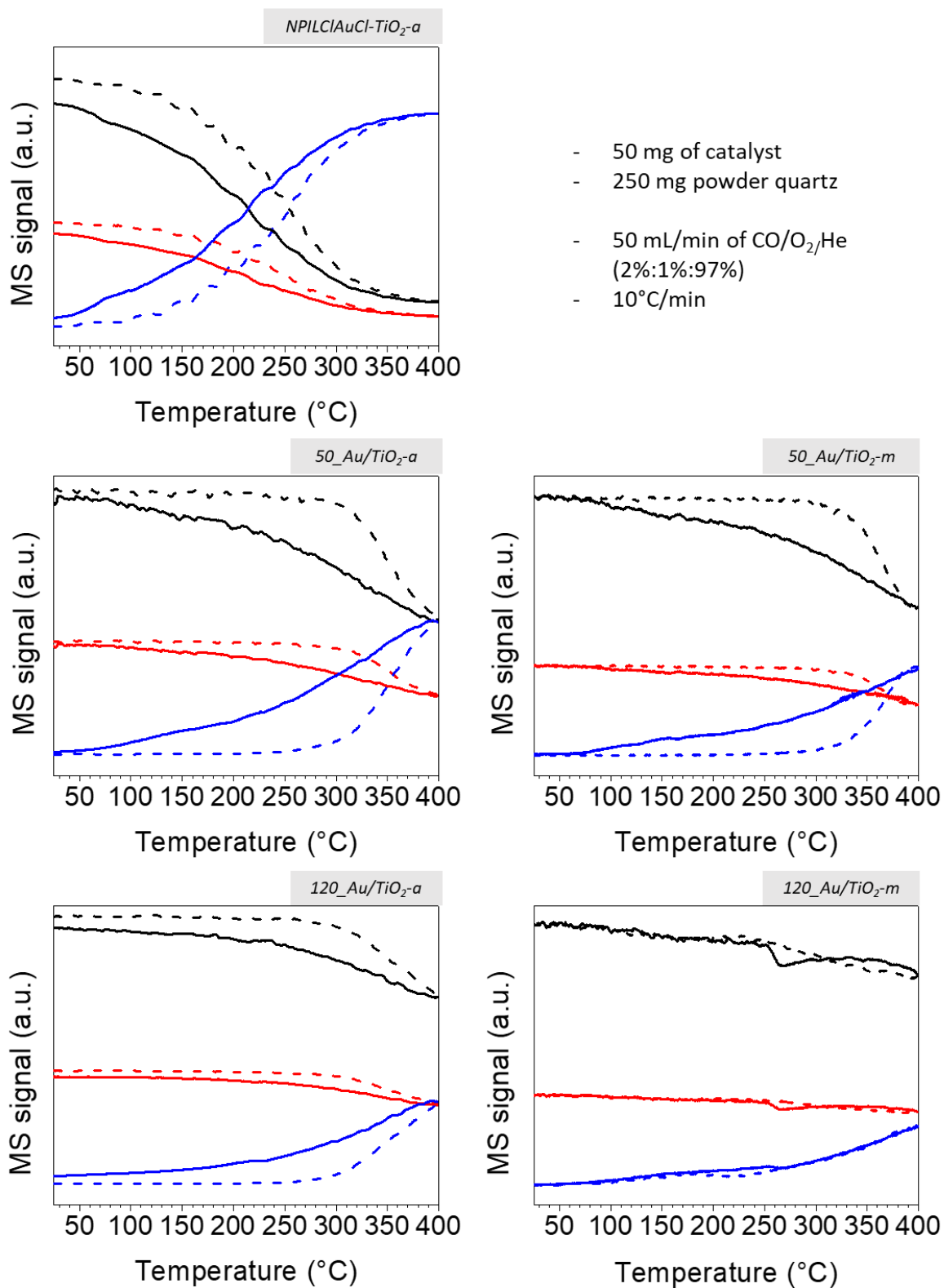


Figure 3.14. Mass spectrometry signal for CO (black), O₂ (red) and CO₂ (blue) obtained for the catalytic tests of *NPILClAuCl-TiO₂-a*, *50_Au/TiO₂-a*, *50_Au/TiO₂-m*, *120_Au/TiO₂-a* and *120_Au/TiO₂-m*. The dashed lines represent the heating and the solid lines, the cooling step.

3.5. GOLD NANORODS (Au NR)

The Au nanorods colloidal dispersion preparation described in this section was done by Dr Patricia Taladriz, University of Fribourg, Switzerland.

Single crystal gold nanorods were synthesised following a previous work with minor modifications (5). At first, a seed solution of nanospheres was produced for subsequently synthesise the Au NR as follows: 5 mL of 0.5 mM HAuCl_4 was mixed with 5 mL CTAB (cetyltrimethylammonium bromide) 0.2 M solution in a 20 mL vial. 0.6 mL of fresh 0.01 M NaBH_4 was diluted to 1 mL with water and was then injected to the Au(III)-CTAB solution under vigorous stirring. The solution colour changed from yellow to brownish yellow and the stirring was stopped after 2 min. The seed solution was aged at room temperature for 30 min.

To prepare the growth solution, 7.19 g (0.038 M in the final growth solution) of CTAB and 1.23 g of sodium oleate (7.4 mM in the final growth solution) were dissolved in 250 mL of warm water ($\sim 50^\circ\text{C}$) in a 1 L Erlenmeyer flask. The solution was cool down to 30°C and 24 mL of 4 mM AgNO_3 solution was added with vigorous stirring for 30 s. The mixture was kept undisturbed at 30°C for 15 min after which 250 mL of 1 mM HAuCl_4 solution was added. The solution became colourless after 90 min of stirring and 5.4 mL of HCl (37 wt. % in water, 12.1 M) was then introduced. After another 15 min of slow stirring, 2.5 mL of 0.064 M ascorbic acid solution was added and the solution was vigorously stirred for 30 s. Finally, 0.8 mL of seed solution was injected into the growth solution. The resultant mixture was stirred for 30 s and left undisturbed at 30°C for 12 h for NR growth.

Figure 3.15 shows the UV-Vis spectra of this sample where there are two distinct resonance bands corresponding to the transverse (at 527 nm) and longitudinal (at 1060 nm) modes derived from the SPR absorption. The inset in the spectra displays a SEM image (scale bar 100 nm) of this sample, where it can be noted certain degree of monodispersity in the distribution of the nanorods. It is also noticeable that there are spheres mixed with the nanorods. The NR are 91.08 ± 10.20 nm in length and 13.16 ± 1.17 nm in width, which gives rise to an aspect ratio of 6.94 ± 0.73 . Figure 3.16 shows the SAXS curve (in black) and the fitting (in red) using the sphere model for low q values and cylinder model for higher q values region, as there are both shapes in the sample as seen by microscopy imaging. Considering that there is a certain degree of polydispersity as can be seen in the SEM images taken before the SAXS

measurement, the model parameters values used for the sphere were 16 nm radius and a polydispersity ratio of 0.3. For the cylinder fit, the averaged length and radius of the nanorods were 90 and 6.6 nm, respectively. The good agreement between the theoretical and experimental curves demonstrate that the parameters values used are adequate.

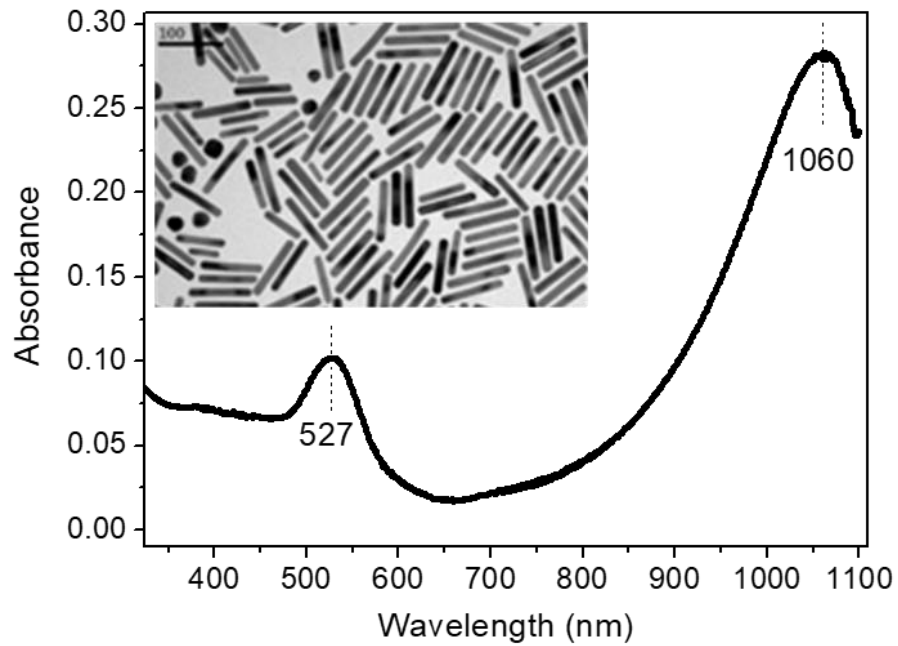


Figure 3.15. UV-Vis spectra of the Au NR, showing two bands corresponding to the transverse (at 527 nm) and longitudinal (at 1060 nm) SPR modes. The inset shows a SEM image.

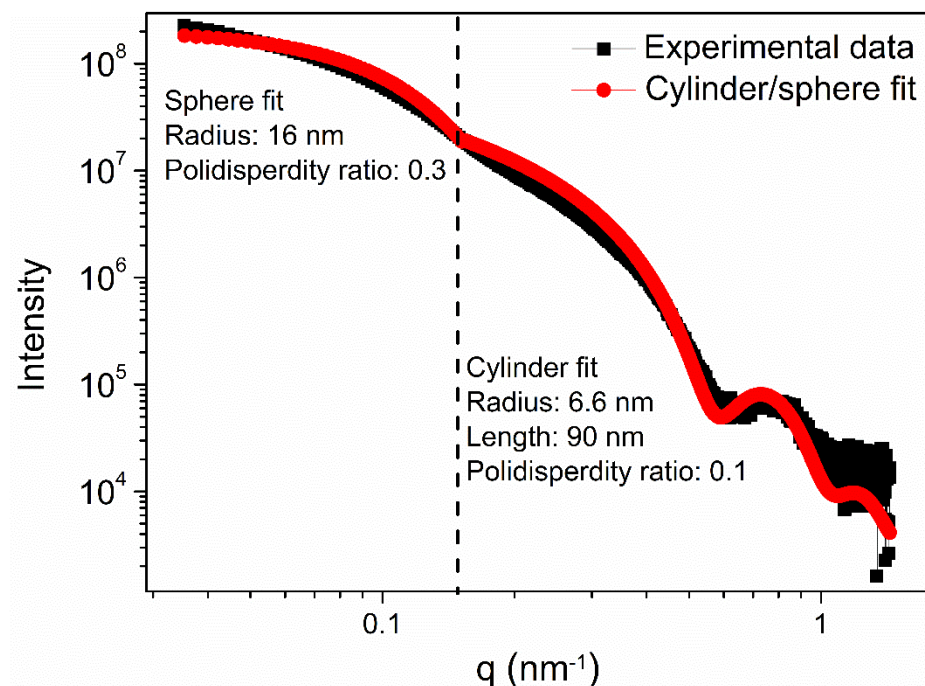


Figure 3.16. Au NR SAXS curve (black) and the cylinder/sphere model fit (red) used to fit the different q regions of the experimental data.

CONCLUSIONS

After the synthesis and characterisation of those gold catalysts, we select the *120_Au/TiO₂-a* and *120_Au/TiO₂-m* for *in situ* Bragg CDI experiments. Even if the 50 nm supported samples present better catalytic performance since more active at lower temperatures, those nanoparticles are too challenging for Bragg CDI experiments. Indeed, the smaller ones would diffract less and would be more difficult to maintain in the proper position during *in situ* treatments as it will be discussed in the next chapter. From the catalytic point of view, the ultra-small nanoparticles are the most relevant however their sizes are of the same order as the resolution achievable today with Bragg CDI, and thus impossible to measure nowadays.

Regarding the Au NR sample, the previous microscopy imaging done before the nanodiffraction was crucial for this experiment. As there is a fluorescence detector at the beamline, we could exactly know which region we were exploring in the membrane, as will be discussed in Chapter VII.

REFERENCES

1. TURKEVICH, J.; STEVENSON, P. C.; HILLIER, J. A study of the nucleation and growth processes in the synthesis of colloidal gold. **Discussions of the Faraday Society**, v. 11, p. 55, 1951.
2. HAISS, W. et al. Determination of Size and Concentration of Gold Nanoparticles from UV–Vis Spectra. **Analytical Chemistry**, v. 79, n. 11, p. 4215–4221, 2007.
3. HUO, S. et al. Superior Penetration and Retention Behavior of 50 nm Gold Nanoparticles in Tumors. **Cancer Research**, v. 73, n. 1, p. 319–330, 2013.
4. LI, T.; SENESI, A. J.; LEE, B. Small Angle X-ray Scattering for Nanoparticle Research. **Chemical Reviews**, v. 116, n. 18, p. 11128–11180, 2016.
5. YE, X. et al. Using Binary Surfactant Mixtures to Simultaneously Improve the Dimensional Tunability and Monodispersity in the Seeded Growth of Gold Nanorods. **Nano Letters**, v. 13, n. 2, p. 765–771, 2013.

CHAPTER IV: Development of an *In situ*
Reactor to Image Catalysts at Work in
Three-Dimensions by Bragg CDI

4.1 INTRODUCTION

In heterogeneous catalysis, reaction conditions can affect not only the selectivity/activity of the reaction but also the catalysts behaviour. That's why, it is crucial to perform *in situ* studies, *i.e.* under controlled gas and temperature environment. To go further, true *operando* studies, *i.e.* under realistic working conditions (temperature, pressure) in combination with a products analysis system, will bring stronger insights for the understanding of the relationship between catalysts structure and activity.

The use of hard X-ray coherent diffraction imaging is compatible with *in situ* characterisation of most of materials. To date, only a few reactors are reported in the literature for *in situ* X-ray imaging of heterogeneous catalysts (1,2). In this chapter, a new *in situ/operando* cell dedicated to high temperature Bragg coherent X-ray diffraction imaging measurements of heterogeneous catalysts has been built. It allows Bragg CDI measurements under controlled flow of various gas mixtures above atmospheric pressure and at elevated temperatures, up to 500 °C. Its design has been chosen to meet both requirements of X-ray imaging: 1/ the beamline geometry (transparent windows and consequently no beam intensity loss; adequate weight as there is a limit for the sample stage and it is a compact system) and 2/ regarding the *in situ* catalytic conditions: homogeneous and well controlled temperature in the heater, small volume with limited dead volume, proper connections for the gas inlet/outlet.

4.2. DESIGN AND OPERATION OF THE *IN SITU* REACTOR

4.2.1. Description of the reactor

We developed an *in situ* reactor for Bragg coherent X-ray diffraction imaging measurements under high temperature and gas flow. The cell is designed for measurements in diffraction mode, as recently published (3). As shown in Figure 4.1, the reactor is composed of a silicon nitride heating device (BACH-RC GmbH) enabling to control the temperature up to 500 °C. Higher temperatures can be reached by replacing the ceramic heating device.

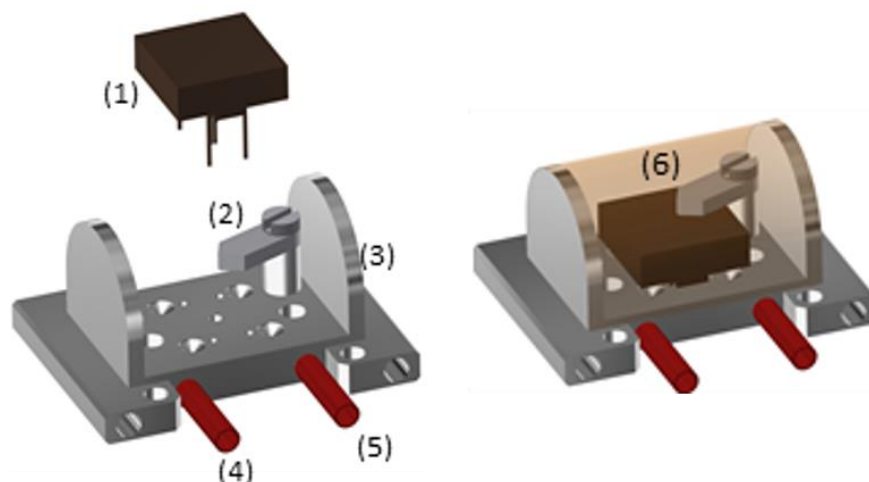


Figure 4.1. Schematic overview of the cell. (1) ceramic heating device, (2) clamp, (3) cell body, (4) gas inlet, (5) gas outlet, (6) Kapton window.

A Pt100 resistance thermometer is used for PID (proportional integral derivative) temperature regulation. A Kapton window is glued on the upper part of the cell and enables to work under controlled gas mixture at atmospheric pressure. The window allows X-rays to enter and exit the cell without significant reduction in intensity. Its dome geometry gives the necessary flexibility in terms of sample alignment and range of angles ($\sim 180^\circ$), indispensable to work in diffraction mode with various materials. Two inlet and outlet tubes (1/8 inch) enable the gas flow.

For the CDI measurements, the sample is deposited on a chemically inert sample holder usually used in electron microscopy, which allows to characterise the samples by electron microscopy methods before and after the X-ray imaging measurements. For the Bragg CDI measurement, the sample holder is clamped (item 2 in Figure 4.1) on the ceramic heating device.

The whole setup is purposely very compact ($40 \times 30 \times 20 \text{ mm}^3$) and light, with a weight below 100 g, compatible with piezo stages commonly used at X-ray imaging beamlines. Even if rather compact, the volume of gas around the sample is still rather big from the catalysis point of view. Indeed, the volume of gas around the sample is mainly constrained by the height of the window. This one cannot be lower to avoid to be burned at too high temperatures. To go further, smaller reactor volume, without dead volume, would improve the *in situ/operando* catalyst characterisation.

4.2.2. Validation of the reactor

At first, we checked the homogeneity of the temperature provided by the ceramic heating device on the sample holder. The temperature of a silicon wafer, used as sample holder, was determined by Infrared (IR) thermography with an ImageIR® 8300 HP camera from InfraTec (InfraTec GmbH, Dresden, Germany) equipped with a microscopic lens with a magnification of 1.0, a working distance of 20 cm, a field of view of 9.6×7.7 mm and a pixel size of $15 \mu\text{m}$. An IR thermography image is presented in Figure 4.2, showing the temperature of the silicon wafer and its surrounded heater (in part). Figure 4.2 puts in evidence the narrow temperature distribution (± 1 °C) at 400 °C of the silicon wafer where the sample is deposited for CDI measurements. We can also see the homogeneity of the temperature on the heating device around the sample holder.

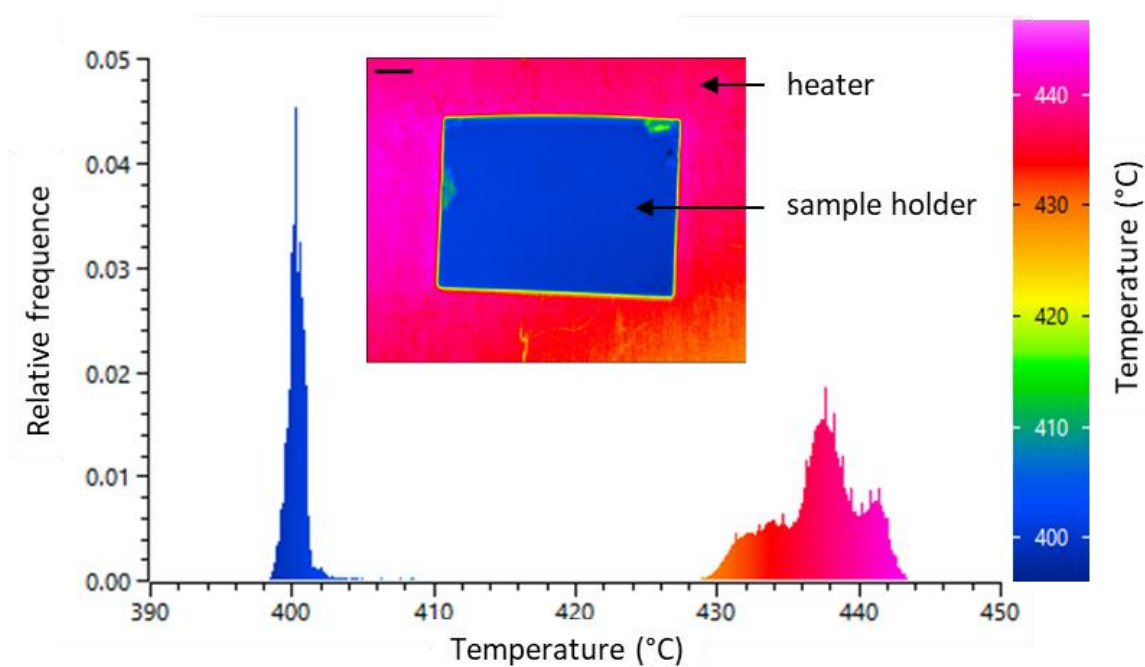


Figure 4.2. Infrared thermography measurement of the sample holder heated at 400 °C: IR thermography image and temperature distribution on the whole image. Scale bar corresponds to 1 mm.

In order to follow the catalytic performances of the sample loaded into the reactor, an on-line mass spectrometer (Pfeiffer vacuum Prisma) was connected to the gas outlet. We measured the conversion of CO of our model catalyst. This latter is composed of gold nanoparticles supported on TiO_2 with a diameter size around 120

nm, as observed by scanning transmission electron microscopy (Chapter III). Despite the small amount of sample loaded into the holder, it is possible to follow its catalytic properties by measuring the conversion of CO into CO₂. As shown in Figure 4.3, we can clearly see the onset of CO oxidation with the consumption of CO and O₂ and the production of CO₂ during heating up (1.0% CO – 0.5% O₂). We can also observe the decrease of CO conversion during the cooling ramp. The CO oxidation is unambiguously assigned to the catalytic activity of the gold nanoparticles, because for an unloaded cell the gas composition remained constant. This validates the use of the cell for catalytic measurements during X-ray imaging studies.

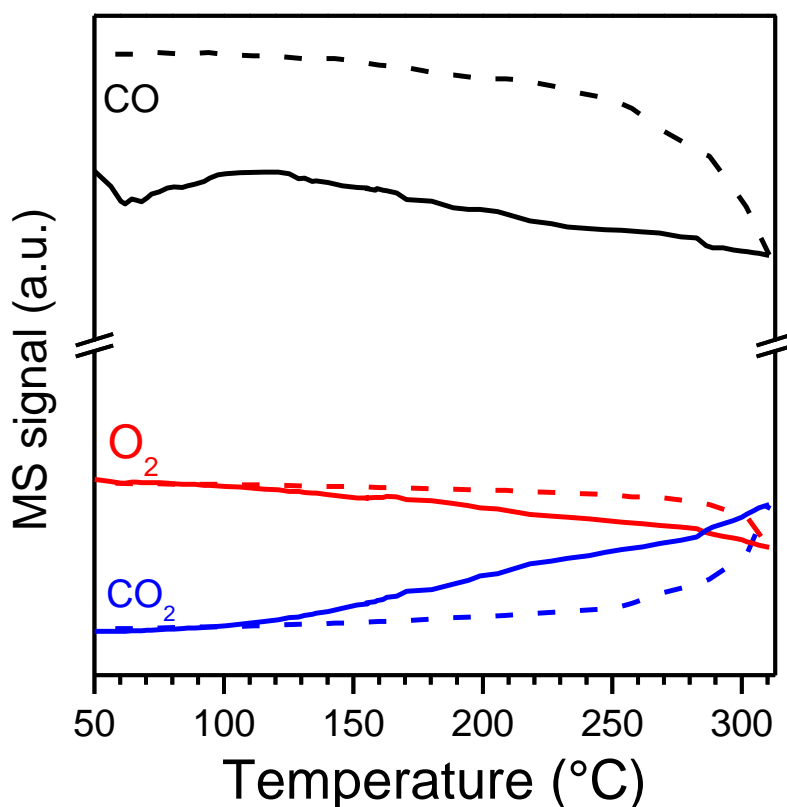


Figure 4.3. Mass spectrometry signal of CO (black), O₂ (red) and CO₂ (blue) obtained at the outlet of the cell during heating-cooling reaction cycle (1% CO, 0.5% O₂). Heating: dashed line and cooling: solid line.

4.3. FIRST BRAGG CDI MEASUREMENTS OF Au NP WITH THE *IN SITU* REACTOR

4.3.1. Cristal beamline at SOLEIL

Bragg CDI measurements were carried out at the synchrotron radiation facility SOLEIL (Saint-Aubin, France) at the Cristal beamline, which is dedicated for performing diffraction techniques. Cristal is an undulator beamline as schematised in Figure 4.4. Figure 4.5 displays a photo of the beamline showing the position of the sample, the detector, the goniometer and the θ -2 θ configuration.

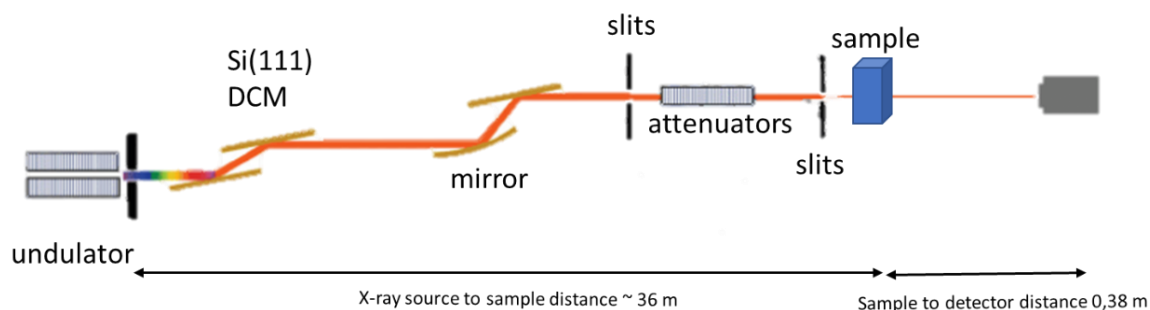


Figure 4.4. Schematic of the Cristal beamline. Figure adapted from (4).

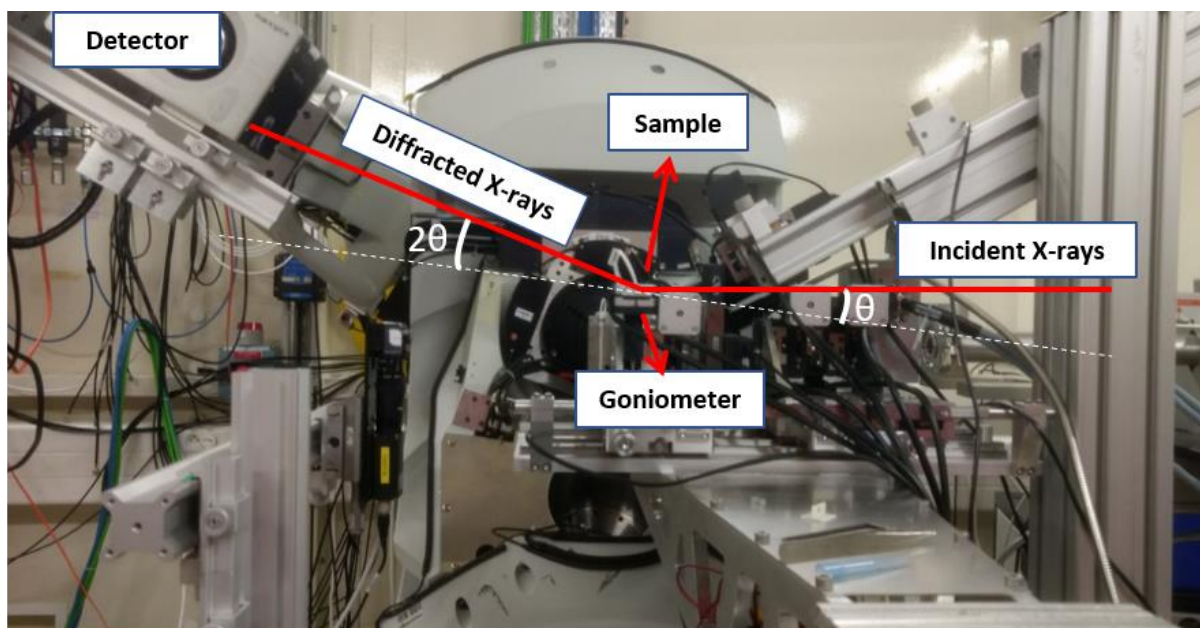


Figure 4.5. Experimental set-up of Cristal beamline showing the θ -2 θ configuration for the Bragg CDI experiment.

At Cristal beamline, the goniometer is used for the rocking curve measurement as a scan in the θ angle and it consists of a piezo stage controlled by motors motion. Figure 4.6 shows the cell loaded with the sample and installed on the sample stage of the Cristal beamline. For the Bragg CDI experiment, an 8.5 keV X-rays beam was used and focused into a $2 \times 2 \mu\text{m}^2$ (FWHM) spot, with a Fresnel zone plate (FZP, diameter = 294 μm ; outermost zone width = 100 nm; focal length = 20 cm) and an order sorting aperture (diameter = 70 μm) located 15 cm after the FZP. The sample was placed in the focused X-ray beam and appropriately aligned for satisfying the Bragg condition. A Maxipix detector (55 microns pixel size, 512 x 512 pixels) was placed at 0.38 m from the sample recording the scattered X-rays from the gold nanocrystal satisfying the (111) Bragg condition (theoretical Bragg angle equals to 36.11° at 8.5 keV).

For each sample, we measured a rocking-curve of 1.4 - 1.6° by rotating the sample around the Bragg angle with a step of 0.02° . Each angle is exposed during 10 s and a full two dimensions (2D) data set is obtained in around 30 min.

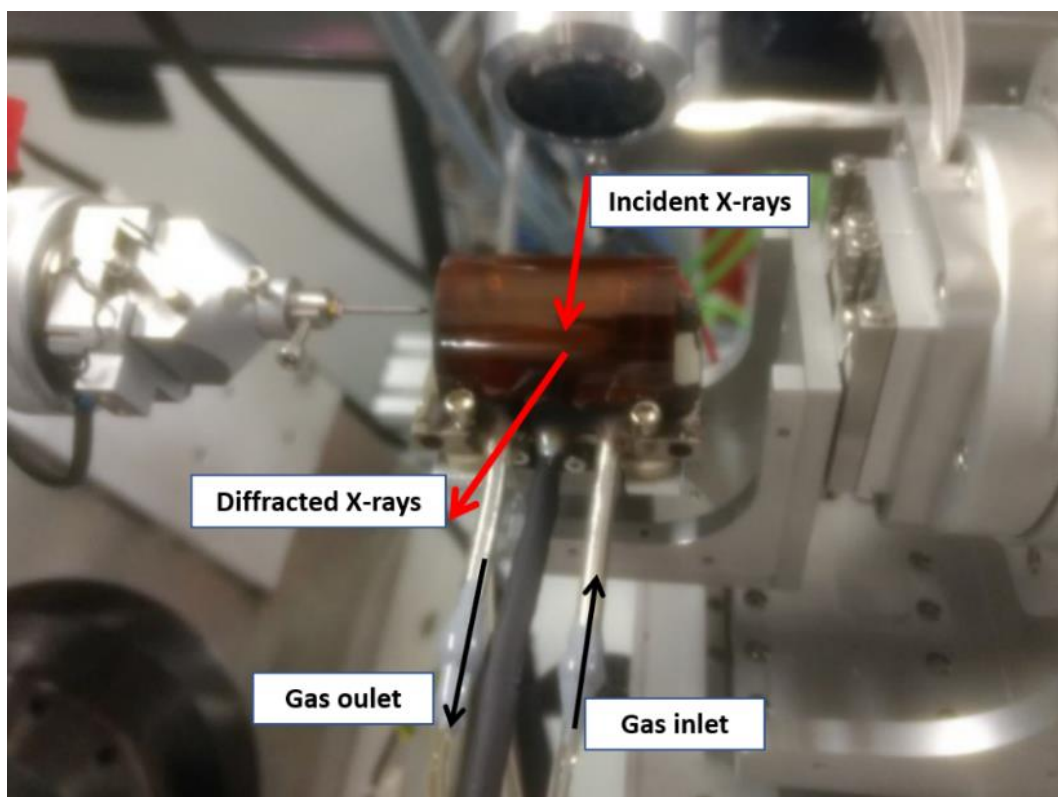


Figure 4.6. Photography of the cell installed at the Cristal beamline at SOLEIL.

4.3.2. Data reconstructions

The data set is inverted using phase retrieval algorithms (5) on *MATLAB R2017b* to produce a real space image of the measured gold nanocrystal. The phasing algorithm involved iterative switching between real and Fourier spaces through the use of fast Fourier transform until known constraints in each domain had been satisfied. 10220 iterations were run for the images presented hereafter. The iterations consist of alternating 20 iterations of the error reduction (ER) algorithm (6) with 180 iterations of the hybrid-input-output (HIO) algorithm (7) while utilising the Shrinkwrap (8) and guided (9) algorithms. The obtained real space images presented herein have a spatial resolution of around 32 nm with a pixel size around 5 nm. The software *ParaView* was used to generate the three-dimensional images of the reconstructed nanocrystals.

4.3.3. *In situ* conditions

Sequences of Bragg CDI diffraction patterns of the gold catalyst (*120_Au/TiO₂-m* from Chapter III) were collected under constant gas flow at two isothermal conditions: room temperature (RT) and 400 °C upon exposure to different gas mixtures: pure He (~40 mL/min) or 0.3% CO – 3.8% O₂ in He with a constant total gas flow (~50 mL/min).

Three experimental conditions referred as *A*, *B* and *C* are presented and discussed hereafter. The condition *A* is representative of the sample at RT under He, *B* is the same nanoparticle observed at RT under the reaction gas mixture and *C* is another nanoparticle observed at 400 °C during the conversion of CO into CO₂. The rocking curves obtained in reciprocal space, used for reconstructions, are presented in Figure 4.7, Figure 4.8 and Figure 4.9, for the three conditions *A*, *B* and *C*, respectively.

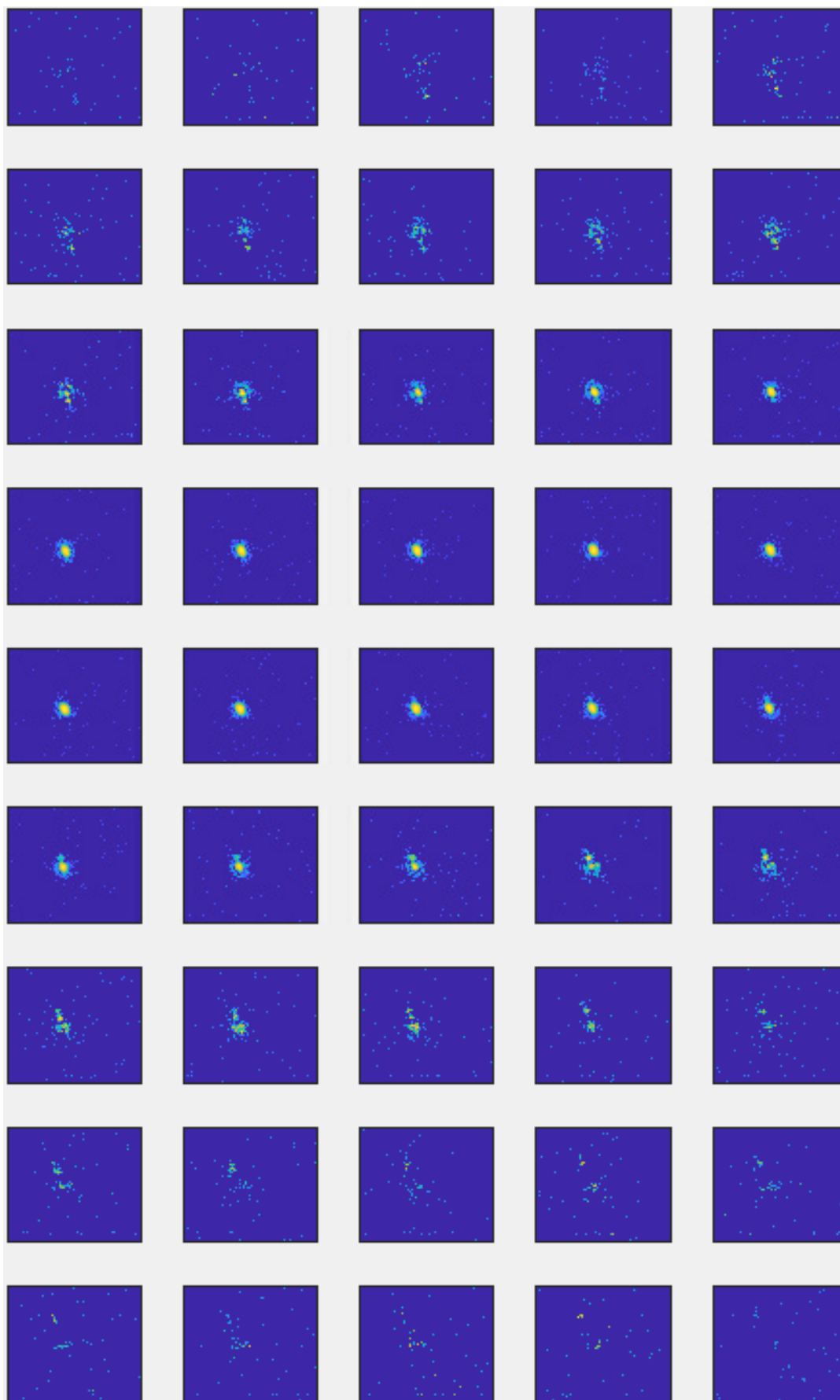


Figure 4.7. Part of the X-ray diffraction data measured during the rocking curve around the Au (111) reflection for one Au/TiO₂ nanoparticle at RT under He (A).

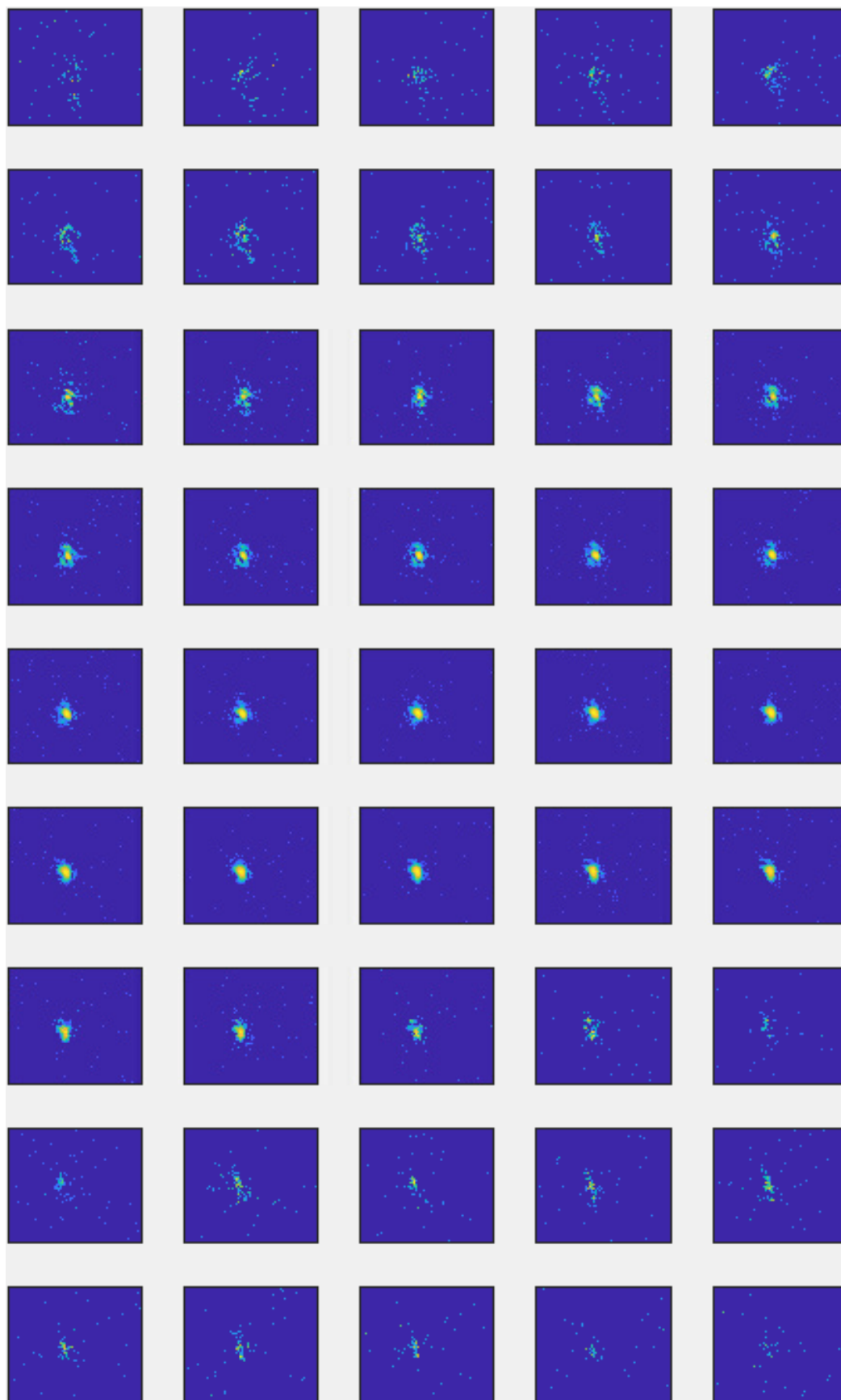


Figure 4.8. Part of the X-ray diffraction data measured during the rocking curve around the Au (111) reflection for one Au/TiO₂ nanoparticle at RT under CO/O₂ (B).

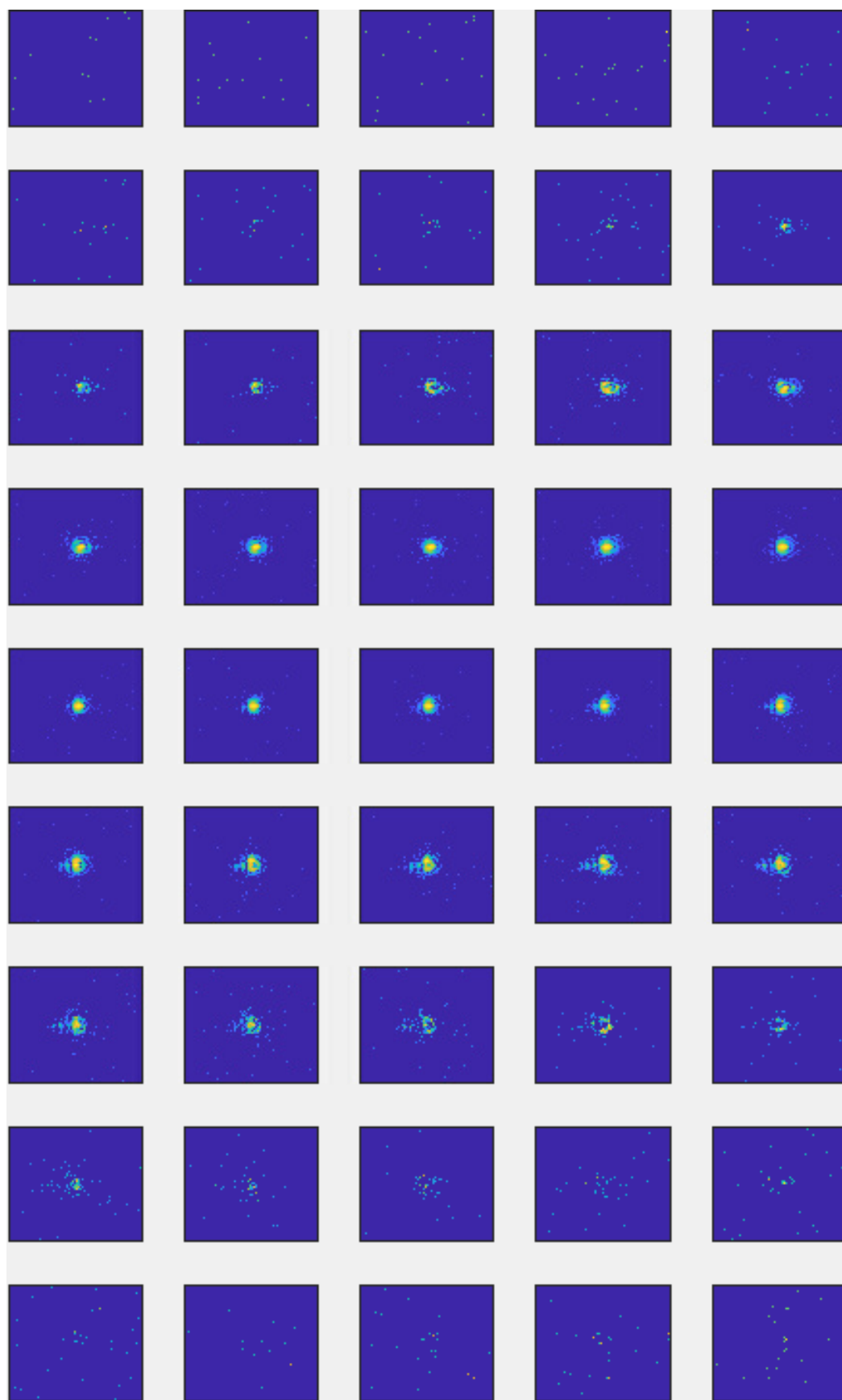


Figure 4.9. Part of the X-ray diffraction data measured during the rocking curve around the Au (111) reflection for one Au/TiO₂ nanoparticle at 400 °C under CO/O₂ (C).

4.4. BRAGG CDI RESULTS AND DISCUSSION

In Figure 4.10 are presented 2D slices through the 3D coherent diffraction patterns around the center of the Bragg spot Au(111) for the same individual Au/TiO₂ nanoparticle at RT under a flux of He (A) and CO/O₂/He (0.3%/3,8%/95,9%) flux (B) at atmospheric pressure. The differences in intensities observed on the diffraction patterns A and B come from the gas changes between both images. After adding the reactive gas mixture, a more distorted diffraction pattern appears showing the changes in the structure, phase and strain distributions inside the nanoparticle due to the gas adsorption. It is noteworthy that those changes are not due to beam damage since a such change has not been observed under static conditions (He at RT) with consecutive rocking curves measurements.

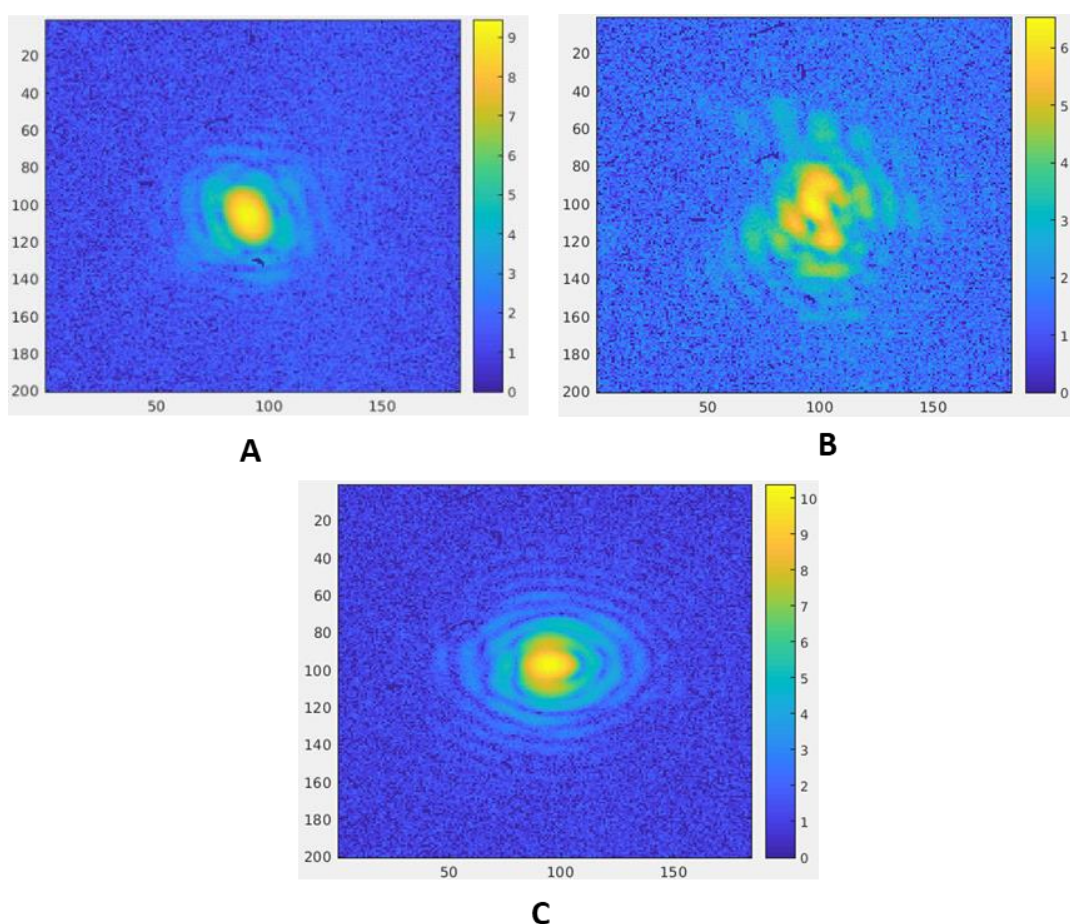


Figure 4.10. 2D slices through the 3D coherent diffraction patterns around the center of the Bragg spot for the same individual Au/TiO₂ nanoparticle at RT under He flux (A) and under CO/O₂/He flux (B). (C) 2D slice for another Au/TiO₂ nanoparticle obtained at 400 °C under CO/O₂/He flux whilst the CO oxidation reaction is occurring.

Whilst the reaction is occurring at 400 °C, we could observe a very different coherent diffraction pattern as presented in Figure 4.10 (C). It is coming from another particle, different from the one presented on **A/B**, since during heating, the signal of the first nanoparticle has been lost. Interestingly a much more symmetric pattern is observed while the reaction is occurring. This is characteristic of structural changes due to the occurrence of the catalytic reaction.

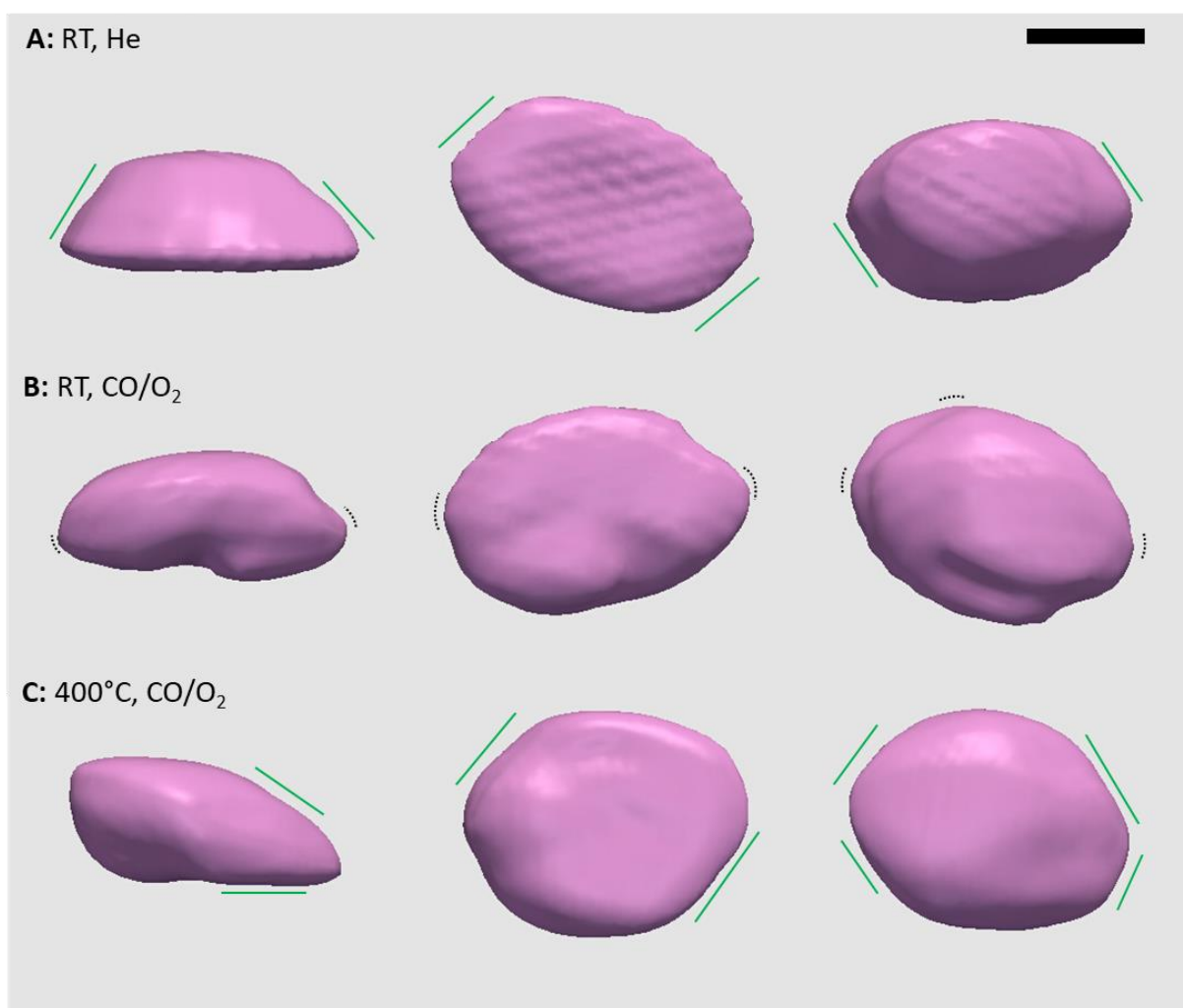


Figure 4.11. Morphology of the gold nanoparticle reconstructed from Bragg CDI patterns measured under He at RT (A), under CO/O₂/He at RT (B) and at 400 °C (C). The side (left), bottom (middle) and top (right) views are presented. The green and black marks are showing the faceted and rounder shapes of the nanoparticles. Scale bar corresponds to 100 nm.

The 2D set of coherent diffraction patterns were phase retrieved and inverted to obtain complex images of the Bragg electron density and lattice displacement of the studied object. Three-dimensional reconstructions of the magnitude of the

nanocrystal's complex density function are presented in Figure 4.11 for the three states on different side views. The density function is shown as 25% of density isosurface. The reconstruction of the gold nanocrystal corresponds reasonably with the dimensions obtained from electron microscopy images, although slightly larger, which could be within the error of the reconstruction size measurements. The pristine object, (A), presents edges and corners as expected from the observations made by electron microscopy. At room temperature, the shape changes from a faceted one under He to a smoother rounded shape under CO/O₂/He as observed in Figure 4.11 A and B. This is in agreement with previous studies of environmental transmission electron microscopy showing that Au catalysts systematically changed the shape with the change of gases (10–12).

During the catalytic reaction at high temperature, the nanoparticle presents a more faceted shape with sharper corners as observed in Figure 4.11 (C). With higher conversion, a refacetting of the gold nanoparticles is observed. This surface restructuring is driven by the minimization of atomic stress and free energy simultaneously in the catalyst particle, support and interface (13).

The phase, used to color the isosurface of the cross-sections in Figure 4.12, shows the internal variation of the lattice distortion from the ideal crystal lattice along (111). The phase range on the Figure is from $-\pi/3$ to $+\pi/4$. A phase redistribution between the three studied states is observed. Adding the reactive gas mixture induces a lattice displacement resulting in a stronger phase structure in the image. As expected, bonding of CO or O₂ molecules to Au nanoparticles is accompanied by weakening of Au-Au bonds (14). The phase shift is broader from the states A to B to C. It corresponds to a more complex lattice displacement structure in the presence of CO/O₂ mixture. Furthermore, a stronger lattice displacement is induced by the reaction process. The highest values of the phase shift are at the external part of the nanoparticles, mainly where the facets meet as compared with those of the flat facets. At the pixel locations with the highest values on the slices, the displacement is of 0.20 Å at RT under He, 0.45 Å under CO/O₂ and 0.66 Å at 400 °C during the reaction. The surface sites and facets on which the reaction occurs are sensitive of the atomic arrangements. That is why stronger lattice displacements are observed at the corners and edges of the nanoparticles. This is in agreement with theoretical work showing that

low-coordinated and perimeter sites are very active and the weakening of Au-Au bond is an essential aspect of the Au activity (14).

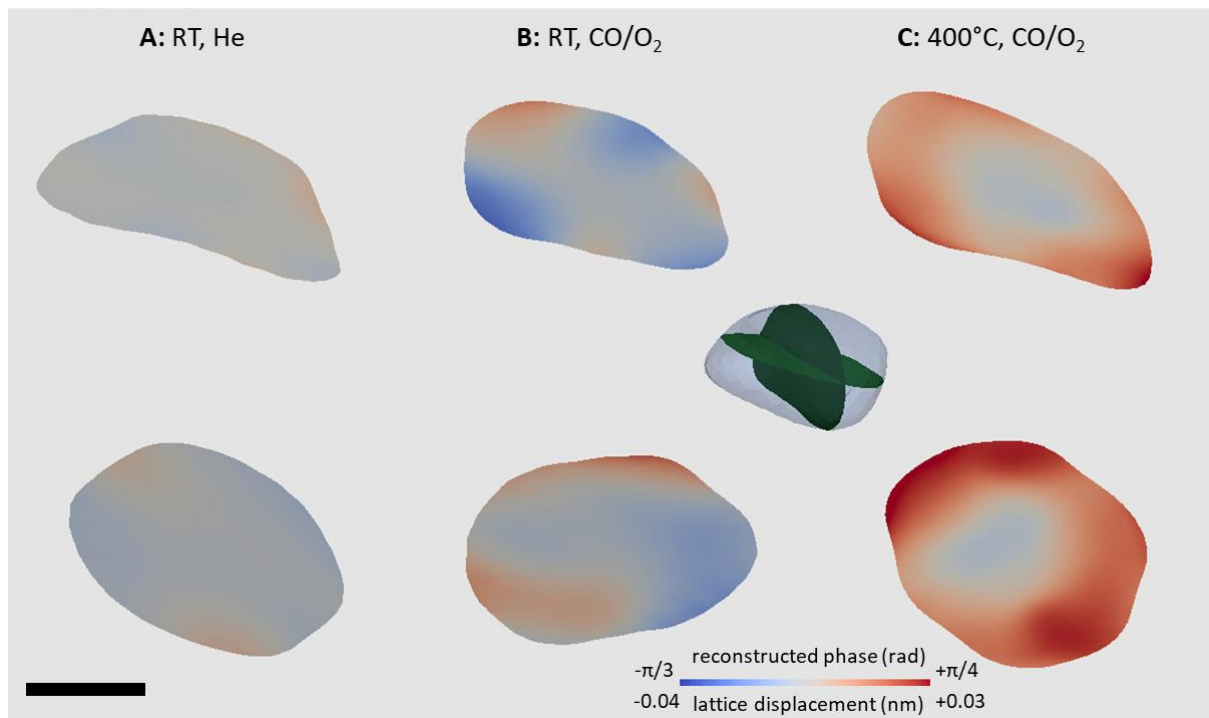


Figure 4.12. Particle cross-sections displaying the phase and lattice displacement, projected along (111) of the interior of the nanoparticle at RT (A) under He, (B) under CO/O₂/He and (C) at 400 °C under CO/O₂/He. As shown in the figure inset, cross-sections are made at the center of the nanoparticle perpendicular (top) and parallel (bottom) to the support. Scale bar corresponds to 100 nm.

CONCLUSIONS

We built a new cell dedicated to *in situ/operando* Bragg CDI measurements, compatible with the beamline set-up described above and covering the needs for the catalysis reaction (3). The utilisation of the cell proved to be reproducible as several particles were measured during the beamtime. By performing *operando* Bragg CDI we could follow the morphology and the 3D phase distribution over individual Au NP during the CO oxidation reaction. We achieved 32-nanometers spatial resolution. This resolution could be further improved by increasing the coherent flux, as it is expected with the upgrade of the SOLEIL synchrotron, and by reducing the large air paths from the optics to the sample and from the sample to the detector (38 cm of air, sample-detector distance corresponds to an attenuation factor of about 30% at 8.5 keV). The

next chapters will present results from the same gold nanocrystals batch studied *in situ* at the 34-ID-C beamline of the Advanced Photon Source (APS) where the coherent flux is higher, allowing us to achieve an improved resolution.

REFERENCES

1. RICHARD, M. I. et al. Reactor for nano-focused x-ray diffraction and imaging under catalytic in situ conditions. **Review of Scientific Instruments**, v. 88, n. 9, p. 093902, 2017.
2. BAIER, S. et al. In Situ Ptychography of Heterogeneous Catalysts using Hard X-Rays: High Resolution Imaging at Ambient Pressure and Elevated Temperature. **Microscopy and Microanalysis**, v. 22, n. 1, p. 178–188, 2016.
3. ROCHET, A. et al. In situ reactor to image catalysts at work in three-dimensions by Bragg coherent X-ray diffraction. **Catalysis Today**, v. in press, 2018.
4. JACQUES, V. L. R. et al. Estimation of coherence properties of an undulator-generated x-ray beam from near-field and far-field slit diffraction visibilities. **Physical Review B**, v. 86, n. 14, p. 144117, 2012.
5. CLARK, J. N. et al. Three-dimensional imaging of dislocation propagation during crystal growth and dissolution. **Nature Materials**, v. 14, n. 8, p. 780–784, 2015.
6. GERCHBERG, R. W.; SAXTON, W. O. A Practical Algorithm for the Determination of Phase from Image and Diffraction Plane Pictures. **Optik**, v. 35, n. 2, p. 237–246, 1972.
7. FIENUP, J. R. Phase retrieval algorithms: a comparison. **Applied Optics**, v. 21, n. 15, p. 2758–2769, 1982.
8. MARCHESINI, S.; HE, H.; CHAPMAN, H.; HAU-RIEGE, S.; NOY, A.; HOWELLS, M.; WEIERSTALL, U.; SPENCE, J. X-ray image reconstruction from a diffraction pattern alone. **Physical Review B - Condensed Matter and Materials Physics**, v. 68, n. 14, p. 140101, 2003.
9. CHEN, C.-C. et al. Application of optimization technique to noncrystalline x-ray diffraction microscopy: Guided hybrid input-output method. **Physical Review B**, v. 76, n. 6, p. 064113, 2007.
10. UCHIYAMA, T. et al. Systematic morphology changes of gold nanoparticles supported on CeO₂ during CO oxidation. **Angewandte Chemie - International Edition**, v. 50, n. 43, p. 10157–10160, 2011.
11. KUWAUCHI, Y. et al. Intrinsic catalytic structure of gold nanoparticles supported on TiO₂. **Angewandte Chemie - International Edition**, v. 51, n. 31, p. 7729–7733, 2012.

12. VENDELBO, S. B. et al. Visualization of oscillatory behaviour of Pt nanoparticles catalysing CO oxidation. **Nature Materials**, v. 13, n. 9, p. 884–890, 2014.
13. WAGNER, J. B. et al. In situ electron energy loss spectroscopy studies of gas-dependent metal-support interactions in Cu/ZnO catalysts. **Journal of Physical Chemistry B**, v. 107, n. 31, p. 7753–7758, 2003.
14. RASHKEEV, S. N. et al. Role of the nanoscale in catalytic CO oxidation by supported Au and Pt nanostructures. **Physical Review B**, v. 76, n. 3, p. 035438, 2007.

CHAPTER V: Watching a Gold Nanocrystal
at Work: from the Core to the Surface of the
Nanoparticle

5. INTRODUCTION

Strained metal surfaces have chemical properties significantly different from those of unstrained surfaces, modifying their reactivity (1). The improvement of catalytic processes can be achieved through the fine understanding of the evolution of strain and the formation of defects in both the surface and the inner core structure of the nanomaterials.

In this chapter, it is reported the first 3D imaging study of defects dynamics and refacetting process of a single gold nanocrystal during CO oxidation reaction, using Bragg CDI. After a short description of the beamline and the experimental conditions used in this study, we will present the main results obtained on the pristine catalyst. We will show that we successfully captured *in situ* the surface restructuring of our model gold catalyst (120 nm) during the catalytic reaction. Under *in situ* conditions, we observed the formation of the catalytic active sites with 12-nanometers spatial resolution. We demonstrate their correlation to the nanocrystal's catalytic activity and unveil the atomistic mechanism taking place.

5.1. BRAGG CDI EXPERIMENTS OF Au NP

5.1.1. Beamline 34-ID-C at APS

In situ Bragg CDI measurements were carried out at the Advanced Photon Source at Argonne National Laboratory, USA at the 34-ID-C beamline, which is dedicated for performing Bragg CDI measurements. A schematic of the beamline is presented in Figure 5.1.

The incident monochromatic coherent X-ray beam with an energy of 9 keV was focused to a size of approximately 500 nm x 500 nm by Kirkpatrick–Baez (KB) mirrors and shines on the sample inside the cell, sealed with a Kapton window. A Timepix detector with 55 x 55 μm^2 pixel sizes, placed 0.43 m away from the sample, recorded the scattered X-rays from a single gold nanocrystal satisfying the (111) Bragg condition.

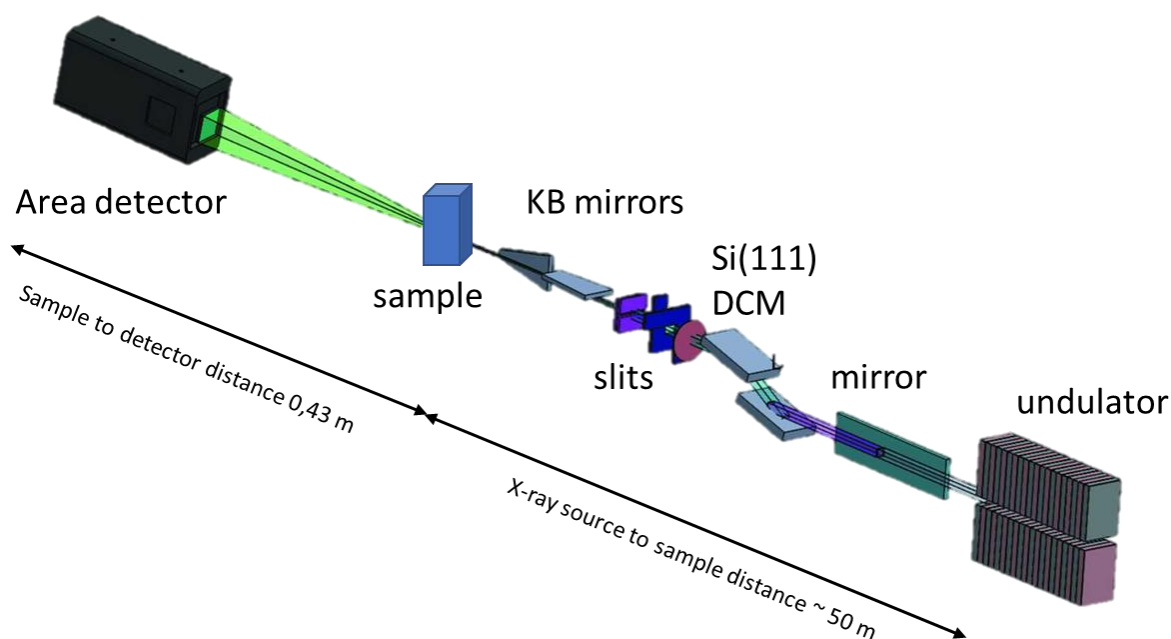


Figure 5.1. Schematic of the 34-ID-C beamline. Adapted from (2).

5.1.2. Experimental conditions

5.1.2.1. Sample preparation

The sample was prepared the same way as for the electron microscopy membranes, described in Annex. 3 μL of the sample $120_Au/TiO_2-m$ (described in Chapter III) dispersed in water, was placed on a 9 windows silicon nitride membrane. The samples were then covered by a Petri dish to minimise contamination and were dried overnight. Figure 5.2 (b) shows a low-magnification SEM image of the membrane where we can distinguish the sample distribution as white dots dispersed over the membrane.

5.1.2.2. Sample environment

A picture of the reactor used to perform *in situ* Bragg CDI experiments is shown in Figure 5.2 (a), where the gas inlet/outlet and electrical connections are displayed. We can also see the silicon nitride membrane clamped with a metallic piece. With a similar design to the cell described in Chapter IV, but with a bigger volume, the heating system is composed of a ceramic heating device, enabling to control the temperature

(up to 900 °C). The cell has a water-cooling system to avoid overheating and damages to the piezo stages.

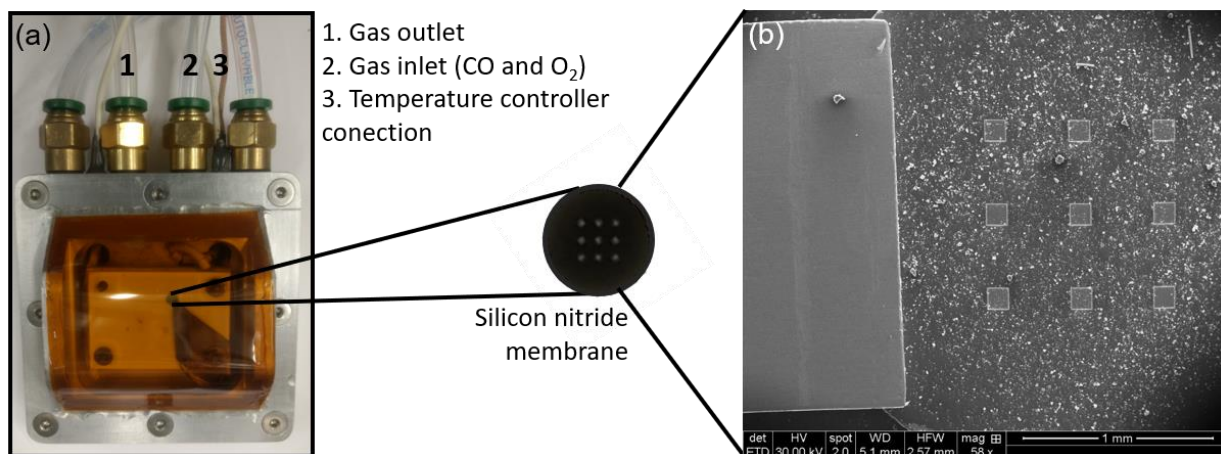


Figure 5.2. (a) The *in situ* cell used for the Bragg CDI experiment, where the gas/temperature connections are shown; (b) SEM image showing the distribution of the sample $120_Au/TiO_2-m$ on the silicon nitride membrane.

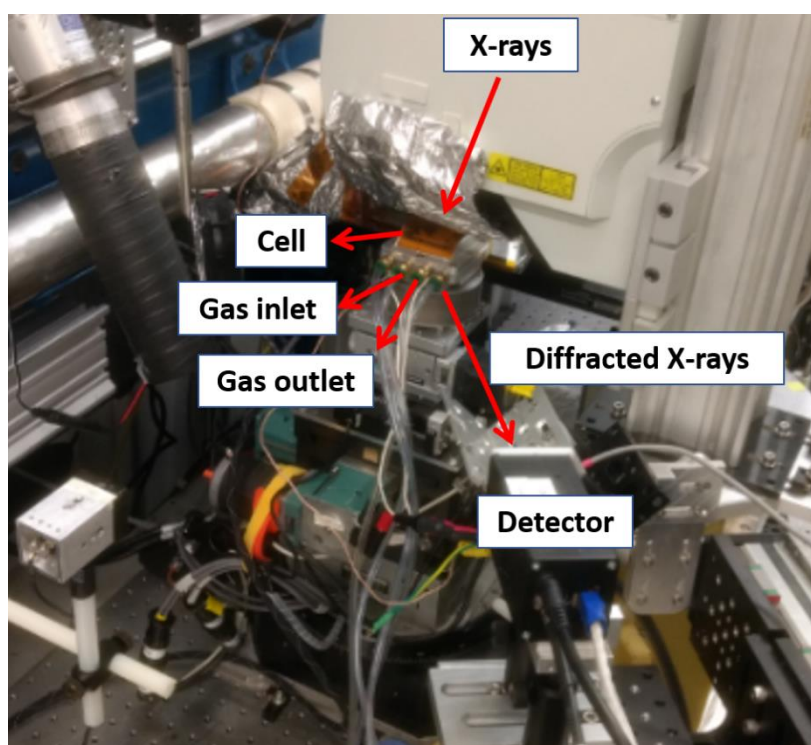


Figure 5.3. Picture of the experimental setup at the beamline 34-ID-C, showing the experimental cell, the gas and electrical connections, the detector position and the incoming/diffracted X-rays.

5.1.2.3. Bragg CDI measurements

The gold catalyst loaded inside the *in situ* cell was installed on the sample stage of the beamline (Figure 5.3) and a sequence of diffraction patterns from the (111) peak of Au were collected covering the whole rocking curve, by rotating the nanocrystal in angular steps of 0.02° over the angular range of 1.2° . Each frame was accumulated with ten exposures of 5 seconds.

5.1.2.4. In situ measurements

The nanocrystals were measured at different temperatures: RT, 200 and 400 °C. At first, we followed the calcination step under air atmosphere. Then we followed the catalytic reaction under a flux of a mixture of 2% of CO in He and 5% of O₂ in N₂, with gas flows of 5 and 14.5 mL·min⁻¹, respectively. The reactive gas mixture results in a CO:O₂ ratio of 0.5%:3.7%.

As it is crucial to follow the same nanoparticle under the different conditions of temperatures and gas, it is essential to track the nanoparticle during the heating process. Indeed, during heating, due to thermal expansion of the setup, the nanocrystal can drift and be lost or not well aligned in the center of rotation. The “semi-manual” procedure, consisting of checking during the whole treatment the alignment of the nanoparticle within the center of rotation described in Chapter II, is used. For this reason, a rather slow heating ramp has been chosen (3 °C/min). After reaching the temperature of interest, after 5 to 10 minutes for stabilisation the ten rocking curves are measured.

We will discuss the measurements and results obtained for a single gold nanocrystal that we followed during the whole thermal treatment. All along the discussion in this Chapter, we studied a unique gold nanocrystal, referred hereafter as *Particle 1*.

Other nanoparticles followed in similar way will be presented in Chapter VI.

5.1.3. Data reconstructions

The data set is inverted using phase retrieval algorithms (3) on *MATLAB R2017b* to produce a real space image of the measured gold nanocrystal. The phasing

algorithm involved iterative switching between real and Fourier spaces through the use of fast Fourier transform until known constraints in each domain had been satisfied. 2220 iterations were run for the images presented hereafter. The iterations consist of alternating 20 iterations of the error reduction (ER) algorithm (4) with 180 iterations of the hybrid-input-output (HIO) algorithm (5) while utilising the Shrinkwrap (6) and guided (7) algorithms. The obtained real space images have a spatial resolution of around 12 nm with a pixel size around 4 nm.

It is noteworthy to mention, several number of iterations during the reconstruction process have been used (from 420 to 2220 iterations) in order to improve the convergence. Figure A1 (Appendix) shows the reconstructions of the gold nanoparticle at RT and air using 420, 620, 820, 1020, 1220, 1420, 1620 and 1820 iterations. A remarkable feature of all the reconstructions with different number of iterations is that the final objects have the same size and shape. The non-variability of these parameters proves that the employed methodology is reliable to recover the electronic density of the object and represents a powerful technique to get insights about the nanoparticle morphology.

5.2. PRISTINE GOLD NANOPARTICLE

Experimentally, successive 2D coherent diffraction patterns are measured around the (111) Bragg peak. Figure 5.4 displays a part of the patterns measured during the rocking of the single gold nanocrystal, collected under air at room temperature. The 2D diffraction patterns are stacked and the fringes seen from the 3D views are enhanced (inset of Figure 5.4). This intensity distribution carries information about the morphology and internal lattice distortions in the crystal, as will be discussed.

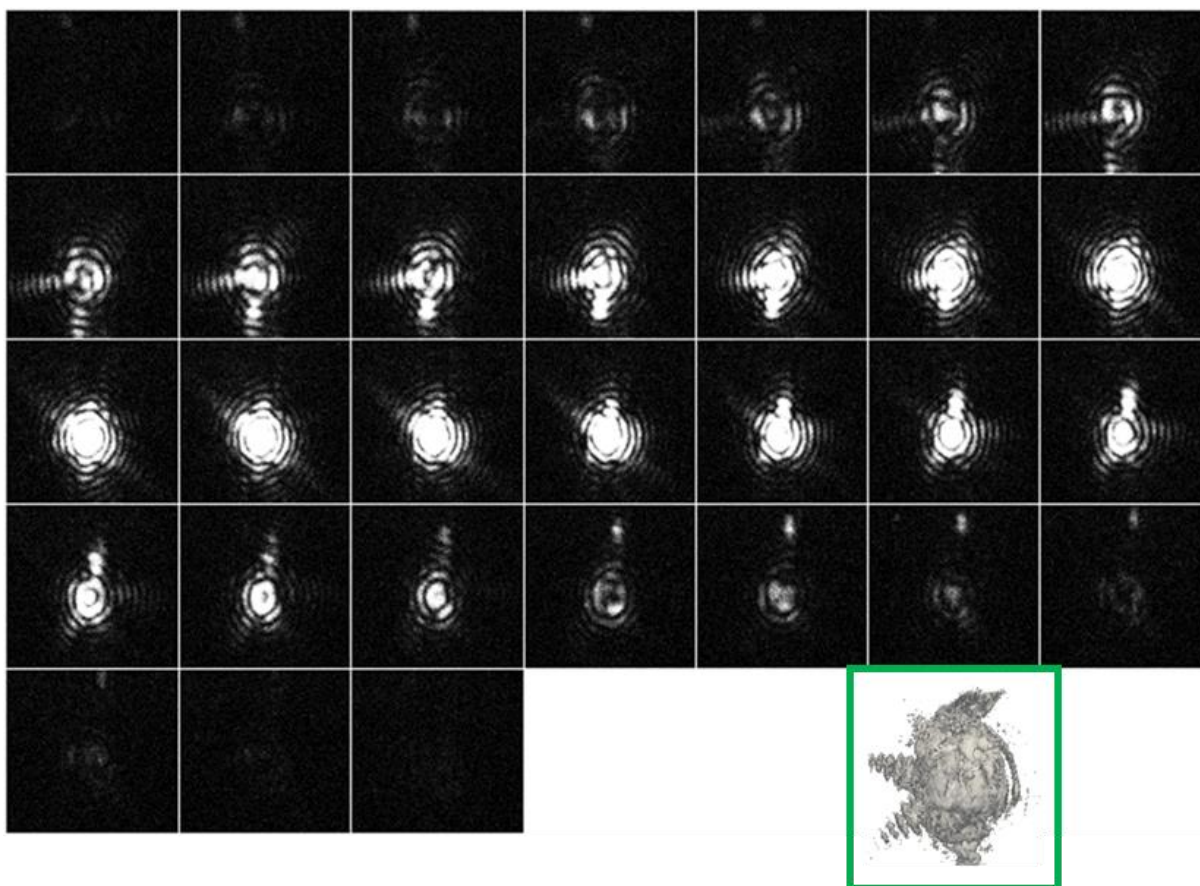


Figure 5.4. Series of 2D coherent diffraction patterns of a gold nanocrystal recorded at RT under air (for sake of clarity, only one every two patterns is shown (0.04°)). Inset: 3D Bragg diffraction peak obtained by stacking the 2D diffraction patterns. The intensity of the diffraction patterns scales from 0 to 128612 counts; the rocking curve was measured by ten exposures of 5 s each of them.

The 3D coherent Bragg peak intensity is inverted to a real space image. Figure 5.5 (a) shows the 3D reconstruction of the Au nanocrystal in air at room temperature, presented from the side, top and bottom views. The reconstruction exhibits a truncated octahedral shape. Moreover, we can clearly identify the (100) and (111) facets.

The STEM image of a gold nanoparticle from the same batch is also shown, demonstrating the accuracy of the reconstruction, both from the morphology and size aspects. The size of the nanoparticle was determined by extracting line scans across of the particle cross-sections (Figure 5.6), leading to 125 nm. This is in good agreement with the sizes reported in Chapter III obtained by SAXS and UV-Vis.

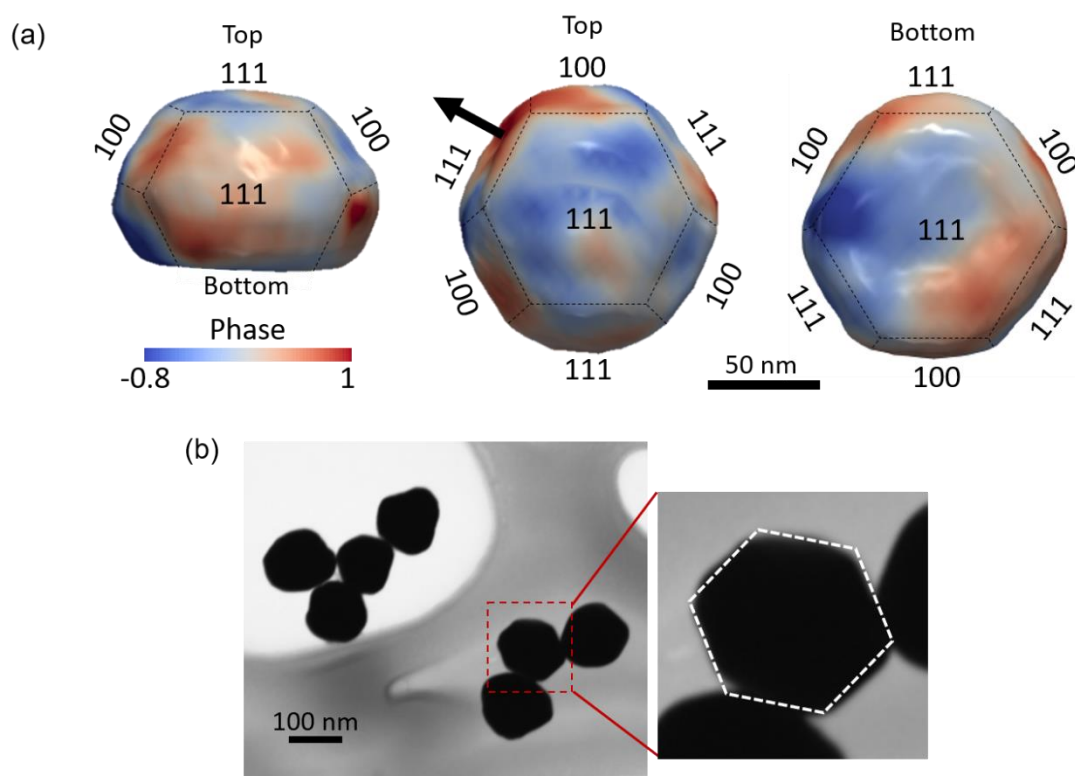


Figure 5.5. (a) Top and bottom views (the scale bar is 50 nm) of a gold nanocrystal recorded at RT under air. The direction of the Q vector is shown in the top view. (b) STEM image of the Au NP (the scale bar is 100 nm). The zoom in region highlights the hexagonal shape of the particle.

Within this work, we reached a spatial resolution of 12 nm. The resolution was determined by taking the derivatives of the line scans across the nanoparticle along the vertical and horizontal directions (Figure 5.6).

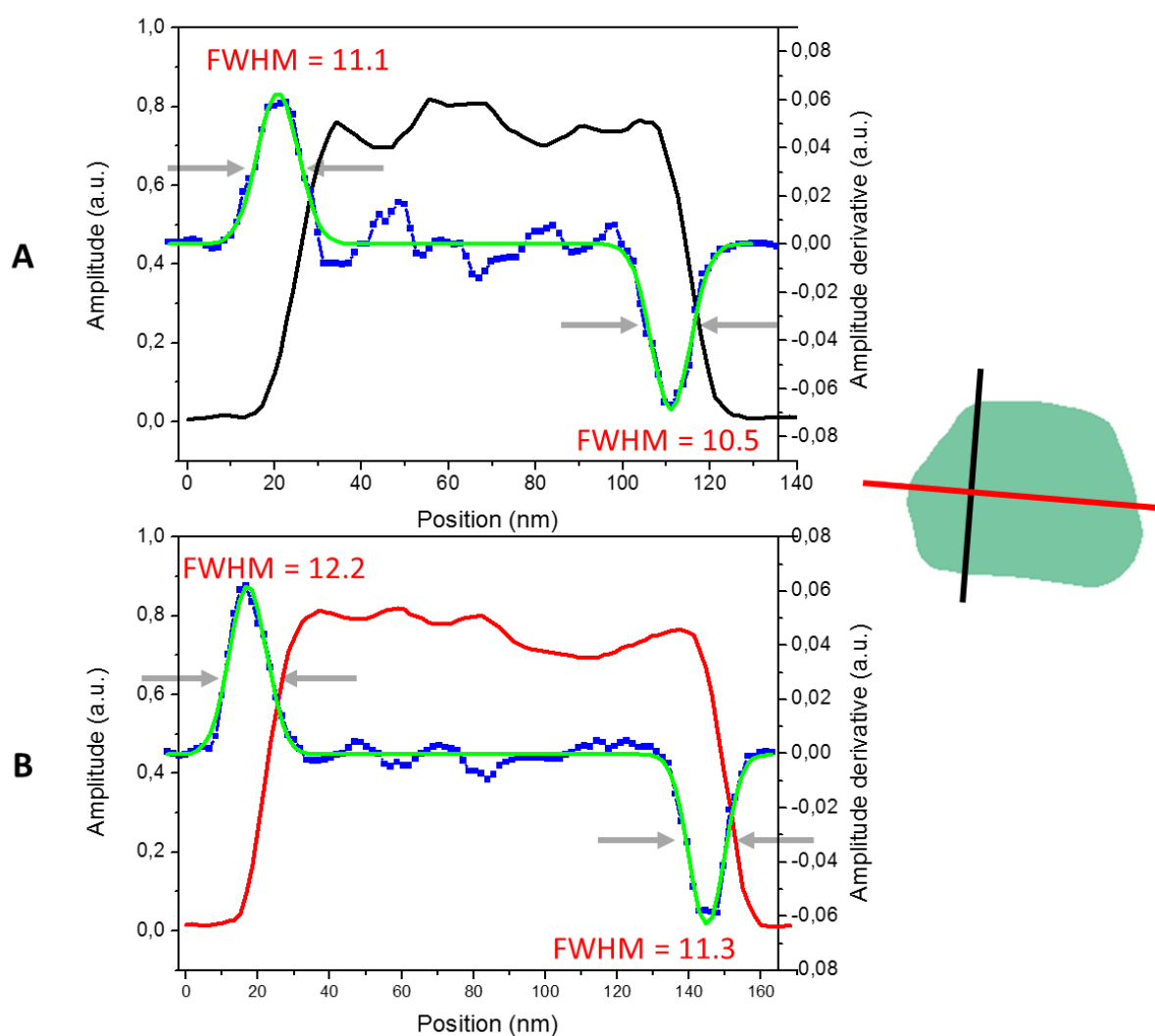


Figure 5.6. Averaged line profiles. Lines (A, black) along the vertical and (B, red) horizontal directions of the particle cross-section presented as a green surface on the right. The derivatives of the line scans are showing that the reconstruction resolution is 12 nm.

5.3. ADSORBATE-INDUCED SURFACE TRANSFORMATIONS

5.3.1. Morphology and lattice displacement

Comparing the Bragg CDI measurements performed at RT under air and CO/O₂ gas mixture reveals the effect of the gas adsorption on the gold nanoparticle. Figure 5.7 presents selected diffraction patterns obtained during the rocking curve measured at RT under CO/O₂. Significant signal is observed on a shorter angular range than on Figure 5.4, measured under air. This is characteristic of a less faceted object (more

strain). This is more obvious in Figure 5.8 (top), within the 3D diffraction peaks where less fringes can be resolved under reactive gas mixture compared with air.

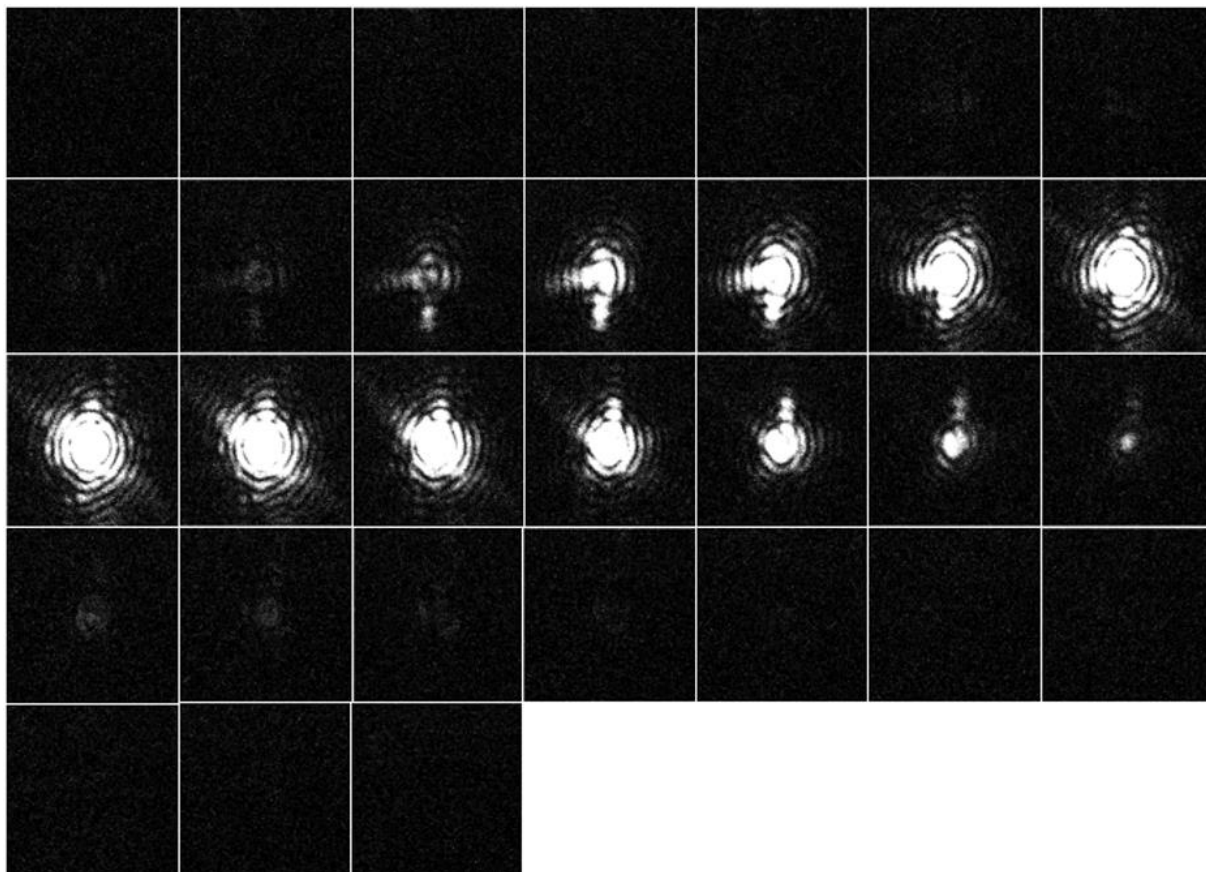


Figure 5.7. Series of 2D coherent diffraction patterns of a gold nanocrystal recorded at RT under CO/O₂ (for sake of clarity, only one over two patterns are shown (0.04°)). The intensity of the diffraction patterns scales from 0 to 115171 counts; the rocking curve was measured by ten exposures of 5 s each of them.

Upon CO/O₂ adsorption, the 3D reconstructions reveal the adsorbate-induced surface transformations occurring onto the Au nanocrystal surface. As already mentioned, the pristine gold nanocrystal reconstruction (RT, air) exhibits a faceted morphology, in agreement with STEM images. The same nanocrystal turns into a smoother and rounded shape in CO/O₂ environment at RT, as shown in Figure 5.8 (bottom). These changes in surface morphology indicate that the gas molecules of O₂ and CO interact strongly with the surface atoms.

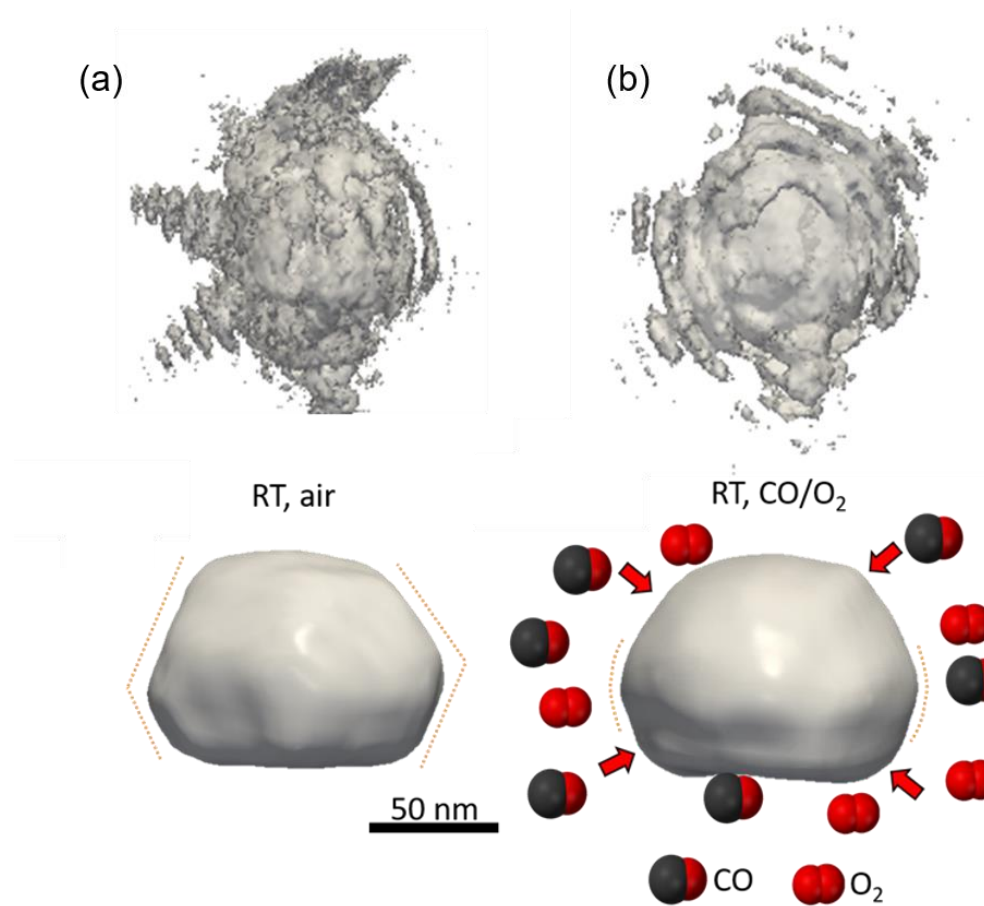


Figure 5.8. Top: 3D Bragg diffraction peak of the gold NP at RT under air (a) and CO/O₂ (b). Bottom: Grey isosurface (30%) representing the particle shape of the same Au/TiO₂ nanoparticle in side view. The dotted lines are showing the faceted and rounder shapes of the nanoparticle.

Moreover, a distinct phase redistribution is observed between the two gas environments at room temperature. The phase shifts of the gold nanocrystal under air and CO/O₂ at RT are displayed as 3D views in Figure 5.9. Cross-section views for both gas atmospheres are presented in Figure 5.10, with the insets showing the position of the presented cross-sections. For both Figures, the phase scale ranges from -0.3 to 0.9, corresponding to lattice displacement values of -11 pm and 34 pm, respectively (for the calculation, equation (6) from Chapter II was used).

As clearly observed on the Figures, the reactive gas mixture CO/O₂ induces a lattice displacement resulting in a smoother phase structure, evidencing the annihilation of several nanocrystal defects.

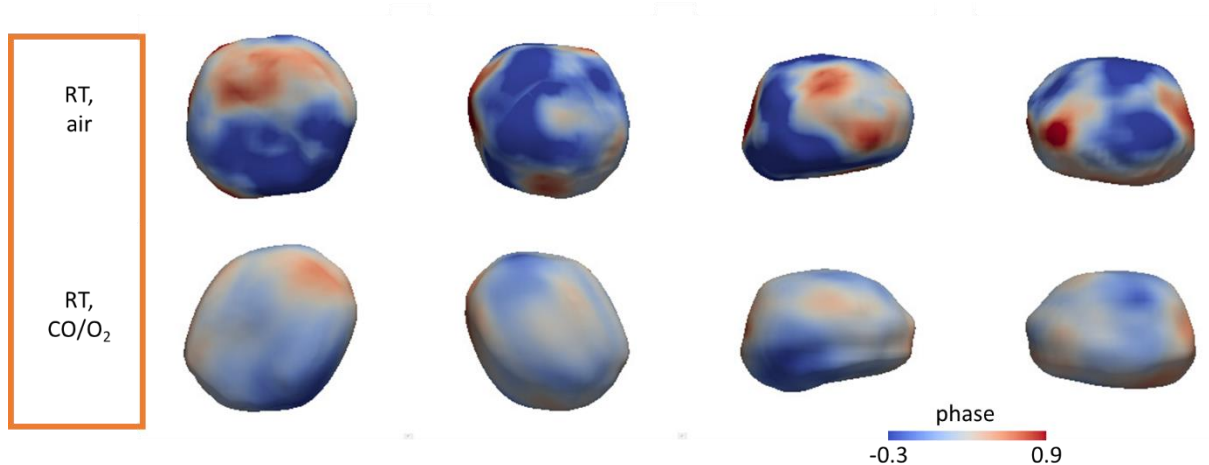


Figure 5.9. Three-dimensional views as function of phase of the gold nanocrystal under both atmospheres, air and CO/O₂ at RT.

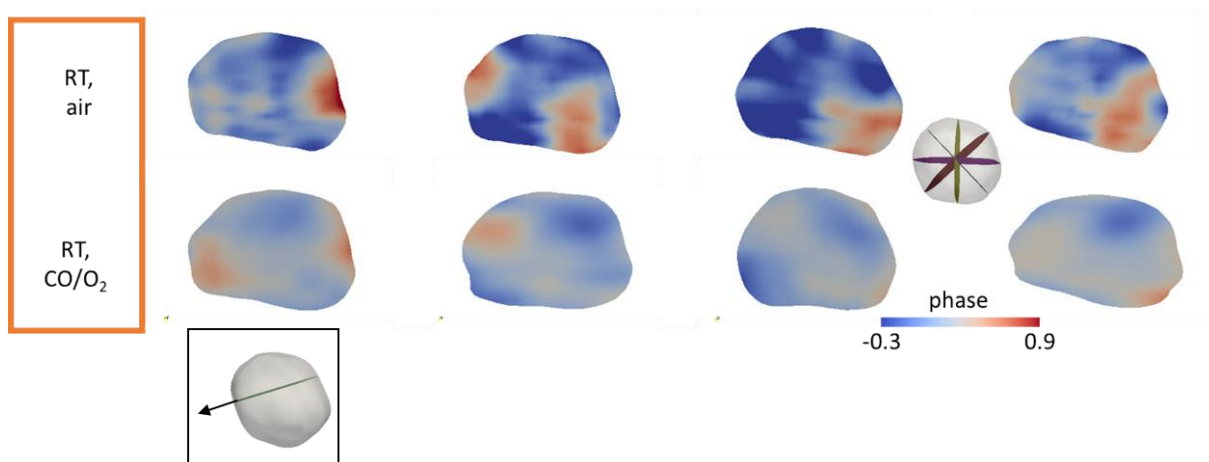


Figure 5.10. Cross-section views as function of phase of the gold nanocrystal under both atmospheres air and CO/O₂ at RT. The inset represents the four cross-section planes shown. The inset in the first column represents the q vector direction.

5.3.2. Strain analysis

The 3D strain distribution of the entire volume along the measurement direction was obtained by taking the derivative of the displacement field resulting from algorithmic phase reconstruction and is defined as $\frac{\partial u_{111}(r)}{\partial x_{111}}$ where $u_{111}(r)$ is the displacement field. Figure 5.11 displays the 3D distribution of the strain field along [111]. Cross-sections are presented in Figure 5.12. As for the phase distribution, the strain is evolving with the gas environment. The highest values of strain are concentrated at the periphery of the nanoparticle. We observe a mean surface

compressive to tensile strain swap during CO/O₂ adsorption on the gold nanocrystal surface. The average surface strain in air equals to $-1.7 \cdot 10^{-4}$ and becomes tensile with a mean value of $1.1 \cdot 10^{-5}$ after CO/O₂ adsorption. This pattern of displacement observed on the surface of the nanocrystal upon CO/O₂ adsorption can be attributed to the decrease of the surface stress, due to the annihilation of point defects.

The surface stress σ_s can be estimated by the Young-Laplace equation (8):

$$\sigma_s = -\frac{3KR}{2} \frac{\Delta a}{a} \quad (11)$$

where $K = 220 \text{ GPa}$ is the bulk modulus of gold, R the radius of the locally rounded region and $\frac{\Delta a}{a}$ the strain. The strain at the position indicated by the green arrow of Figure 5.11 is $-3.5 \cdot 10^{-4}$ for the nanocrystal under air and $3.4 \cdot 10^{-4}$ in CO/O₂. We can estimate the radius R of the locally rounded region is 20 nm. Equation (11) leads to a surface stress of $2.31 \pm 1 \text{ N} \cdot \text{m}^{-1}$ for the nanocrystal under air, typical of tensile surface stress of metals (8,9) in the range of $2 \text{ N} \cdot \text{m}^{-1}$. On the other hand, the surface stress of the nanocrystal under CO/O₂ turns to be compressive and equal to $-2.24 \pm 1 \text{ N} \cdot \text{m}^{-1}$. The adsorbate-induced surface stress on the gold nanocrystal leads to a compressive stress change at RT (between air and CO) of $-4.55 \text{ N} \cdot \text{m}^{-1}$, resulting in the inward displacement of the curved regions. The chemisorption of CO and O₂ molecules on the metal surface will re-establish at least some of the bonds on the surface atoms. If the adsorbate is more electronegative than the surface atoms, then charge should be removed from the bonds metal-adsorbate and be partially transferred to the adsorbed species. That is the case for the CO oxidation reaction as the reactant's molecules are more electronegative than the gold atoms. In this case, the removal of charge from the surface atoms should decrease the tensile stress and could turn it into a compressive one (9,10). The curved and flat regions react differently to CO adsorption, modifying the proportion of under-coordinated sites. The nanocrystal surface modification is directly influenced by the surface stress tuning the catalytic performance of the nanocrystals.

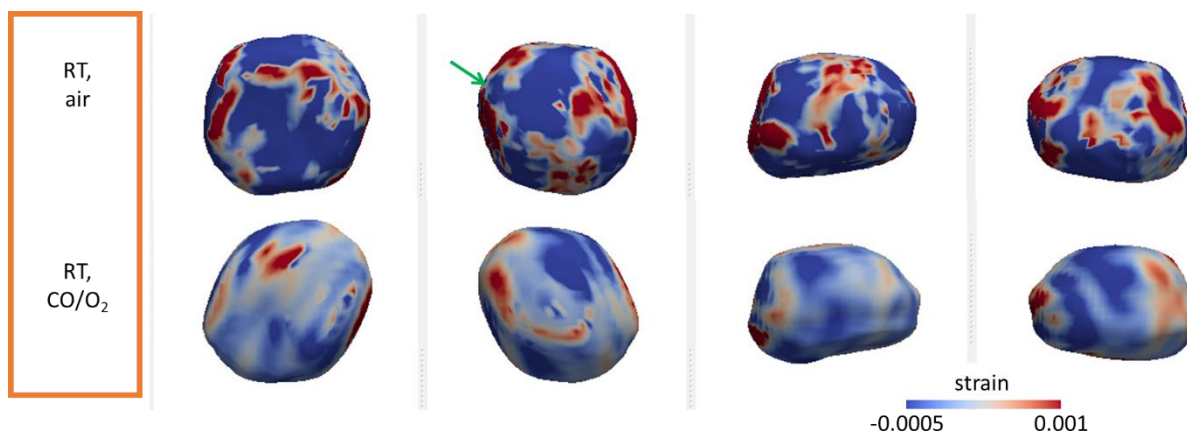


Figure 5.11. Three-dimensional views as function of strain of the gold nanocrystal under both atmospheres air and CO/O₂ at RT.

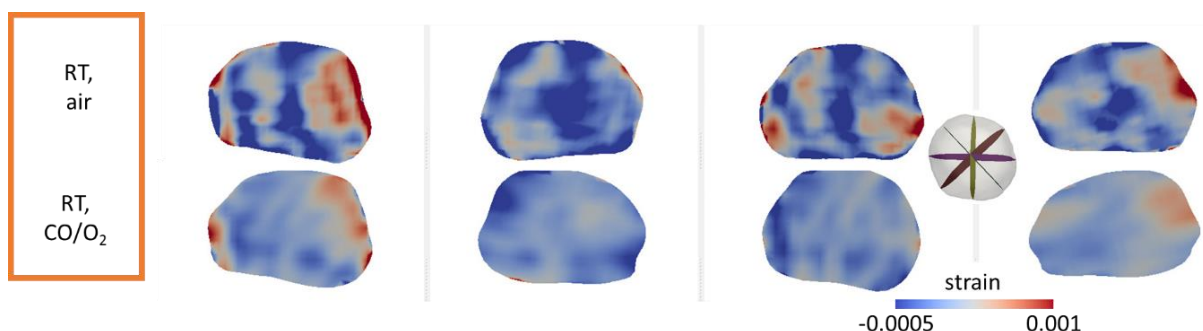


Figure 5.12. Cross-section views as function of strain of the gold nanocrystal under both atmospheres air and CO/O₂ at RT. The inset represents the four cross-section planes shown.

5.4. IN SITU DYNAMICS AND CATALYTIC ACTIVITY

5.4.1. *In situ* surface dynamics

We succeeded in capturing *in situ* the surface restructuring of the same nanoparticle during the catalytic reaction of CO oxidation into CO₂ at 200 °C and 400 °C. The catalyst presents an increased activity at 400 °C compared to 200 °C, and none at room temperature as shown in Figure A2 (Appendix). On the following Figures, a green gradient is illustrating the increase of catalytic activity as function of the temperature. Figure 5.13 and Figure 5.14 show the three-dimensional phase and strain distributions of the same nanocrystal at RT, 200 and 400 °C during the conversion of CO into CO₂, revealing the nanocrystal surface dynamics, with the reconstitution of sharper edges and corners. As previously stated, nanocrystal corners and edges are

regions of low-coordinated atoms and the location of the active sites. The direct correlation between the nanocrystal surface modifications and its catalytic activity is here uniquely unveiled by *in situ* Bragg coherent X-ray diffraction imaging. Furthermore, this surface reshaping is driven by inner modifications as described hereafter.

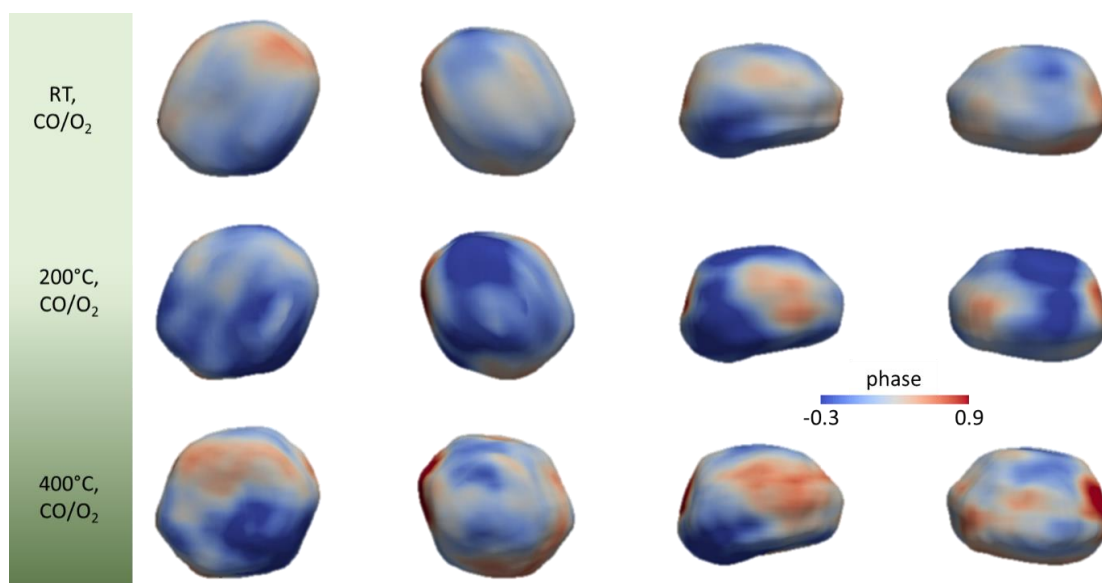


Figure 5.13. Three-dimensional views as function of phase of the gold nanocrystal under CO/O₂ at RT, 200 °C and 400 °C. The green gradient represents the increase of catalytic activity as function of the temperature.

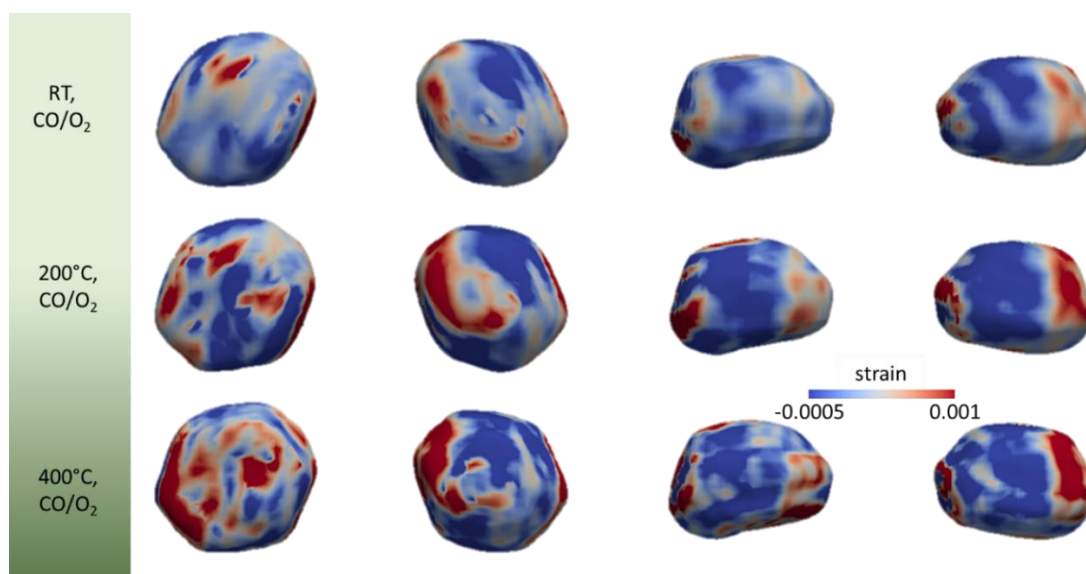


Figure 5.14. Three-dimensional views as function of strain of the gold nanocrystal under CO/O₂ at RT, 200 °C and 400 °C. The green gradient represents the increase of catalytic activity as function of the temperature.

Under working conditions, the surface modifications are also accompanied by a one-fold increase of the average surface strain, reaching $1.35 \cdot 10^{-4}$ and with corner regions of surface stress $> 6 \text{ N.m}^{-1}$. This is in agreement with the “d-band centre theory” (11), the increase of tensile strain can enhance the surface adsorption and lead to improved catalytic activity.

The presence of strain due to the lattice distortions, change the d-band of the metallic nanoparticle: overall, tensile (expansive) strain reduces the orbital overlap, narrowing the d-band. The narrowing caused by tensile strain or lower coordination should lead to an up-shift of the d-band center. An expanded lattice raises the d-band center: a higher d-band center results in stronger bonding in the chemisorption process of the molecules to the metal surface. The altered d-band center affects the interaction with adsorbates (12,13). As the strain clearly modifies the d-band center, reducing or increasing the adsorption energies of the atoms/molecules, the catalytic performance can be improved by tuning the strain.

The huge development of quantum theoretical calculations is allowing us to calculate energy barriers, adsorption energies and activation energies for processes occurring on metallic nanoparticles surfaces. Changes in the lattice constant inducing strain are relatively simple to calculate and offer information regarding the reactivity of the nanoparticles. Hammer and Nørskov (12,14) have demonstrated that changes in electronic structure on the surface causes predictable changes in the surface chemical properties, for example, the adsorption energy of molecules. In this approach, the authors succeeded in correlating the energy of the d-band state and the chemisorption energy of atoms/molecules, demonstrating that it is possible to correlate the electronic states with the catalytic performance. A correlation between the energy of the d-band and the adsorption energy of several atoms and small molecules was established.

5.4.2. Nanotwin network formation

The surface modifications are accompanied by strong lattice dynamics in the core structure of the nanocrystal, along with anisotropic strain patterns are observed (Figure 5.15 and Figure 5.16). The phase evolution between the nanocrystal at RT, 200 °C and its catalytic active state at 400 °C is emphasised in the line scans (Figure 5.17), the latter exhibiting an oscillatory behaviour. Each phase oscillation corresponds

to an atomically defective domain, spanning across the nanocrystal and forming a network of parallel ribbons with strained interfaces. At 400 °C it is clear the presence of these ribbons seen in both plots (phase and strain) crossing the nanocrystal. These defects enable accommodating the tensile strain which built up within the nanocrystal and is attributed to a nanotwin network.

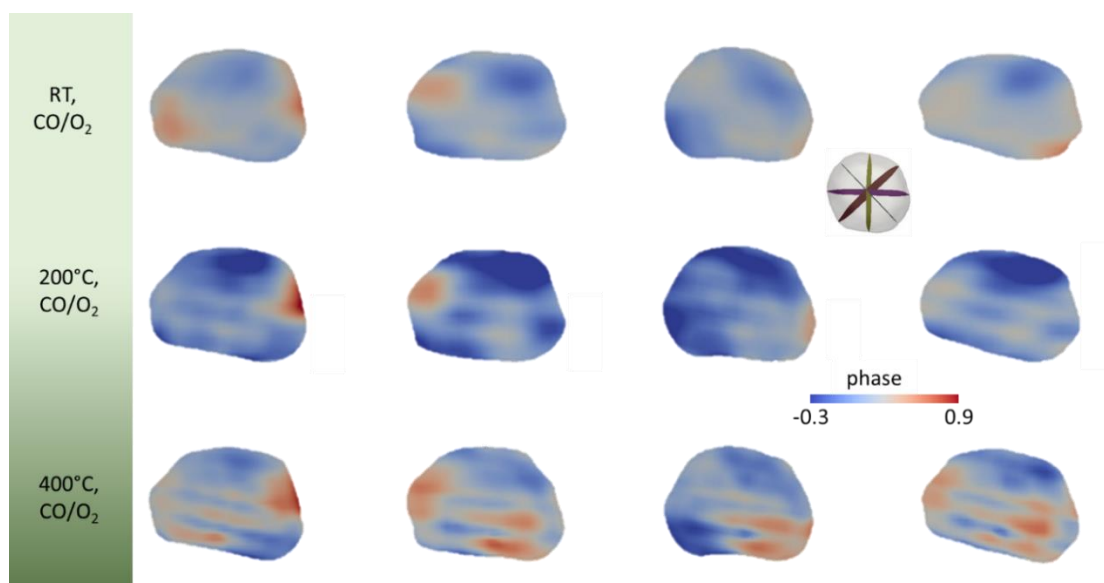


Figure 5.15. Cross-section views as function of phase of the gold nanocrystal under CO/O₂ at RT, 200 °C and 400 °C. The inset represents the four cross-section planes shown. The green gradient represents the increase of catalytic activity as function of the temperature.

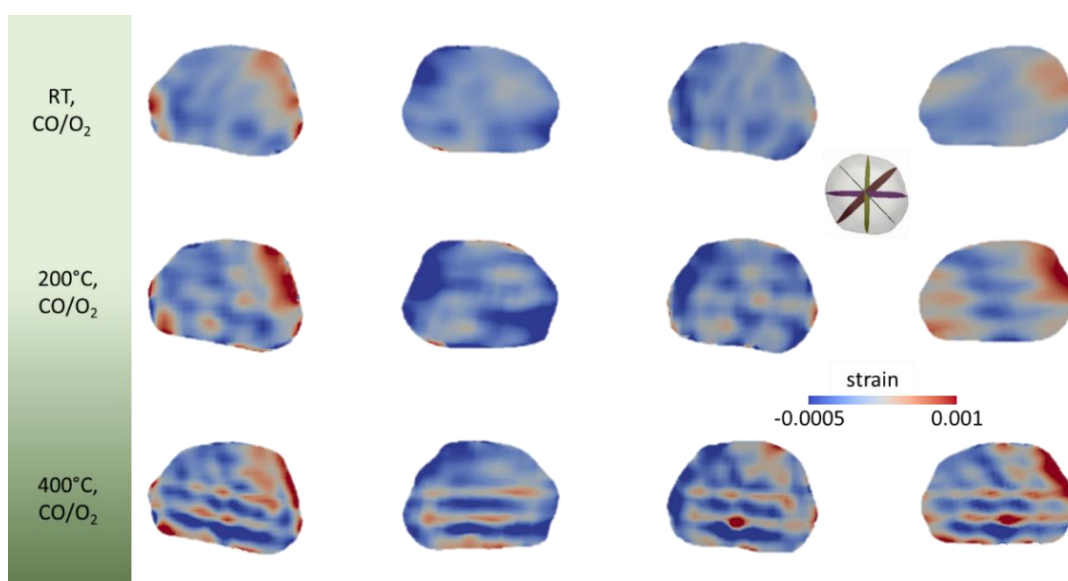


Figure 5.16. Cross-section views as function of strain of the gold nanocrystal under CO/O₂ at RT, 200 °C and 400 °C. The inset represents the four cross-section planes shown. The green gradient represents the increase of catalytic activity as function of the temperature.

Indeed, twin domains are planar defects comprised of at least two adjacent stacking faults. They occur when a stacking sequence of planes share one of these planes and follow a mirrored packing order (15). Instead of the usual ABCABC... sequence of the $\{111\}$ planes, twin domains can be formed by the stacking ABCABC**BACB**ABCABC... (bold letters mark the planes belonging to the twinned crystal, the underlined the shared ones), as highlighted in Chapter II. Twin domains should be “invisible” in the retrieved Bragg electron density maps, since the twin crystal does not satisfy the Bragg condition (15). The phase offset between the parent crystals should be proportional to the twin width, although the twin boundary interfaces as well as the strain contribute to the phase variations explaining the lower phase offset observed here.

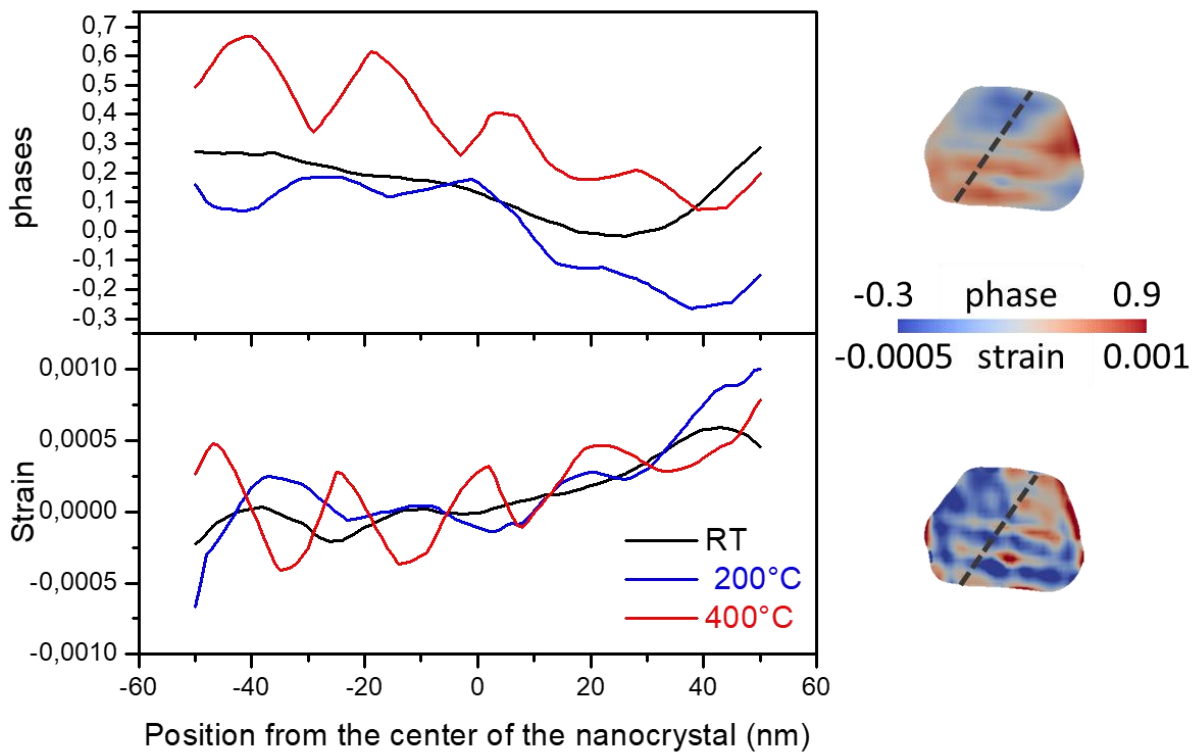


Figure 5.17. Line scans of the phase and strain along the dashed line of the cross-sections presented for illustration at 400 °C under CO/O₂. The black line corresponds to the gold catalyst at room temperature, with no catalytic activity, the blue line to the same cross section at 200 °C, and the red line to the same, but active gold catalyst at 400 °C.

Since the nanotwins are smaller than the resolution achieved here (12 nm) they cannot be faithfully reconstructed, but the network and their positions are indeed resolved to a much higher precision, as shown by the black arrows in Figure 5.18.

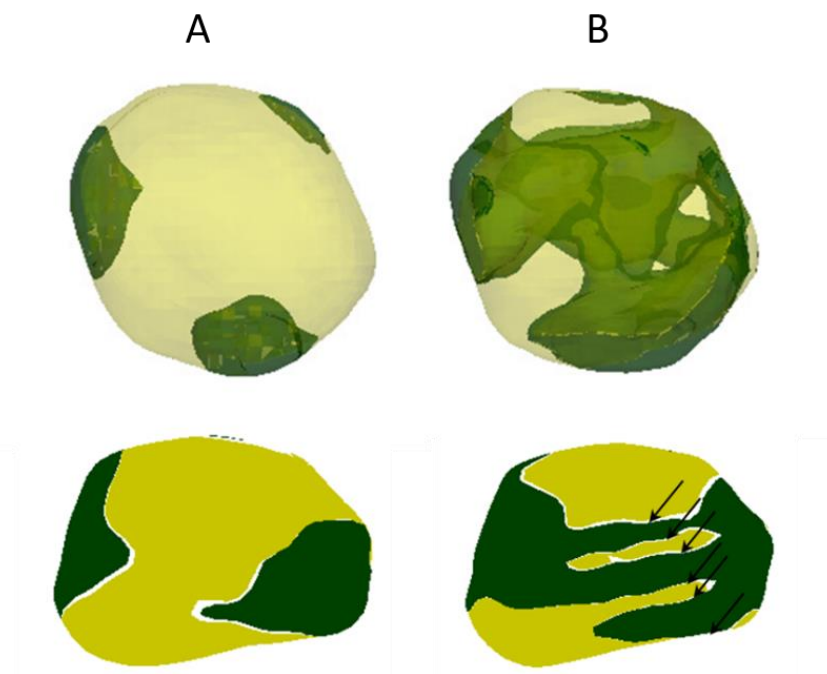


Figure 5.18. 3D and cross sections of the distribution of the low (yellow) and high (green) phase shift of the same Au/TiO₂ nanoparticle under CO/O₂ at 200 °C (A) and 400 °C (B). The black arrows indicate the position of the nanotwin network.

The nanotwins play a crucial role in the deformation mechanism, facetting process and catalytic behaviour of the gold nanocrystals. The large positive surface stress at 400 °C under reactive condition, is the trigger to the surface reconstruction through a glide motion. According to dislocation theory (16), glide motion is performed by the movement of a dislocation or the formation of two partial dislocations (Shockley partials), the latter being energetically more favourable than a single dislocation in the case of fcc metals. When surface stress is applied (Figure 5.19), Shockley partial dislocations are emitted leading to the twin nucleation which propagate across the nanocrystal. The nanotwin network is well evidenced in Figure 5.19, showing its formation between 200 and 400 °C, which correlates with the increased catalytic activity of the gold nanocrystal.

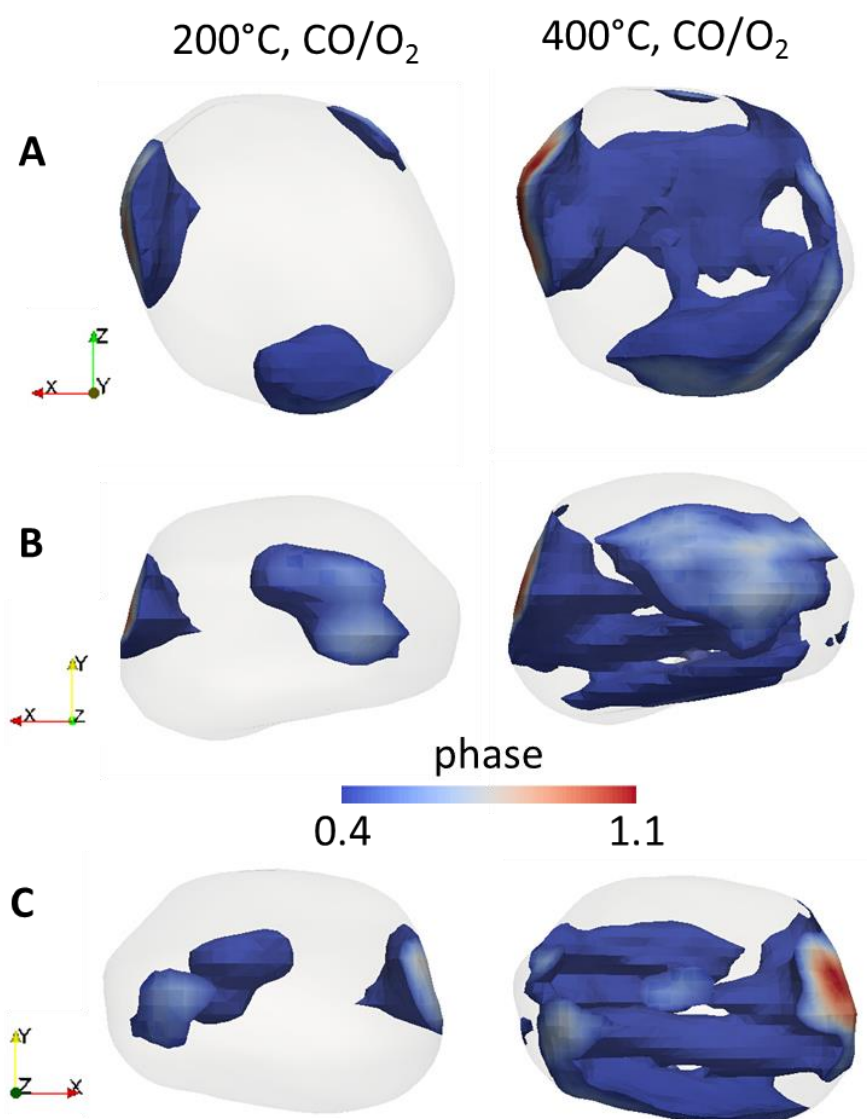


Figure 5.19. Phase shift distribution for the Au nanocrystal at 200 and 400 °C under CO/O₂. Distribution of the maximum phase (0.4-1.1) of the same Au/TiO₂ nanoparticle under CO/O₂ at 200 °C in top view (A) and at 400 °C in top (B) and side view (C). The crystal at 200 °C shows highly distorted areas concentrated at the surface. At 400 °C, a complex network is present with highly distorted areas crossing the entire volume of the crystal.

It is important to notice that the same features are not seen for the nanoparticle measured under air at the most reactive temperature (400 °C), as shown in Figure 5.20 where cross-sections displayed as function of both, phase and strain seems to have random distribution over the crystal.

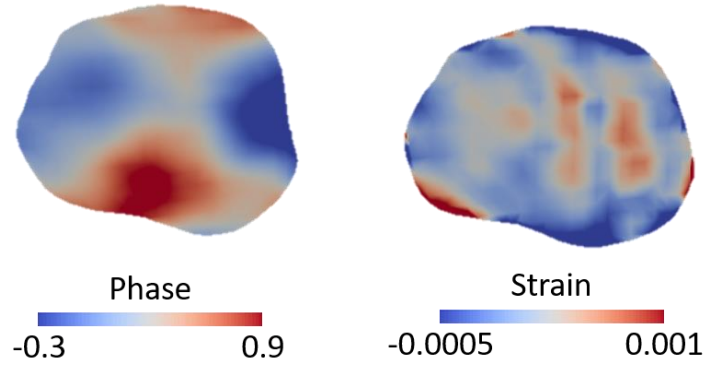


Figure 5.20. Cross-section views of the nanoparticle measured at 400 °C under air in function of both, phase and strain.

5.4.3. Strain energy density

The formation of defects, or nanotwin network enables accommodating the tensile strain which built up within the nanocrystal. We can estimate the elastic strain energy E_s and the strain energy density (*i.e.* strain energy per volume) using the three-dimensional strain distribution.

Strain energy is the energy stored in the body due to deformation. When force or load is applied it undergoes some deformation in shape, size and length, as revealed by the 3D strain maps.

According to equation (12), the strain energy density can be determined:

$$E_s = \int \frac{1}{2} \sum_{ij} \sigma_{ij} \varepsilon_{ij} dV = \frac{2G + 3I}{2} \int \left(\frac{\partial u_{111}}{\partial x_{111}} \right)^2 dV = \frac{3}{2} K(T) \int \left(\frac{\partial u_{111}}{\partial x_{111}} \right)^2 dV \quad (12)$$

where K is the bulk modulus for gold (220 GPa) and the volume integral is over the entire Bragg electron density.

A component of strain, which is projected on the momentum transfer vector (111) is used to evaluate the elastic strain energy. Because gold is cubic lattice structure, it is sufficient to represent the strain energy over the volume (17). It turns out that the strain energy density is varying from $2.73 \cdot 10^4$ to $6.85 \cdot 10^4$ J·m⁻³ between room temperature and 400 °C (Table 2).

As we observed above, the introduction of structural defects, nanotwins may reduce the strain energy and sustain stability of the nanostructure, which usually occurs in large (> 100 nm) nanoparticles. However, it does not relieve the strain to the level of single nanoparticles (18), neither to single crystals, because the magnitude of the elastic strain energy density is approximately four times higher than that of the single nanocrystals (Table 2).

Table 2. Evolution of the strain energy and strain energy density as function of temperature.

Temperature	RT	200 °C	400 °C
Strain energy (aJ)	26.58	63.04	63.91
Strain Energy Density (J·m ⁻³)	2.73 x 10 ⁴	6.73 x 10 ⁴	6.85 x 10 ⁴

CONCLUSIONS

In this chapter we showed the results regarding the Bragg CDI experiment where we measured the sample *120_AuTiO₂-m in situ* under ambient pressure (air and CO/O₂ atmospheres) and at elevated temperatures (up to 400 °C). This is the first work describing *in situ* 3D imaging of a single gold catalyst under realistic working conditions for the CO oxidation. We reach a spatial resolution of 12 nm. We were able to track a single gold nanocrystal at different temperatures and measure its strain response to different gas atmospheres, nonreactive and reactive.

We observe and quantify the adsorbate-induced surface stress on the gold nanocrystal, leading to the surface restructuring. Furthermore, the present study discerns the role of nanotwin network in the deformation of the gold nanostructure and sheds further light on the defects mechanisms responsible for its catalytic properties.

This work is an illustration of the importance of *in situ/operando* defect dynamics imaging and it paves the way to elucidate chemical processes at the single nano-object level towards defect-engineering nanomaterials.

REFERENCES

1. MAVRIKAKIS, M.; HAMMER, B.; NØRSKOV, J. K. Effect of Strain on the Reactivity of Metal Surfaces. **Physical Review Letters**, v. 81, n. 13, p. 2819–2822, 1998.

2. LI, L. et al. Methods for operando coherent X-ray diffraction of battery materials at the Advanced Photon Source. **Journal of Synchrotron Radiation**, v. 26, n. 1, p. 220–229, 2019.
3. CLARK, J. N. et al. Three-dimensional imaging of dislocation propagation during crystal growth and dissolution. **Nature Materials**, v. 14, n. 8, p. 780–784, 2015.
4. GERCHBERG, R. W.; SAXTON, W. O. A Practical Algorithm for the Determination of Phase from Image and Diffraction Plane Pictures. **Optik**, v. 35, n. 2, p. 237–246, 1972.
5. FIENUP, J. R. Phase retrieval algorithms: a comparison. **Applied Optics**, v. 21, n. 15, p. 2758–2769, 1982.
6. MARCHESINI, S. et al. X-ray image reconstruction from a diffraction pattern alone. **Physical Review B - Condensed Matter and Materials Physics**, v. 68, n. 14, p. 140101, 2003.
7. CHEN, C.-C. et al. Application of optimization technique to noncrystalline x-ray diffraction microscopy: Guided hybrid input-output method. **Physical Review B**, v. 76, p. 064113, 2007.
8. ROBINSON, I. Nanoparticle Structure by coherent X-ray diffraction. **Journal of the Physical Society of Japan**, v. 82, n. 2, p. 1–7, 2013.
9. HAISS, W. Surface stress of clean and adsorbate-covered solids. **Reports on Progress in Physics**, v. 64, n. 5, p. 591–648, 2001.
10. IBACH, H. The role of surface stress in reconstruction, epitaxial growth and stabilization of mesoscopic structures. **Surface Science Reports**, v. 29, n. 5–6, p. 195–263, 1997.
11. SUN, J. et al. Gold micromeshes as highly active electrocatalysts for methanol oxidation reaction. **RSC Advances**, v. 7, n. 36, p. 22479–22484, 2017.
12. HAMMER, B.; NØRSKOV, J. K. Theoretical surface science and catalysis—calculations and concepts. **Advances in Catalysis**, v. 45, n. 2, p. 71–129, 2000.
13. SNEED, B. T.; YOUNG, A. P.; TSUNG, C.-K. Building Up Strain in Colloidal Metal Nanoparticle Catalysts. **Nanoscale**, v. 7, n. 29, p. 12248–12265, 2015.
14. HAMMER, B.; NØRSKOV, J. K. Electronic factors determining the reactivity of metal surfaces. **Surface Science**, v. 343, n. 3, p. 211–220, 1995.
15. ULVESTAD, A. et al. 3D Imaging of Twin Domain Defects in Gold Nanoparticles. **Nano Letters**, v. 15, n. 6, p. 4066–4070, 2015.
16. HULL, D.; BACON, D. J. **Introduction to dislocations**. Amsterdam: Elsevier/Butterworth-Heinemann, 2011.

17. ULVESTAD, A. et al. Single Particle Nanomechanics in Operando Batteries via Lensless Strain Mapping. **Nano Letters**, v. 14, n. 9, p. 5123–5127, 2014.
18. KIM, J. W. et al. 3D Bragg coherent diffractive imaging of five-fold multiply twinned gold nanoparticle. **Nanoscale**, v. 9, n. 35, p. 13153–13158, 2017.

CHAPTER VI: Looking *In situ* at Twinned Nanoparticles

6.1. INTRODUCTION

Twins can be produced during the crystal growth, heat treatment or mechanical deformation. For fcc metals, like gold, the twin boundaries can be coherent (CTB) and incoherent (ITB). The CTB present low-energy and a mirrored stacking order can be seen in the twin and parent crystal. The ITB has high boundary energy and a partial dislocation on each slip plane (1).

In this chapter we discuss on Bragg CDI measurements performed on nanoparticles presenting those twin defects after synthesis. We applied the same experimental method with *in situ* Bragg CDI to follow both the calcination under air (for a crystal referred as *Particle 2*) and the catalytic reaction under CO/O₂ (for a nanoparticle referred as *Particle 3*). The studied nanocrystals (*120_Au/TiO₂-a* from Chapter III) are from the same batch of the one presented in Chapter V and their reconstruction was done using the same parameters.

6.2. TWINNED GOLD NANOCRYSTAL UNDER AIR

The particle, called *Particle 2*, was measured under air at three temperatures: RT, 200, 400 °C.

6.2.1. Pristine twinned nanoparticle

Figure 6.1 shows a sequence of 2D Bragg peaks recorded for *Particle 2* measured at RT under air atmosphere. The central 2D diffraction pattern is the one inside the red square and represents the pattern measured at the middle of the rocking curve. If we compare these 2D patterns with the ones recorded for *Particle 1*, the distinct changes seen are clear: while the patterns recorded for *Particle 1* are more symmetric, where the fringes assume a form similar to a ring (section 5.3), the current patterns are much more asymmetric. This is indicative of strain in the nanostructure of the gold nanocrystal under study.

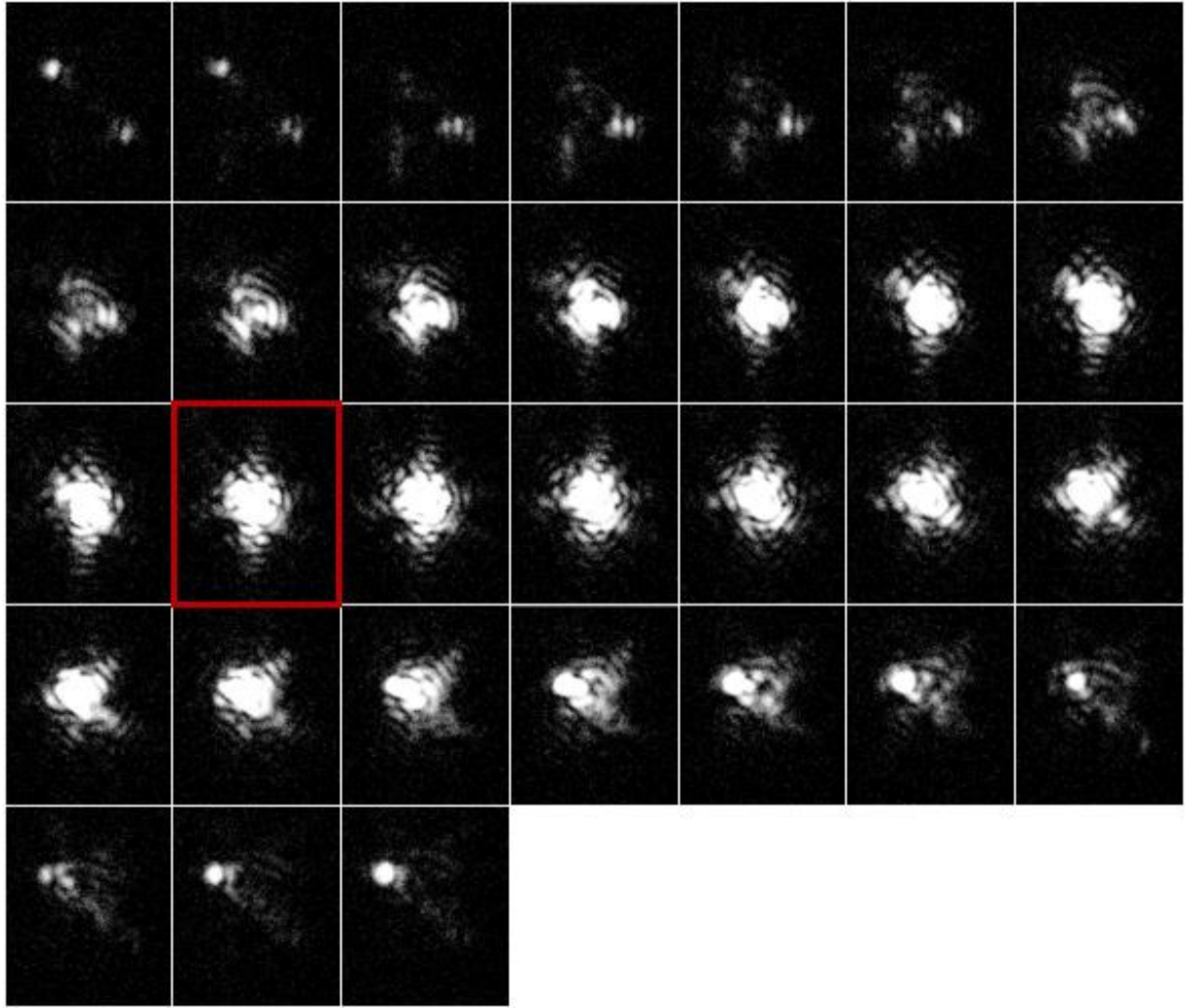


Figure 6.1. Series of 2D coherent diffraction patterns of a gold nanocrystal (*Particle 2*) presenting twin defects recorded at RT under air (for sake of clarity, only one every two patterns is shown (0.04°)). The intensity of the diffraction patterns scales from 0 to 84120 counts; the rocking curve was measured by ten exposures of 5 s each of them.

Figure 6.2 (a) shows the reconstructed gold nanocrystal for the measurement done at RT under air. A notable feature of this structure is that there are three pieces satisfying the chosen Bragg condition (denoted as 1, 2 and 3 in the Figure) and two regions where there is no electron density, the so-called missing Bragg electron density. This means that for these two missing segments, the crystalline lattice was not well oriented for the chosen Bragg condition, *i.e.* the (111) reflection. This corresponds to the presence of twins. Indeed, the formation of twin boundaries involves shearing of crystal planes and the final structure assumes a new orientation. In this process, the atoms of the original crystal structure are called “parent” and the

misoriented crystal is the “twin”, and it is the mirrored reflection of the original crystalline structure, as shown in Figure 6.3 (2).

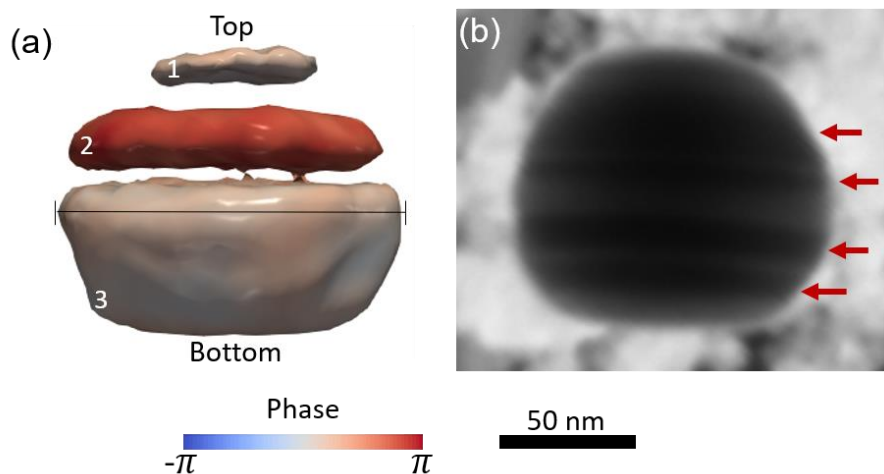


Figure 6.2. (a) Reconstruction of the 120 nm Au/TiO₂ catalyst measured at RT under air in function of phase. 1, 2 and 3 correspond to the three pieces of the parent crystal; the designation of the top/bottom parts is shown. (b) STEM image of another nanoparticle from the same batch; the red arrows point to regions of darker contrast, characteristic of twin domains. The scale bar is 50 nm for both, the reconstruction and the STEM image.

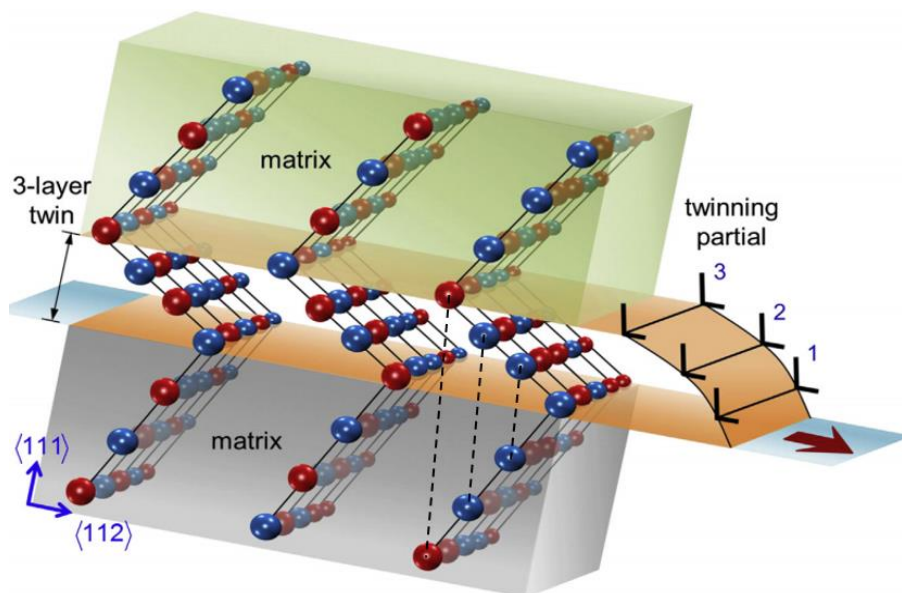


Figure 6.3. Twinning domains formation for the (111) planes. The black dotted lines link the parent crystal, here called matrix, with the twinned crystal, which is formed as the mirrored images of the original structure. Figure from reference (2).

Figure 6.2 (b) displays a STEM image (dark field mode) of one single gold nanoparticle prepared in the same batch as *Particle 1*. We can see the similarity in

terms of size between the reconstructed object and the STEM picture (130 nm in the direction represented by the black line in the Figure 6.2 (a)), demonstrating agreement between the Bragg CDI reconstruction and electron microscopy. Another feature seen in the STEM picture is the presence of stripes with lighter/darker contrasts distributed horizontally across the nanoparticle, as pointed by the red arrows and attributed to the presence of several twin domains inside the nanoparticles.

6.2.2. Calcination treatment

Figure 6.4 shows the reconstructed twinned gold nanocrystal (*Particle 2*) at three different temperatures (RT, 200 and 400 °C) under air. We notice a phase switch in parent piece 2 from RT to 200 °C, going from $+\pi$ to $-\pi$ values and then it comes back to positive values at 400 °C. This could be due to the fact that the positive and negative values of π are the same from the physical point of view: if one atom is displaced by $+\pi$ in the crystal lattice or the atom right above is displaced by $-\pi$, they will be at the same position. Physically, it is equivalent. Both objects will give the same diffraction pattern and there is an indetermination in the reconstruction process.

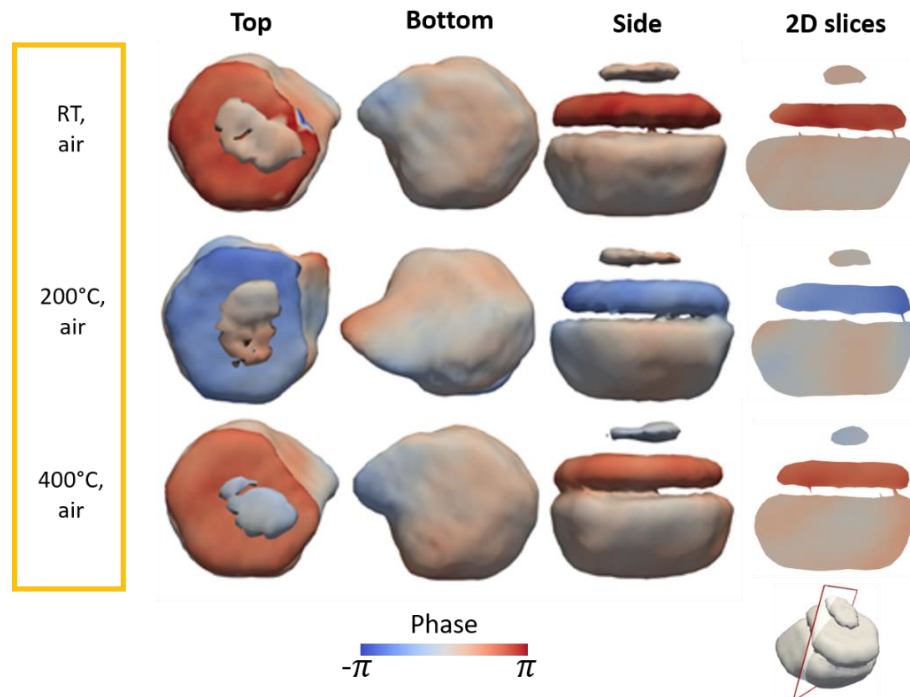


Figure 6.4. Reconstructions in function of phase for the nanoparticle measured under air at the three different temperatures (RT, 200 °C and 400 °C) showed in top, bottom and side views. The last column shows 2D slices taken as shown in the inset below the slices.

Unlike the widely described coherent twin boundaries (CTBs), where the interface between the parent/twinned crystal is assumed perfect, most of the real nanocrystals present irregular interfaces between the twin and the parent crystal. At room temperature, the phase offset between the parent regions 1-2 and 2-3 is approximately -2.09 rad or $-2\pi/3$, indicating perfectly coherent twin boundary interfaces. With increasing temperature, the phase offset slightly decreases between the parent regions 2 and 3 (Table 3). The coherent twin boundaries become defective with incoherent segments and these defects along with strain will lead to deviations from the theoretical values in the measured phase offsets (3,4). It is known that coherent twin boundaries can be very mobile during heat treatment (5). However only a slight decrease in the twin domain size (between 2-3) is observed during the heating. The thermal stability of the twin domains indicates that the local lattice structure has reached a free energy minimum during the annealing pre-treatment (400 °C).

Table 3. Phase offset and distance between the parent and twin portions.

Temperature	Phase offset (rad) 1-2	Phase offset (rad) 2-3	Distance (nm) 1-2	Distance (nm) 2-3
RT	2.1	2.0	19.2	13.3
200 °C	1.7	1.9	20.0	13.0
400 °C	2.1	1.3	19.0	9.6

6.3. TWIN GOLD NANOCRYSTAL UNDER CO/O₂

After the calcination treatment under air, *Particle 2* was placed under CO/O₂ gas mixture at RT. Figure 6.5 compares the reconstructions of *Particle 2* under both gas conditions. As already shown in Chapters IV and V, it is noticeable the corners become more rounded for the particle measured under the reactive atmosphere, as highlighted by the yellow marks. This can be explained by the adsorbate-induced surface transformation described in Chapter V.

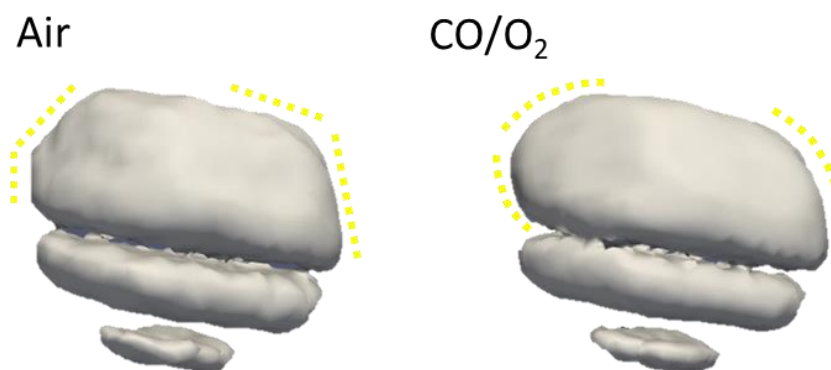


Figure 6.5. Reconstructions of the nanoparticle measured at RT under air (left) and under CO/O₂ (right). The yellow marks are showing the faceted and rounder shapes of the nanoparticle, depending on the gas environment.

Unfortunately, because of the unexpected loss of the diffraction signals due to “uncontrolled” drifts and rotations of the gold nanoparticle during the thermal treatment, we cannot provide a complete description of this twinned gold nanocrystal through the entire cycles, from RT to 400 °C. However, from the same batch of sample, we successfully measured another twinned crystal (*Particle 3*) under reaction conditions during heating at 200 and 400 °C and after cooling down at room temperature (referred as RT back).

A clear signature of twin domains in the nanoparticle is observed in Figure 6.6 with regions with missing Bragg electron density on the reconstruction of *Particle 3* under reaction conditions at 200 °C. The size of the reconstructed object is 120 nm across at the widest point and the shape (seen from the bottom view) is hexagonal, in great agreement with the previous discussed results. The two parent pieces for this crystal are represented by the numbers 1 and 2 in the first 3D reconstruction shown in Figure 6.6. It deals with a twinned nanocrystal with incoherent boundaries with high boundary energy and a partial dislocation on each slip plane (1).

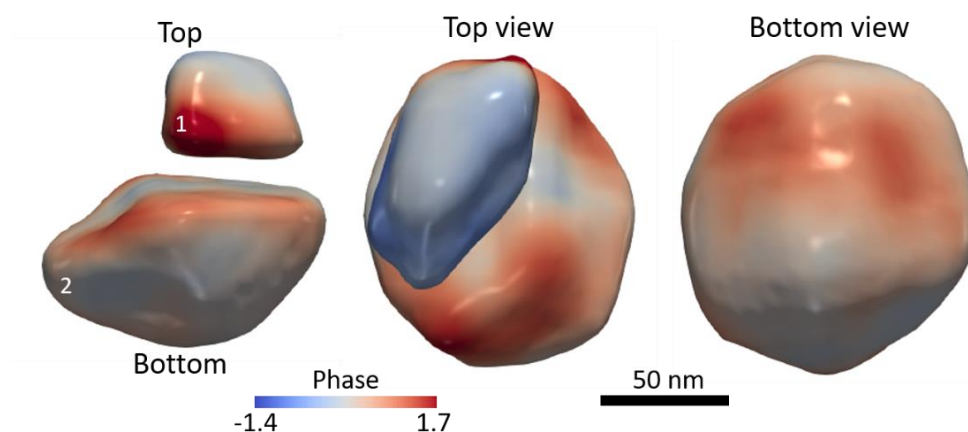


Figure 6.6. Different views of the 3D reconstruction of *Particle 3*, shown as function of phase for the measurement done at 200 °C under CO/O₂. The scale bar is 50 nm.

Figure 6.7 displays different 3D views for the reconstructions from the sample at 200 and 400 °C whilst the catalytic activity is increasing. We also show the reconstruction at RT back under CO/O₂ atmosphere where no more catalytic conversion can be measured. Corresponding cross-sections are shown in Figure A3 (Appendix). It is noticeable that for the temperatures of 200 and 400 °C the corners of the NP are well faceted, as the reaction occurs. Then, when back to RT, where no CO conversion is observed, the corners become more rounded. The presence of the corners with the low-coordinated atoms is directly linked to the catalytic properties.

Besides, the phase offset between the parent regions at 200 and 400 °C is approximately 0.8 rad. The size of the twin domain slight increase from 18 to 21 nm during the heating from 200 to 400 °C under reaction conditions. The distribution of phases is random over the parent regions, and we don't observe formation of partial dislocation or nanotwin propagation as seen for the initial twin free nanoparticle (*Particle 1*) presented in the previous chapter. The partial dislocation is already present on the slip plane of the incoherent twin boundaries imperfection. In this case the adsorbate-induced surface stress seems to induce a slight motion of the twin domain instead of the previously described nucleation of nanotwin.

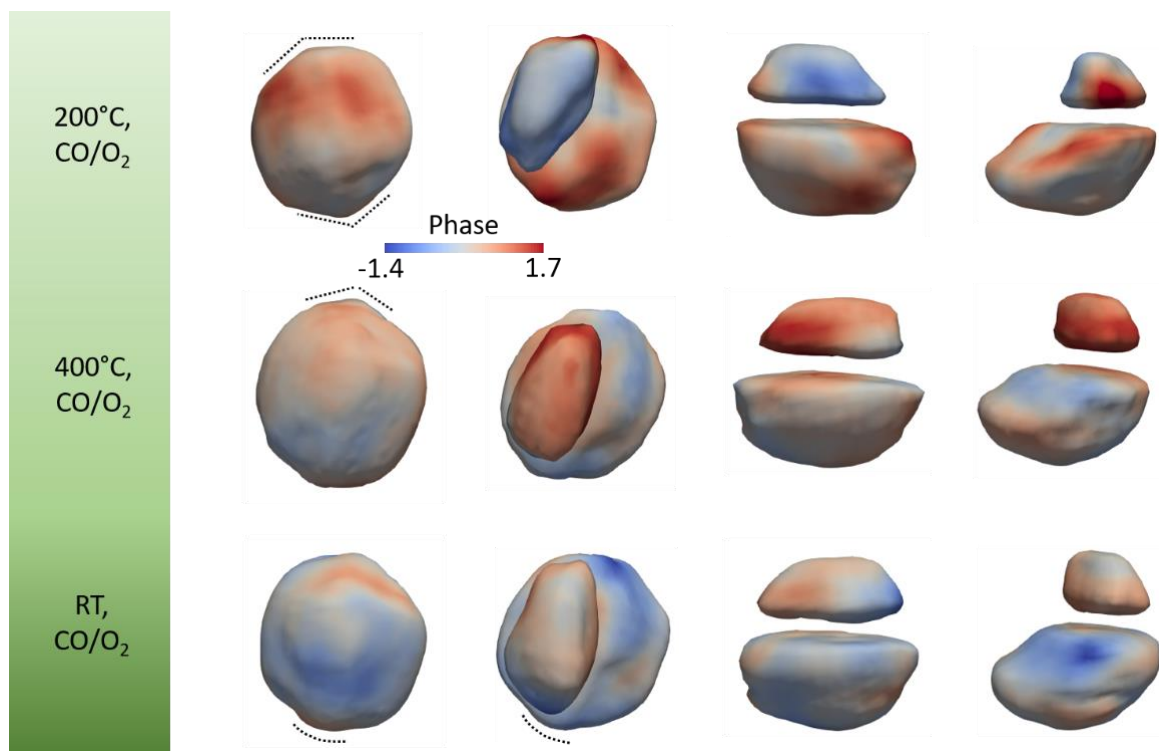


Figure 6.7. Different views of the 3D reconstructions for *Particle 3* at the three different temperatures measured. The data are shown as function of phase.

CONCLUSIONS

These results demonstrate that Bragg CDI is a highly powerful technique to uncover defects found in crystalline structures, such as twin domains, under realistic working conditions. Although the influence of twin domains in gold nanocrystals in the CO oxidation reaction is not well established, it is known that it does influence the catalytic properties, as pointed out by few works (6). The interface between the parent and twinned portions can change the surface energy on the nanoparticle and consequently alter the reaction pathway.

In the case of the nanoparticles presented in this chapter, under the reactive gas atmosphere, the adsorbate-induced surface stress caused by the reactants gas molecules seems to provoke a slight motion of the twin domain. Given the nanoparticle studied in the previous chapter and the ones presented in the current chapter, the structural differences between them reveals inhomogeneities in the crystalline lattice, which can induce different catalytic properties for them. This work demonstrates the importance of studying heterogeneities present in the composition of nanomaterials.

REFERENCES

1. LUO, X.-M.; LI, X.; ZHANG, G.-P. Forming incoherent twin boundaries: a new way for nanograin growth under cyclic loading. **Materials Research Letters**, v. 5, n. 2, p. 95–101, 2017.
2. CHOWDHURY, P. et al. Mechanical response of low stacking fault energy Co–Ni alloys – Continuum, mesoscopic and atomic level treatments. **International Journal of Plasticity**, v. 71, p. 32–61, 2015.
3. YAU, A. et al. Imaging the Hydrogen Absorption Dynamics of Individual Grains in Polycrystalline Palladium Thin Films in 3D. **ACS Nano**, v. 11, n. 11, p. 10945–10954, 2017.
4. ULVESTAD, A. et al. 3D Imaging of Twin Domain Defects in Gold Nanoparticles. **Nano Letters**, v. 15, n. 6, p. 4066–4070, 2015.
5. YAU, A. et al. Bragg coherent diffractive imaging of single-grain defect dynamics in polycrystalline films. **Science**, v. 356, n. 6339, p. 739–742, 2017.
6. KRAJČÍ, M.; KAMEOKA, S.; TSAI, A.-P. Twinning in fcc lattice creates low-coordinated catalytically active sites in porous gold. **The Journal of Chemical Physics**, v. 145, n. 8, p. 084703, 2016.

CHAPTER VII: Gold Nanorods Stability **Studied by Nanodiffraction**

7.1. INTRODUCTION

Comprehensive knowledge of the structural/morphology stability of thin gold nanorods is crucial for their reliable use in a wide range of applications such as functional nanoelectronics and mechatronics devices, medicine and theragnostic. In this Chapter, by using microscopy techniques, X-ray nanodiffraction/fluorescence and scanning electron microscopy, we discovered that the Rayleigh instability phenomenon exists in ultrathin nanorods at room temperature.

It is well-known that gold nanoparticles present the ability to absorb and confine light because of the presence of the SPR band. Gold nanorods (Au NR) exhibit two SPR bands, the transverse and longitudinal modes. As the band position in both modes is sensitive to the size and shape of the nanorods, one can tune the position of the band by controlling the aspect ratio (length/diameter) value. This property is crucial for photocatalysis applications (1–4).

Another promising application related to this phenomenon is in the field of nonlinear optical response. The lack of suitable optical modulators in the visible region restrict severely the progress of visible pulsed lasers. Au NR with low aspect ratio value usually have the transversal and longitudinal SPR bands in the visible region, which makes them promising candidates for optical response in visible lasers (5). Still in the optical response area, study of the decay channels derived from the SPR absorption in Au NR in ultrafast time scale is nowadays a matter of fundamental importance because it is related to their mechanical and electronical properties (6). One of the major consequences of decay relaxation is the increase in the thermal energy which causes deformation on the nanoparticle surface (7). In this case, nanoparticle stability under an external perturbation (such as thermal energy) can be crucial and it is a key issue for the understanding of the decay process. Another relevant area for Au NR is in the biological field. Since the process of surface functionalisation of gold nanorods is relatively simple, several biomolecules can be attached to the rod surface and subsequently conjugated to a biological agent, making them relevant to a variety of applications including drug delivery (8), biological sensing (9,10), and photothermal therapy (11).

But nanorods structures are prone to instabilities. This is known as Rayleigh instability, a phenomenon discovered by Plateau and theoretically pioneered by

Rayleigh in the 1870s (12); it corresponds to the decay of a liquid cylinder or wire into a row of spherical droplets for achieving surface energy minimisation. Nichols and Mullins systematically extended the Rayleigh's theory to solids (13). The rearrangement of the surface morphology would lead to significant variations in the electronic structure and electrical transport properties.

According to Nichols and Mullins, free-standing nanorods will break up into nanospheres with larger diameter. Nanorods will fragment into nanospheres with a radius $R_{NS} = 3.78R_{NR}$, where R_{NR} denotes the radius of the nanorod and R_{NS} of the nanosphere. They also demonstrated that the rod shape is not stable against a perturbation whose wavelength is larger than the rod circumference. In this case, the fragmentation will occur for the minimum wavelength of perturbation $\lambda_{critical} = 2\pi r_{NR}$. From the thermodynamic point of view, the origin of the phenomena is that if the λ of the undulation obeys the criteria $\lambda > 2\pi R_{NR}$, then, mathematically, the surface area will be reduced, consequently achieving surface energy minimization.

Another noteworthy conclusion is that the maximum growth rate occurs at a maximum wavelength λ_{max} and therefore is expected to control the distance between the final spheres formed under the influence of the perturbation. In this extrapolation for solids rods it was found that the phenomenon happens through mass transport mechanisms, where $\lambda_{max} = 8.89, 9.02$ and $12.96R_{NR}$ for surface diffusion, internal volume and external volume diffusion, respectively. In the fragmentation process, the rod volume is conserved, and as the surface atoms are more unstable and easier to be moved, the phenomenon is usually governed by surface atoms diffusion.

7.2. X-RAY NANODIFFRACTION EXPERIMENTS OF Au NR

7.2.1. 26-ID-C beamline at APS

Scanning nanodiffraction and fluorescence measurements were performed at the 26-ID-C nanoprobe beamline (14) of the Advanced Photon Source (APS) at the Argonne National Laboratory (Argonne, USA). A schematic of the setup is presented in Figure 7.1.

The beam was focused using a coherently illuminated Fresnel zone plate (FZP) with a diameter of 100 μm and an outer-most zone width of 30 nm, corresponding to a

focal length of 9 mm at 9 keV. The nanocrystals were placed into the X-ray beam focus ($30 \times 30 \text{ nm}^2$) and raster scanned by translating the FZP with 10 nm steps on a $300 \times 300 \text{ nm}^2$ sample area. At each scanning position, diffraction patterns of 10 s exposure time were recorded with a piXirad detector with $60 \times 60 \mu\text{m}^2$ pixel size placed 500 mm downstream from the sample. For each scan the fluorescence (Au L1-edge) radiation of the same region was recorded as well. The detector was positioned on the (200) 2θ Bragg angle to record the coherent diffraction pattern (theoretical $2\theta = 39,5^\circ$). The total duration of a 31×31 scan was about 3 hours. No X-ray radiation damage was detected during the measurements.

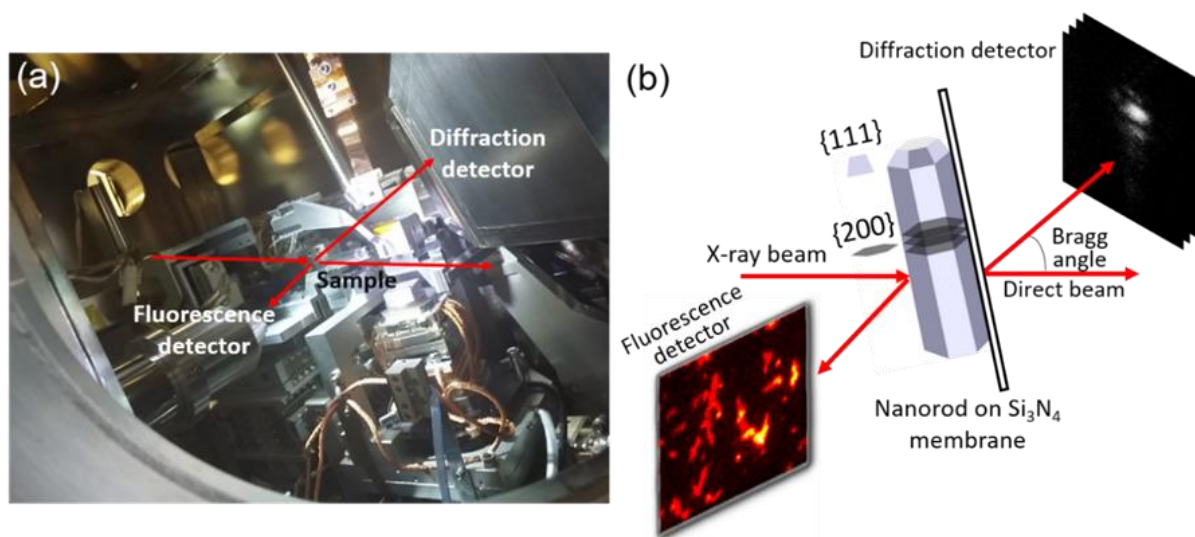


Figure 7.1. (a) Picture of the 26-ID-C beamline setup and (b) schematic representing the as showed picture of the experimental setup for diffraction/fluorescence mapping; a sketch of the NR composed by the {111} and {200} planes is also displayed.

7.2.2. Sample preparation

The synthesis of the gold nanorods is described in Chapter III. Then one drop of the colloidal dispersion containing the Au NR was placed directly onto a 30 nm thick silicon nitride membrane (PELCO support films - TedPella). The sample was dried for 24 hours and characterised by scanning transmission electron microscopy (STEM). Figure 7.2 shows the STEM image of the gold nanorods dispersed on the membrane, that will be used for the X-ray nanodiffraction and fluorescence measurements.

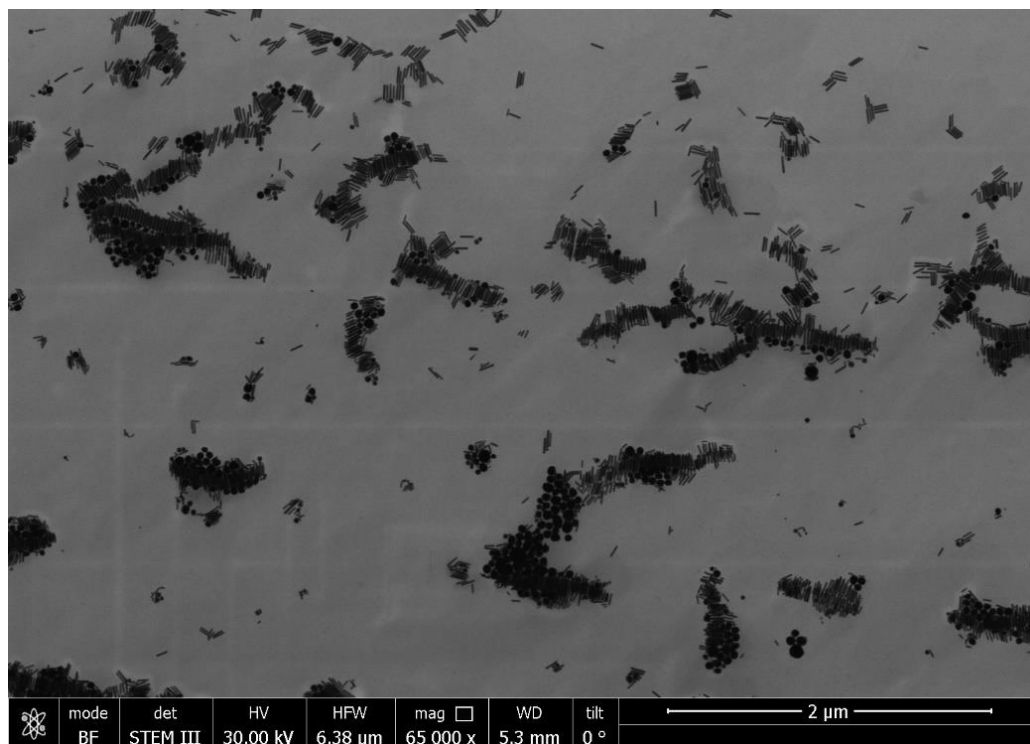


Figure 7.2. Scanning transmission electron microscopy of the gold nanorods dispersed on the silicon nitride membrane used for the nanodiffraction and fluorescence measurements.

7.2.3. Gold nanorod alignment

After a coarse alignment with an on-axis optical microscope, the Si_3N_4 membrane was raster scanned over a large-area ($3 \times 3 \mu\text{m}^2$), recording the Au fluorescence signal (L1-edge). The 2D Au fluorescence map was acquired simultaneously with the total diffraction at (200) 2θ Bragg angle. The 100 nm step size of the latter scan revealed adequate to identify the individual nanocrystals, by fluorescence and the properly oriented nanocrystals by diffraction. Indeed, it is a major challenge with Bragg diffraction measurements to align both the sample and the beam in both real and reciprocal space (15,16). The real-space alignment requires positioning and controllably moving the sample in the nanofocused beam, with a precision that should be significantly smaller than the focus size, here inferior to 30 nm. The reciprocal-space requirement means that the beam and the sample lattice must be aligned at the correct angle to fulfil the Bragg condition.

7.3. GOLD NANORODS

Figure 7.3 presents the STEM (a) and combined X-ray fluorescence and nanodiffraction ((b) and (c), respectively) results of the same region of a membrane with the gold nanorods. The dashed white square represents the same area in (a) and (b) and the whole area of (c). The bright spots in Figure 7.3 (c) corresponds to gold nanorods which sample lattice is aligned at the correct angle to fulfil the (200) Bragg condition. Three nanorods were studied, indicated by the green arrows in (c) and named NR1, NR2 and NR3 in the next sections.

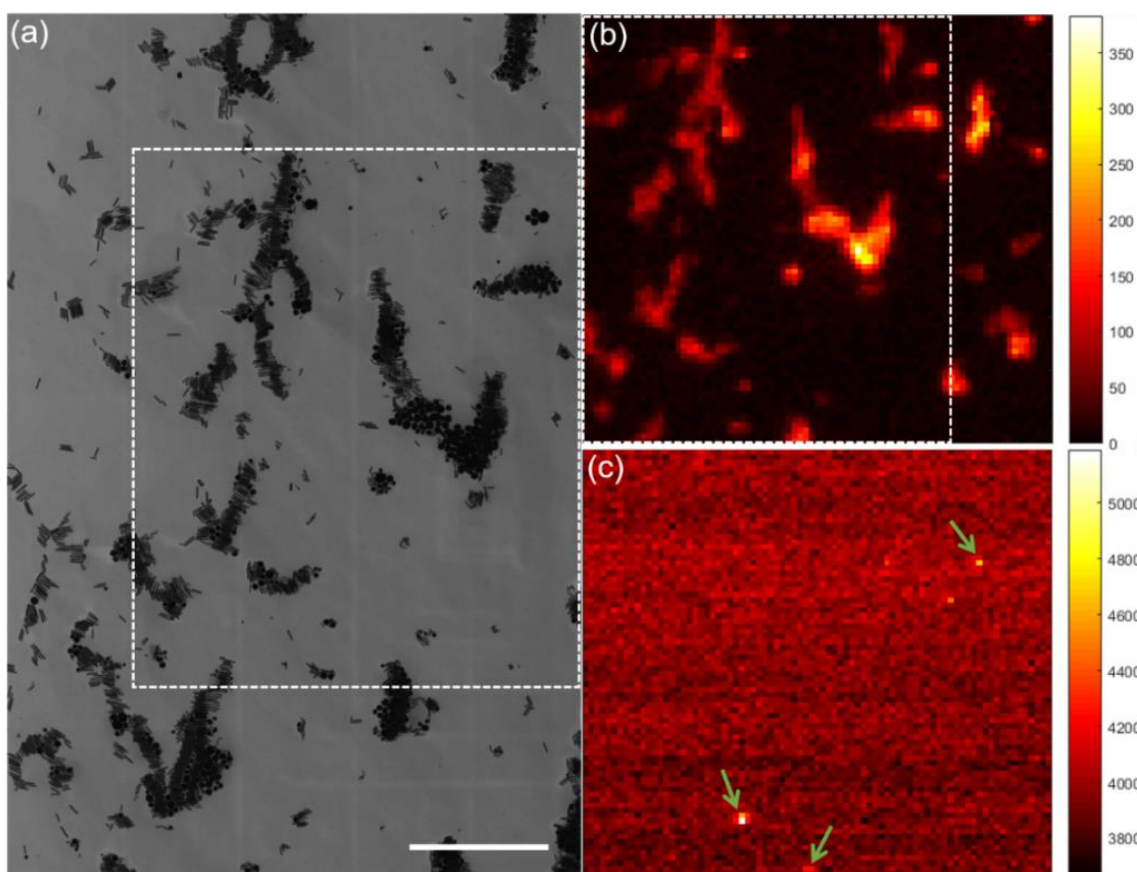


Figure 7.3. (a) STEM image of the explored area during the nanodiffraction experiment (scale bar 1 μm); (b) fluorescence pattern recorded on the area detector of the region highlighted by the white dashed square in (a); (c) diffraction pattern of the same region recorded simultaneously as the fluorescence. The green arrows point to bright diffraction spots derived from well oriented objects. The 2θ angle was configured to the (200) reflection.

Figure 7.4, Figure 7.5 and Figure 7.6 display the STEM, fluorescence and diffraction data collected for NR1, NR2 and NR3, respectively. For all the figures, (a) shows the SEM image taken before the experiment. The scale bar is 500 nm. In (b)

and (c) is displayed the fluorescence mapping and diffraction pattern, respectively, of the same area shown in (a). In (d), (e) and (f), the same data sequence described previously is shown, but the scan was done in the smaller area inside the blue squares in (b) and (c) using finer steps. For NR1, we investigated a region of 320 x 320 nm using 20 nm steps in both, x and y axes, 10 s exposition at each position. In this case, the scan has 16 x 16 points, which results in 256 acquisitions. For NR2, a region of 120 x 220 nm was investigated using 20 nm steps, 10 s of exposure, resulting in a 11 x 6 points scan and 66 acquisitions. For NR3 was the same as NR1 but using 10 nm steps, resulting in 31 x 31 points, *i.e.*, 961 points. It is worth mentioning that this beamline has unprecedented capabilities such as high stability and optics manipulation precision, enabling the use of such small steps for scanning the sample. In (f) the area highlighted by the dashed rectangle represents the same area as in (d), that shows a zoomed in image of the SEM shown in (a). The rows 1, 2 and 3 inside the dashed rectangle are the ones taken for the strain calculation. In Figure 7.4 (f), the white arrows represent the direction of the scan: from the left to the right, from the bottom to the top.

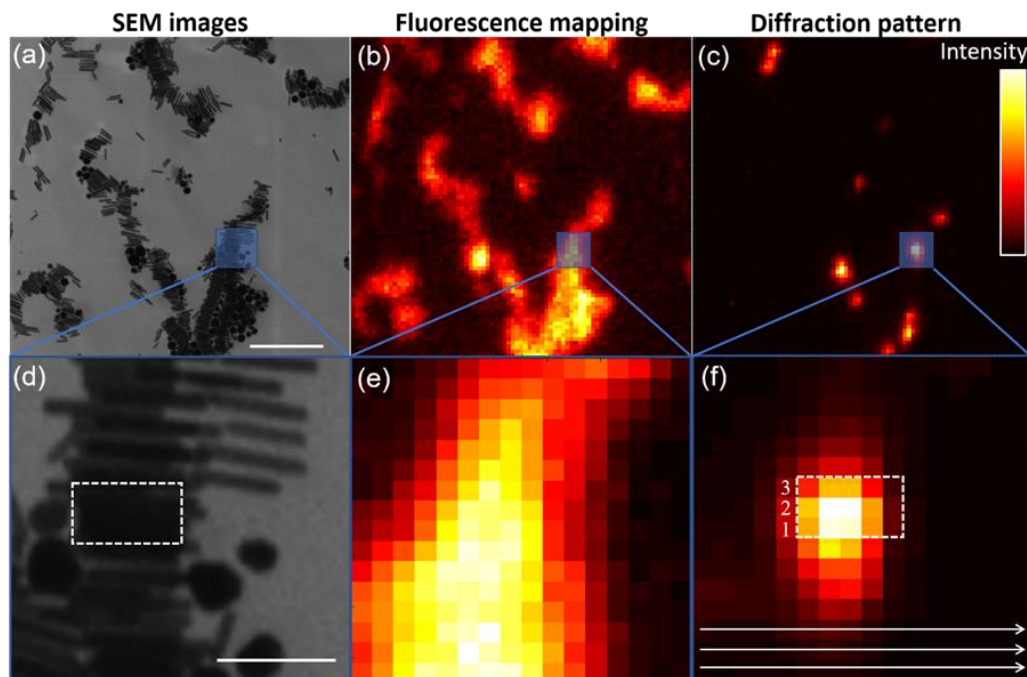


Figure 7.4. (a) STEM image (scale bar 500 nm) of the region mapped in fluorescence mode shown in (b); (c) diffraction pattern of the same region. The area highlighted by the blue square in (a) is shown zoomed in (d) (scale bar 100 nm); (e) and (f) fluorescence mapping and diffraction pattern, respectively, of the same area using finer steps. In (f), the white arrows represent the direction of the scan (from the left to the right, from the bottom to the top) and the rows 1, 2 and 3 inside the dashed rectangle are the ones taken for the strain calculation.

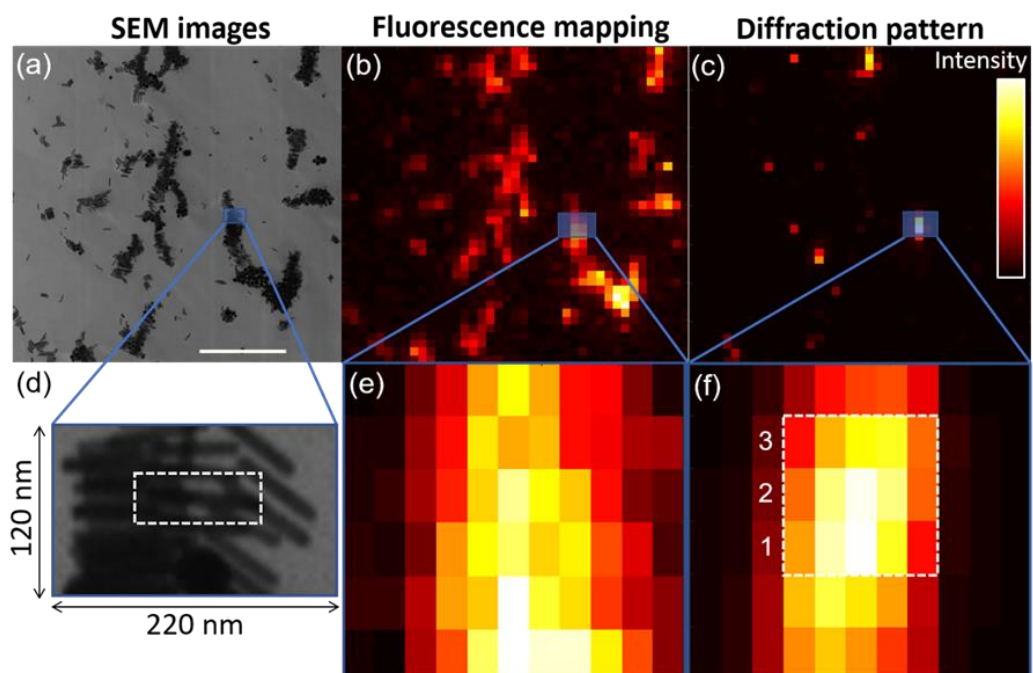


Figure 7.5. (a) SEM image (scale bar 500 nm) of the region mapped in fluorescence mode shown in (b); (c) diffraction pattern of the same region. The area highlighted by the blue square is shown zoomed in (d); (e) and (f) fluorescence mapping and diffraction pattern, respectively, of the same area using finer steps. In (f), the rows 1, 2 and 3 inside the dashed rectangle are the ones taken for the strain calculation.

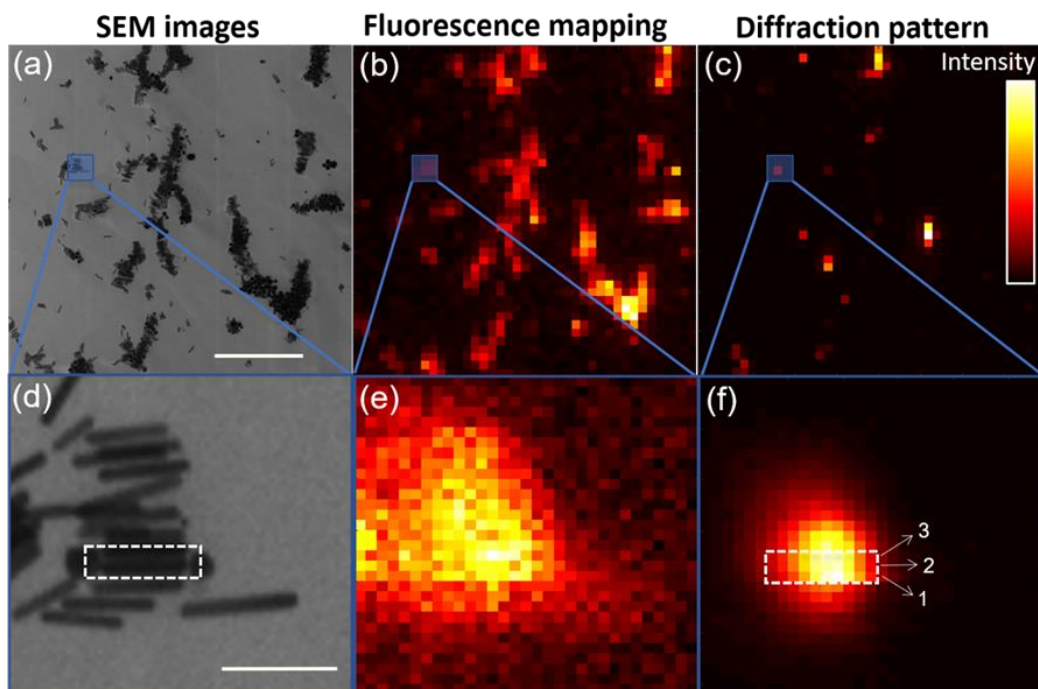


Figure 7.6. (a) SEM image (scale bar 500 nm) of the region mapped in fluorescence mode shown in (b); (c) diffraction pattern of the same region. The area highlighted by the blue square is shown zoomed in (d); (e) and (f) fluorescence mapping and diffraction pattern, respectively, of the same area using finer steps. In (f), the rows 1, 2 and 3 inside the dashed rectangle are the ones taken for the strain calculation.

7.3.1. Strain determination

Regarding the white dashed rectangles in Figure 7.4, Figure 7.5 and Figure 7.6, we averaged the strain values of the columns of rows 1, 2 and 3. Figure 7.7 shows the corresponding diffraction patterns of row 2 inside the red rectangles for the three nanorods studied. The strain was then calculated as just mentioned for each positions of the three gold nanorods.

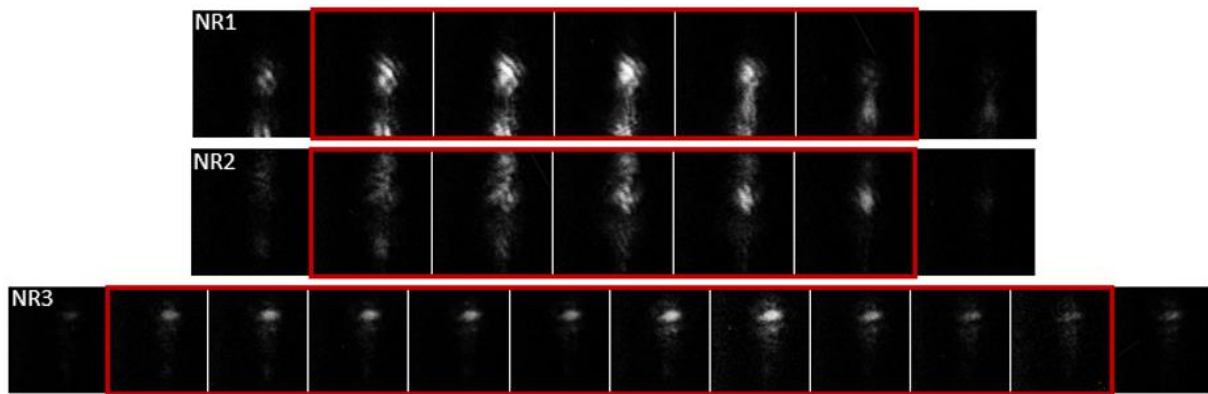


Figure 7.7. Diffraction patterns measured along the NR1, NR2 and NR3. The red squares indicate the patterns used for the strain analysis.

The lattice spacing is determined applying the Bragg law and the strain is defined by using equation (8) (described in Chapter II). As the 2θ position changes as function of the presence of strain in the crystal, having measured the relative Bragg positions we can determine the relative variations of the strain distribution across the sample.

The strain as a function of the position over the nanorod length is presented in Figure 7.8. The final resolution achieved is determined by the X-ray beam size, $30 \times 30 \text{ nm}^2$, although this could be improved by performing a “ptychography” analysis, as the data were collected is overlapping scans.

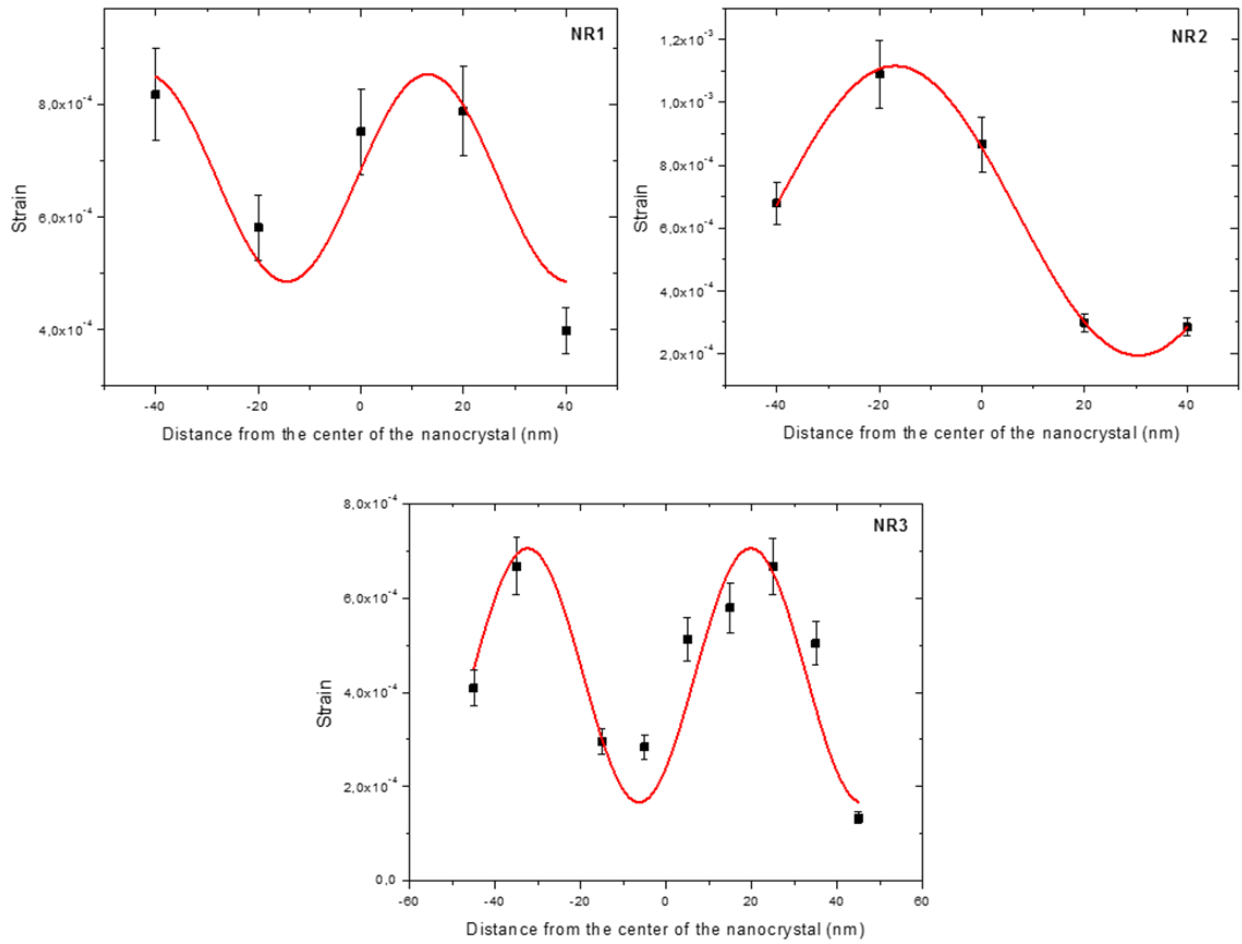


Figure 7.8. Strain as function of the distance from the center of the nanorod, for NR1, NR2 and NR3. Black dots are the strain data and the red curves the sin fitting.

From each fitting we can determine the perturbation wavelength λ : $\lambda_{NR1} = 27,5$ nm, $\lambda_{NR2} = 47,4$ nm and $\lambda_{NR3} = 26,1$ nm. The radius of the nanorods is 6.6 nm. According to Nichols and Mullins, for a minimum wavelength of perturbation of:

$$\lambda_{critical} = 2\pi R_{NR} = 2\pi \cdot 6.6 = 41,5 \text{ nm} \quad (13)$$

the fragmentation of the nanorods should occur. This would apply to NR2 for which $\lambda_{NR2} > \lambda_{critical}$. The stability of NR2 could be explained by the adsorption of the CTAB surfactant molecules on the surface of the nanorods which stabilise it. Nevertheless, we can observe in Figure 7.4 (d) nanospheres of diameter ~ 50 nm. The latter corresponds to the diameter predicted by Nichols and Mullins, where nanorods will

fragment into nanospheres with a radius $R_{NS} = 3.78R_{NR}$, (R_{NR} denotes the radius of the nanorod and R_{NS} of the nanosphere).

On the other hand, for NR1 and NR3, $\lambda_{NR3} < \lambda_{NR1} < \lambda_{critical}$ the fragmentation into nanospheres is not expected. Nonetheless, the strain analysis (Figure 7.8) reveals a sinusoidal behavior of the strain along the nanorod length, corresponding to the Rayleigh instability that is schematised in Figure 7.9.

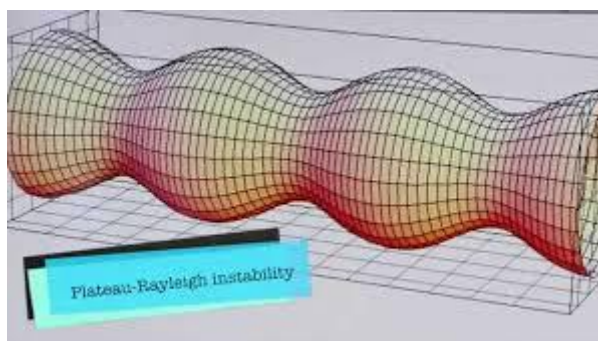


Figure 7.9. Schematic representation of the Rayleigh instability for a solid rod.

CONCLUSIONS

In conclusion, we mapped the strain over the gold nanorod. The strain pattern encoded in the nanorods structure is in agreement with the so-called Rayleigh instability and this work demonstrates that the phenomenon exists even at RT. Further analysis of the ptychography data will enable to improve the spatial resolution below 30 nm and determine the strain with higher accuracy.

As the properties of such gold nanorods make them suitable for a wide range of applications, the existence of these instabilities emphasises that the stability of Au NR must be considered before employing them in nanoscale devices.

REFERENCES

1. LIN, J. et al. Sonogashira cross-coupling on the Au(111) and Au(100) facets of gold nanorod catalysts: Experimental and computational investigation. **Journal of Catalysis**, v. 330, p. 354–361, 2015.
2. ZHAO, J. et al. Direct coating of mesoporous titania on CTAB-capped gold nanorods. **Nanoscale**, v. 8, n. 10, p. 5417–5421, 2016.

3. ZHOU, N. et al. TiO₂ coated Au/Ag nanorods with enhanced photocatalytic activity under visible light irradiation. **Nanoscale**, v. 5, n. 10, p. 4236–4241, 2013.
4. FANG, C. et al. (Gold core)/(titania shell) nanostructures for plasmon-enhanced photon harvesting and generation of reactive oxygen species. **Energy and Environmental Science**, v. 7, n. 10, p. 3431–3438, 2014.
5. WANG, S. et al. Nonlinear optical response of Au nanorods for broadband pulse modulation in bulk visible lasers. **Applied Physics Letters**, v. 107, n. 16, p. 161103, 2015.
6. SOAVI, G. et al. Ultrasensitive Characterization of Mechanical Oscillations and Plasmon Energy Shift in Gold Nanorods. **ACS Nano**, v. 10, n. 2, p. 2251–2258, 2016.
7. ZIJLSTRA, P. et al. Acoustic Oscillations and Elastic Moduli of Single Gold Nanorods. **Nano Letters**, v. 8, n. 10, p. 3493–3497, 2008.
8. WANG, S. et al. Biologically Inspired Polydopamine Capped Gold Nanorods for Drug Delivery and Light-Mediated Cancer Therapy. **ACS Applied Materials & Interfaces**, v. 8, n. 37, p. 24368–24384, 2016.
9. MA, W. et al. Attomolar DNA detection with chiral nanorod assemblies. **Nature Communications**, v. 4, n. 1, 2013.
10. WANG, Y.; TANG, L. Multiplexed gold nanorod array biochip for multi-sample analysis. **Biosensors and Bioelectronics**, v. 67, p. 18–24, 2015.
11. WANG, J. et al. Assembly of Aptamer Switch Probes and Photosensitizer on Gold Nanorods for Targeted Photothermal and Photodynamic Cancer Therapy. **ACS Nano**, v. 6, n. 6, p. 5070–5077, 2012.
12. L. RAYLEIGH. On the instability of jets. **Proc. London Math. Soc.**, v. 10, p. 4–13, 1878.
13. KARIM, S. et al. Morphological evolution of Au nanowires controlled by Rayleigh instability. **Nanotechnology**, v. 17, n. 24, p. 5954–5959, 2006.
14. WINARSKI, R. P. et al. A hard X-ray nanoprobe beamline for nanoscale microscopy. **Journal of Synchrotron Radiation**, v. 19, n. 6, p. 1056–1060, 2012.
15. WALLENTIN, J. et al. Simultaneous high-resolution scanning Bragg contrast and ptychographic imaging of a single solar cell nanowire. **Journal of Applied Crystallography**, v. 48, n. 6, p. 1818–1826, 2015.
16. ROBINSON, I.; HARDER, R. Coherent X-ray diffraction imaging of strain at the nanoscale. **Nature materials**, v. 8, n. 4, p. 291–298, 2009.

CONCLUSIONS AND FUTURE WORK

Regarding the main part of this thesis, the characterisation of single gold nanoparticles under working conditions was done using Bragg CDI. We succeeded in following the changes in the internal and surface structure of the nanocrystals during the reaction occurrence by mapping the phase/strain of the reconstructed nanoparticles in the different measured conditions.

We developed an *in situ* cell (Chapter IV) to perform Bragg CDI under controlled gas/temperature environments, which is crucial for *in situ/operando* measurements.

The changes in the surface morphology of the gold nanocrystal discussed in Chapter V indicates that even at RT the adsorption gases strongly interact with the surface atoms. This interaction is evidenced by the compressive to tensile strain swap from air to CO/O₂ atmospheres at RT. The adsorption leads to a compressive surface stress, resulting in the smoothing curves seen for the reconstructed nanoparticles. During the reaction, there is the reconstitution of the sharper edges of the nanoparticles, which are regions of low-coordinated atoms and represent the catalytic sites for the reaction. As the temperature increases and the NP becomes active, there is the formation of ribbons seen as phase oscillation inside the particle and it was attributed to the formation of a nanotwin network, which was correlated with the increased catalytic activity of the gold nanocrystal.

The capability of Bragg CDI to observe changes in morphology/crystalline lattice under dynamic conditions is very powerful and fills up the gap for 3D characterisation under *in situ/operando* conditions to get atomic scale information.

The reconstructions shown in Chapter VI is a twinned Au NP, a very common type of defect in crystalline structures. As the presence of twin domains does influence the crystal properties, the investigation of twin domains is of paramount importance. The slight changes in the twin domain size between the parent crystal regions can influence the catalytic properties as the number of active sites may change in this case. As future work for this part of the thesis, the calculation of the stress, as was done for the particle in the previous chapter, would help to get insights about the link between the structure and the catalytic properties of this particle.

Another important additional work to do would be to study the crystalline structure of the seed particles to verify if they are single crystals or twinned particles.

Twinned nanoparticles can grow from either twinned or single-crystalline seeds. If single-crystalline, a nanoparticle seed can generate twin defects during the growth of the larger particle (or through a coalescence mechanism). Alternatively, if the nanoparticle seed has a twinned structure, it can grow layer-by-layer in the twinned sequence. Understanding the nanoparticle structure formation is important for controlling the reaction conditions so we can selectively enhance or suppress the single-crystalline/twinned nanoparticle growth, depending on the material's desired properties. We have evidences that the seed precursor is formed by twinned nanoparticles, but a deeper investigation is needed to draw a conclusion. If we consider that the seeds are in fact twinned, most probably the defected structure of the seed is somehow transferred to the entire larger particle, as already reported in few works. This could happen through epitaxial growth. In the case that the seed dispersion is composed by single crystals, it would be interesting to investigate when exactly the twin domains are formed in the crystalline structure: does it form during the wet synthesis procedure or during the calcination process? As it does affect the catalytic properties, this investigation is interesting for the future.

An important study regarding this topic would be to control the degree of twin domains in gold nanoparticles, having twin free crystals in one case and twinned nanoparticles in another case and investigate the structural differences between both and try to correlate this with the catalytic properties of the nanoparticles. Then, we can answer the question: is there any difference between the catalytic performance of defect free and twinned Au NP?

Although the resolution of the CDI techniques does not yet reach the atomic scale as in electron microscopy, this will be dramatically improved with the operation of 4th generation synchrotron sources like SIRIUS (under construction in Campinas, Brazil, where the Cateretê beamline will be dedicated to perform CDI and is planned to operate in 2019). When Cateretê beamline will be in operation, coherent X-ray diffraction imaging techniques will achieve the spatial and time resolution required to study real devices and the techniques could be applied during *in situ/operando* measurements: thermal treatment; use of dedicated cell under different atmospheres; study of charge/discharge in batteries systems; among many other possibilities. This will undoubtedly expand new horizons for the scientific community once in SIRIUS the coherent flux of photons will be 2 to 3 orders of magnitude higher than the available

ones, which means that time resolution in the second range will be possible with an improved spatial resolution.

APPENDIX

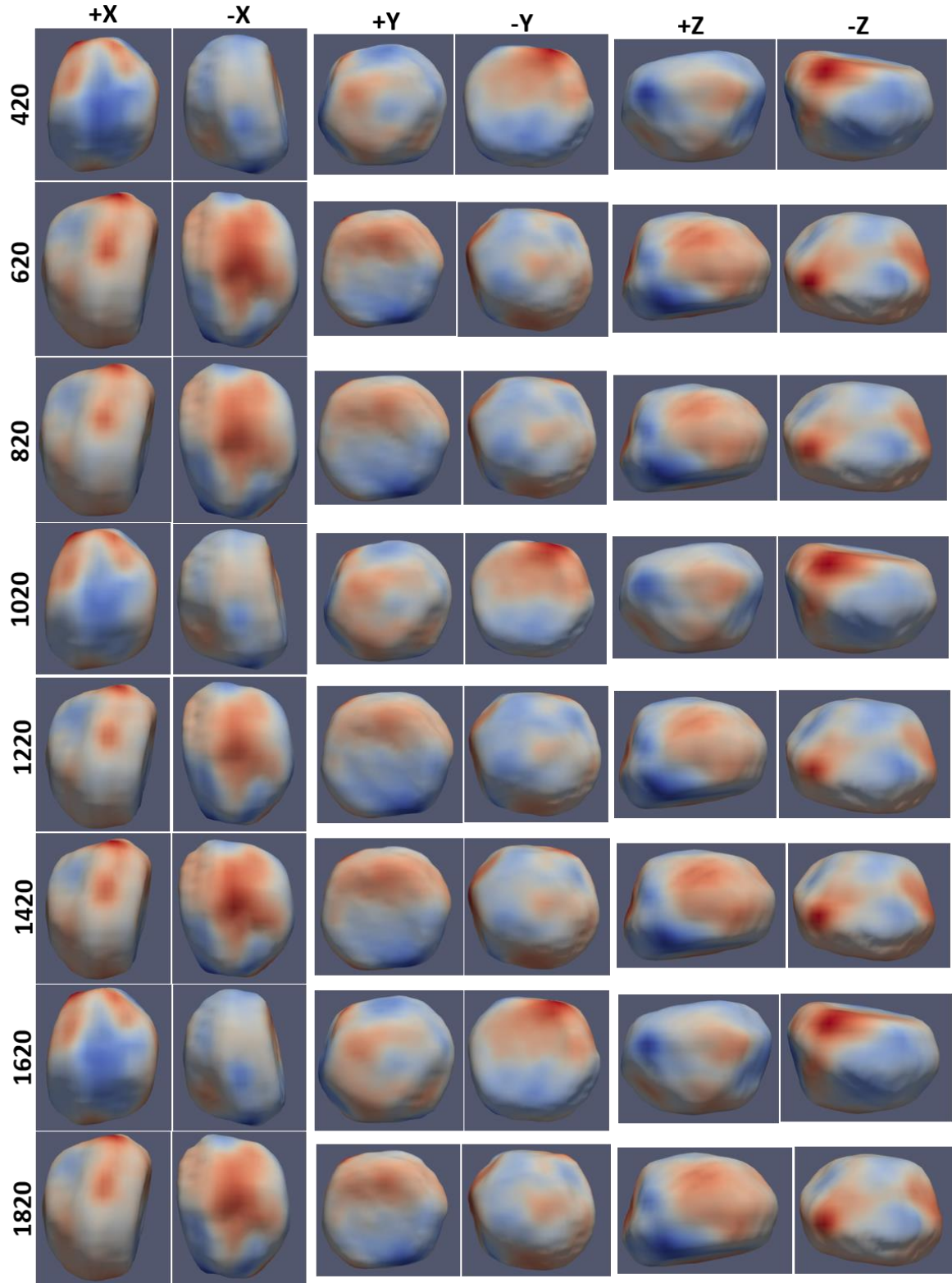


Figure A.1. Reconstructions of the NP measured at RT under air atmosphere, using different number of iterations (shown vertically on the left). The reconstructions are shown along different direction axes (shown in the first line on the top).

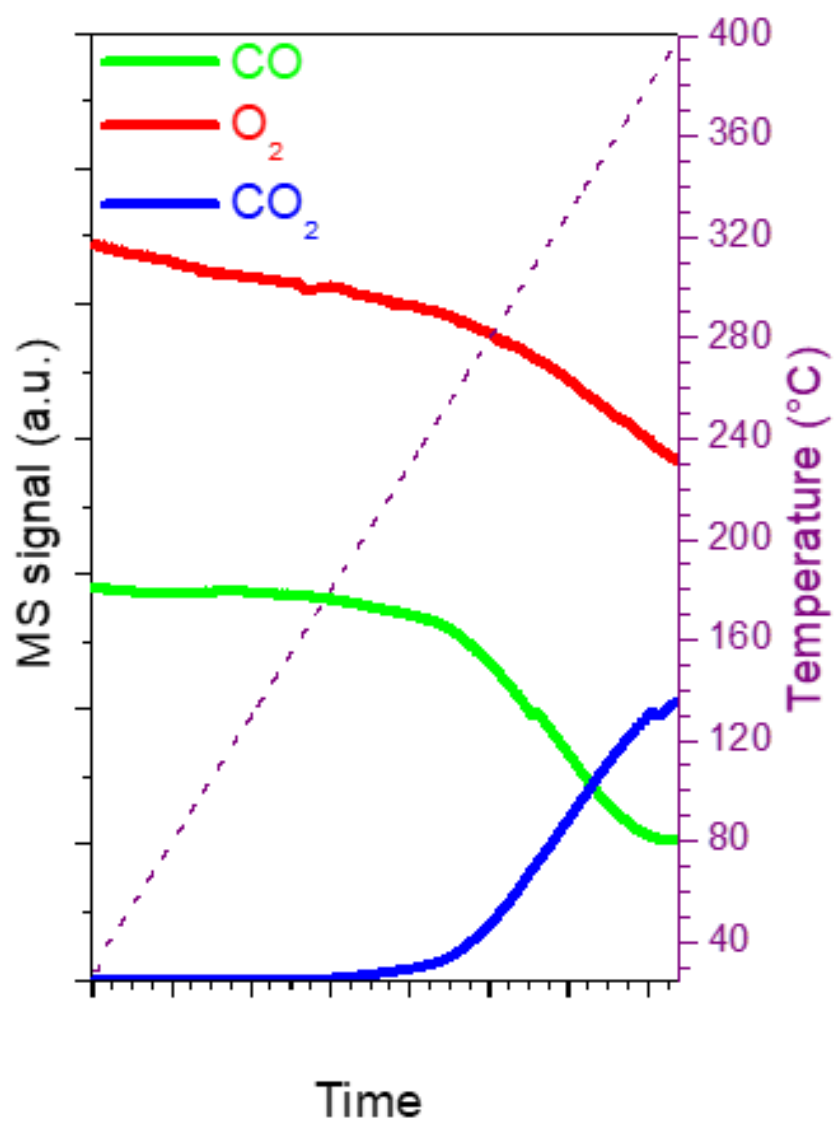


Figure A.2. Mass spectrometry signal of O₂, CO and CO₂ during heating inside our *in situ* CDI cell of the gold catalyst under CO/O₂ gas mixture (CO:O₂, 0.5%:3.7%).

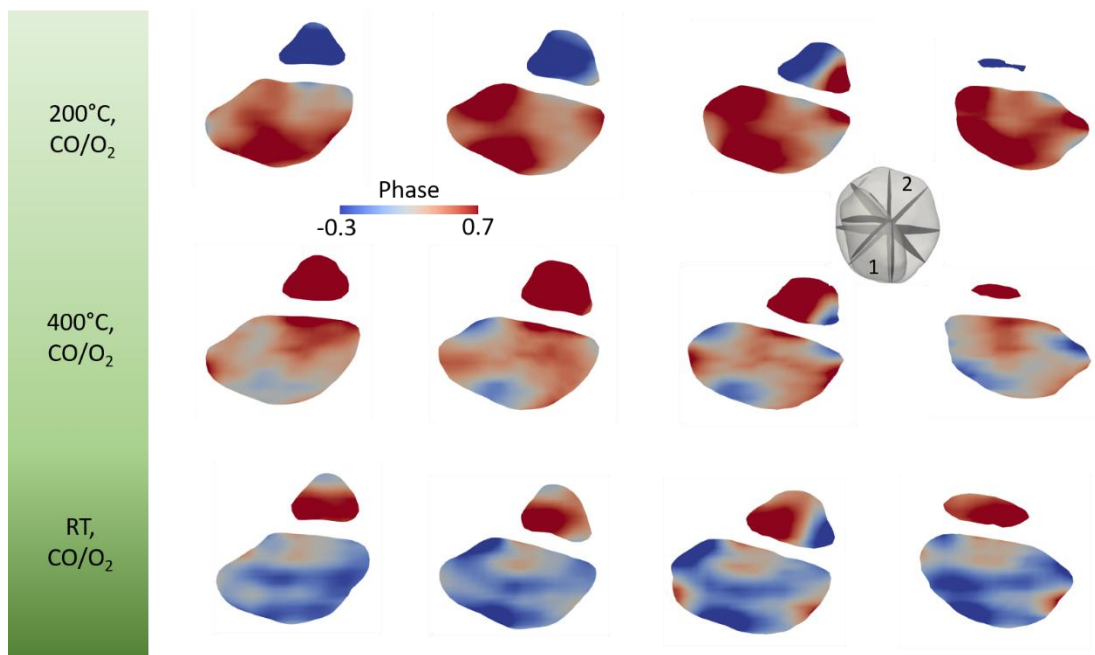


Figure A.3. Cross-section views taken as shown in the inset (1 and 2 are the parent crystal pieces) at the different temperatures for *Particle 3*. The data is shown in function of phase.

ANNEX

Characterisation techniques

A. Electron microscopy

The electron microscopy measurement was performed at the Brazilian Nanotechnology National Laboratory (LNNANO, Campinas-SP). The seed Au NP, *50_Au*, *120_Au*, the Au NR and the sample *NPILCIAuCl-a* were imaged using a High-Resolution E-SEM FEI Quanta 650 FEG, operating in an accelerating voltage of 30 kV using different detectors for scanning and scanning/transmission modes. The samples *NPILBrAuBr*, *NPILBrAuCl*, *NPILCIAuBr*, and *NPILCIAuCl* were characterised by a JEOL JEM 3010 microscope operating at 300 kV (1.7 Å resolution). The samples of Au NP were prepared dropping 6 µL of the colloidal dispersion on Ultrathin Carbon Film copper grids. Those samples made of TiO₂ were analyzed by dispersing a small amount of the solid in water and 3 µL of this suspension were supported in the same type of grid. The samples were dried at room temperature for 24 hours prior to analysis.

B. UV-Vis

The UV-Vis spectroscopy was performed in an Agilent 8453 equipment in a spectral range of 200-1000 nm to verify the surface plasmon resonance band position using a quartz cuvette of 1 cm of optical path length.

The plasmon band is defined as a physical phenomenon caused by collective oscillation of the conductive band of the metal. This phenomenon is due to the fact that the electrons are disturbed by the interaction with the electromagnetic radiation of the incident light. The electric field of the incident radiation leads to the formation of a dipole in the nanoparticles, with the negative charges of the surrounding electrons away from the positive charges that form the metal. To compensate the formation of this dipole, a characteristic wavelength resonance frequency appears, which can be seen in the UV-Vis spectrum (1,2). For gold, the absorption wavelength of the plasmon band is in the visible region for spherical particles and it can be extended to near infrared for anisotropic shapes.

The position of the band of the plasmon resonance gives us an estimate of the size of the nanoparticles. Haiss and collaborators (1) have made an empirical-

mathematical treatment and as result, two formulas were proposed for calculating the diameter of Au NP. When they are in the range of 35 to 100 nm, the calculation is done using the following formula:

$$d = \frac{\ln\left(\frac{\lambda_{spr} - \lambda_0}{L_1}\right)}{L_2} \quad (14)$$

The mean value of the absolute error in the calculation for the particle diameter is only 3%. The theoretical values of the formula are: $\lambda_0 = 512$; $L_1 = 6.53$; $L_2 = 0.0216$ and λ_{spr} is the wavelength position of the SPR band.

For nanoparticles in the range 3-35 nm, we can use the formula:

$$d = e^{\left(B_1 \frac{A_{spr}}{A_{450}} - B_2\right)} \quad (15)$$

Experimentally determined parameters ($B_1 = 3.00$; $B_2 = 2.20$) leads to an error of 11%, which represents a reasonable estimate for the size of the nanoparticles. A_{spr} and A_{450} are the absorption values of the wavelengths of the SPR band and at 450 nm, respectively.

For AuNP smaller than 3 nm, there is no experimental formula derived for the calculation of the particle diameter, but the position of the plasmonic band of absorption in the region of the UV-Vis, in this case, will appear in smaller wavelengths (around 500- 515 nm). In this case, microscopy techniques and X-ray scattering at low angles are essential for the nanoparticle's characterisation.

C. SAXS

This technique was used to characterise the synthesised gold nanoparticles at the SAXS1 beamline of the Brazilian Synchrotron Light Laboratory (LNLS, Campinas-SP). The X-ray beam used was monochromatic at 8 kV ($\lambda = 1.54 \text{ \AA}$). A Pilatus detector was positioned at the two different distances from the samples, 1 m and 3 m, resulting in a q range of 0.01 to 0.4 \AA^{-1} and 0.004 to 0.14 \AA^{-1} , respectively.

D. XRD

The XRD patterns were measured at XPD beamline at LNLS. The X-ray beam used was monochromatic at 8 kV ($\lambda = 1.54 \text{ \AA}$). The diffractograms were recorded using a Mythen 1K detector and the 2θ range was from 10 to 70°.

REFERENCES

1 HAISS, W. et al. Determination of Size and Concentration of Gold Nanoparticles from UV–Vis Spectra. **Analytical Chemistry**, v. 79, n. 11, p. 4215–4221, jun. 2007.

2 KELLY, K. L. et al. The Optical Properties of Metal Nanoparticles: The Influence of Size, Shape, and Dielectric Environment. **The Journal of Physical Chemistry B.**, v. 107, n. 3, p. 668–677, 2003.